The Circumstellar Environments of FU Orionis Stars

Thesis by

Stuart McMuldroch

In Partial Fulfillment of the Requirements

for the Degree of

Doctor of Philosophy

California Institute of Technology

Pasadena, California

1995

(Defended October 28th, 1994)

To my father

Acknowledgments

Although the cover page of this work says "thesis by Stuart McMuldroch" I cannot over-emphasize the debt I owe to so many others. My graduate experience at Caltech has stretched my intellectual and psychological limits - without a large group of friends and colleagues I would never have made it through. I would above all like to thank my father, for without his belief in education and eternal support I would never even have made it to Caltech. He has been and continues to be a strong positive influence in my life that 6,500 miles cannot diminish.

During my stay at Caltech, my thesis advisors Anneila Sargent and Geoff Blake have provided invaluable advice and guidance. Although the road was rocky and I was not the easiest of students, they continued to have faith in me while mine was lacking. I deeply appreciate their time, effort and patience.

The highlights of my graduate tenure are, without doubt, observing at the Owens Valley millimeter-wave array and the Caltech Submillimeter Observatory. I would like to thank Nick Scoville and Tom Phillips in their roles as directors of such fine instruments. I extend a warm thank you to the staff of both the array and the CSO for their prodigious efforts. If possible, they made observing even more enjoyable.

Several people have provided me with assistance while I have been a graduate student. Jim Westphal has been a source of inspiration as a distinguished scientist and human being. Bruce Murray has given me insight into intellectual challenges outside of astronomy. Others, including Ewine van Dishoeck, Todd Groesbeck, Todd Hunter, David Koerner, and Bob Goodrich, have provided me with computer codes and access to data. I also thank the many graduate students who helped write the $\TeX$ macros used in this thesis.

Many friends have kept me relatively sane over my graduate years and I extend

thanks to them all. I would especially like to thank David Koerner for his valuable insight, eclectic conversations, and boundless enthusiasm. Min Su Yun has proven to be a good friend and provider of interesting lunch conversations. Thanks to my roommates Phil and Brad for providing a good place to live. I apologize to my office mates for my tendency to sing wearing headphones. My friends outside of Caltech have provided a much needed opportunity for escape. A special thanks goes to Gage Hutchins, Leslie Leach, Ben Skrainka, Joel Schwartz, and Leon Young.

Finally I humbly thank whatever force brought me into this world and created the marvelous universe I have had the opportunity to study. In my research I have been constantly reminded of a quote from Hamlet that seems pertinent to astronomy: "There is more in heaven and earth, Horatio, than is encompassed by your philosophy."

Abstract

Extensive observations were made of six FU Orionis objects (RNO 1B/1C, V1057 Cygni, Elias 1-12, V1515 Cygni and FU Orionis) and one pre-outburst candidate (V1331 Cygni) using the Owens Valley millimeter-wave array and the Caltech Submillimeter Observatory (CSO). Aperture synthesis maps of CO (1→0), ^{13}CO (1→0), ^{13}CO (2→1), C^{18}O (1→0), and CS (2→1) molecular lines and associated dust continuum emission trace the masses, kinematics and morphology of FU Orionis disks, envelopes, and outflows. Maps from the CSO delineate outflowing gas at larger spatial scales while line strengths, when input into radiative transfer models, yield column densities and fractional chemical abundances.

Unresolved 1.3 mm continuum emission from V1331 Cygni and V1057 Cygni reveal massive circumstellar disks of 0.5 and 0.09 $M_{\odot}$, respectively. Maps of the 2.6 and 3.1 mm continuum emission reveal that RNO 1C is surrounded by a flattened dusty envelope, 5000 AU in size, with mass $\geq$1.1 $M_{\odot}$. No evidence is seen for multiple systems with orbital periods $\gtrsim 4 \times 10^4$ years.

All sources, with the exception of RNO 1B/1C are surrounded by large molecular gas envelopes between 2000-7500 AU in size, with masses ranging from 2×10^{-3} to 0.36 $M_{\odot}$. Aperture synthesis maps suggest the envelopes are asymmetrically distributed. Gas kinematics around V1057 Cygni and Elias 1-12 suggest, but do not demand, that this material is rotating and possibly infalling.

Of the seven sources observed, all but FU Orionis show signs of outflowing molecular gas. No high velocity clumps or "bullets" are seen towards any of the sources. V1331 Cygni, V1057 Cygni, and V1515 Cygni possess arc or ring-like outflow morphologies, while emission from RNO 1B/1C and Elias 1-12 delineates filled outflow shells. All emission patterns are consistent with outflow shells being viewed at different angles. Although based on the statistics of small numbers, observations suggest shells

are seen more frequently around FUors than T Tauri stars. Shell formation may therefore be caused by time-dependent events in the outflow. Cross-cutting arcs within the shell structure, seen towards RNO 1B/1C and Elias 1-12, are probably ridges of gas swept-up by the most recent outbursts, confirming the repetitive nature of FUor outbursts. Estimates of the dynamical ages of the arcs suggest that the interval between outbursts is $\sim 5 \times 10^3$ and 1.3×10^4 years for RNO 1B/1C and Elias 1-12 respectively, consistent with previous estimates of FUor cycling times.

Comparable envelopes and shell-like outflow structure are seen towards embedded sources while envelopes surrounding T Tauri stars are smaller and less massive. This suggests FU Orionis objects are transition sources between deeply embedded and optically visible stars. The strength of the molecular outflow emission is correlated with the mass of the extended envelope; the outflow has evacuated molecular gas leaving less to be swept-up by subsequent outbursts, while envelope masses are smaller since less material is available for accretion.

Chemically, fractional abundances of SiO and methanol are enhanced towards RNO 1B/1C by over an order of magnitude. Methanol is enhanced relative to HCN and H_2CO towards Elias 1-12. Such large changes in fractional abundances must be caused by chemical processing. The SiO enrichments may be produced by sputtering or evaporation of dust grains in regions of directly shocked material or by chemical reactions of SiH_4 after sublimation from grain surfaces. Methanol enrichments are difficult to produce in strong shocks, and may be caused by low velocity grain-grain collisions. For RNO 1B/1C, evaporation of the entire methanol rich grain mantles seems to be required; while for Elias 1-12 mantle phase changes from an amorphous ice to a clathrate hydrate can be invoked, expelling the methanol, with smaller molecules remaining trapped in the clathrate. Such low velocity collisions probably occur in the turbulent shear zones surrounding the outflowing gas.

Table of Contents

List of Figures

Chapter 1:

List of Tables

CHAPTER 1

Introduction

The birth of stars in the Galaxy probably occurs in two distinct modes: stars are either born nearly simultaneously in a tight group or sporadically from loosely associated dense cores embedded within a molecular cloud.

It is currently believed that solar mass stars form by the latter method and that their evolution can be considered in terms of four conceptually distinct stages as shown in Figure 1.1 (Shu *et al.* 1993). Gas and dust slowly contract under self-gravity against the supporting forces supplied by magnetic fields forming an embedded source in about 10^6 years (Figure 1.1b)). When the structure becomes sufficiently centrally concentrated, the core begins to collapse from the inside out (Figure 1.1 b)). Angular momentum constraints initiate the formation of a centrifugally supported disk surrounding the protostar. Material accretes onto this disk from the infalling envelope before being accreted onto the central source. The infalling envelope is in turn replenished by gas and dust from the molecular cloud.

Recent modifications to this scenario involve detailed calculations incorporating the effects of magnetic fields. These suggest that a infalling "pseudodisk" several thousand AU in size, initially forms at the embedded stage. Similar structures are also predicted by the inviscid disk models of Stahler *et al.* (1994). The pseudodisk models, supported by observations of embedded sources and classical T Tauri stars, suggest infall envelopes are not spherical and that their mass decreases as the mass of the circumstellar disk grows (Ohashi *et al.* 1991; Galli & Shu 1993).

One of the least expected discoveries was that of *outflowing* gas (Figure 1.1 c)). Molecular line observations revealed a bipolar outflow from the young star L1551 (Snell *et al.* 1980). Early interpretations of the shell-like structure invoked an atomic wind sweeping-up molecular gas to form a cavity devoid of molecular material. However, this model cannot explain the lack of emission from the far-side of the cavity nor observations of molecular gas within the cavity (*cf* Bachiller & Gómez-González

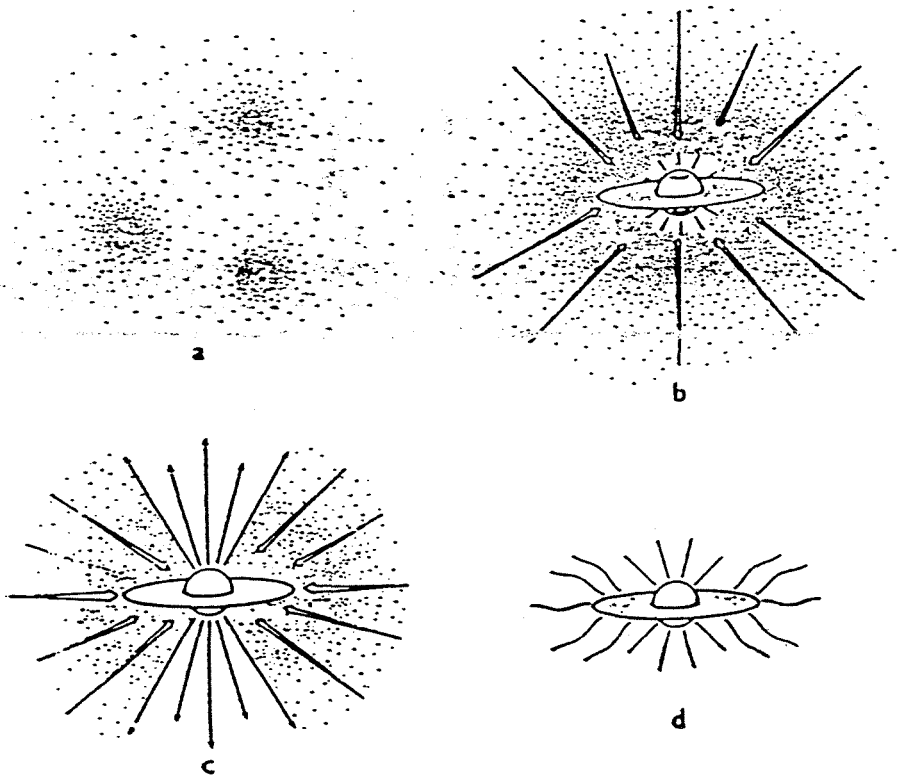

Figure 1.1. The formation of a planetary system can be envisioned as taking place in four stages. In a) gas and dust contract to form an cold embedded source; in b) a protostar with a surrounding nebular disk form at the center of the cloud core; in c) a stellar wind breaks out along the rotational axis of the system, creating a bipolar flow; in d) infall ceases revealing a newly formed star with a circumstellar disk from which planets form. Reproduced from Shu *et al.* (1993).

1992). A new interpretation is now emerging where outflows are driven by a collimated jet which entrains material in a bowshock, thereby creating a filled shell (Masson & Chernin 1993; Raga & Cabrit 1993; Stahler 1994).

As the system evolves, infall onto the circumstellar disk ceases and accretion onto the central star halts (Figure 1.1 d)). Micron sized dust particles settle to the disk mid-plane and aggregate to form larger particles. These grow to produce kilometer sized bodies, or planetesimals (Weidenschilling & Cuzzi 1993). Planets are formed by the pairwise accumulation of these small solid bodies (Lissauer & Stewart 1993). The evolution of the planetesimal size distribution is determined by the gravitationally enhanced collisional cross-section, which favors collisions between planetesimals with smaller velocities. Runaway growth of the largest planetesimal in each accretion zone is the probable outcome (Ohtsuki *et al.* 1993). The remaining gas disk is possibly removed by photoevaporation or other processes involving the young star.

Figure 1.1 suggests accretion and mass loss vary slowly and smoothly with time. However, changes in the strength of P Cygni profiles observed towards young stars indicate that mass loss rates vary on a timescale of hours. Luminosity variations in young stars suggest accretion rates are also highly time-dependent. The most spectacular time-dependent phenomena are exhibited by FU Orionis objects. Their luminosity increases by 5-6^m over over several months to decades, with a corresponding increase in mass accretion rates by a factor of one hundred.

1. Observational Characteristics of FU Orionis Objects

In 1938, FU Orionis rose by 6^m over a period of six months and has declined by $\sim 1^m$ since then exhibiting a unique spectral signature. Several other stars have been identified as FU Orionis objects (FUors) based on similar increases in luminosity or on their spectra alone. Their association with molecular clouds, strong lithium lines, reflection nebulae, and powerful winds suggests the stars are very young (*cf* Herbig 1977; 1989; Goodrich 1987; *cf* Hartmann *et al.* 1993). Indeed, a pre-outburst spectragram of V1057 Cygni is that of a strong-lined T Tauri star (Herbig 1958). The number of detected FUor outbursts suggests the phenomenon is repetitive, with stars in the T Tauri stage of evolution undergoing up to 100 outbursts over $\sim 10^6$ yrs (Herbig 1977, 1989; Hartmann 1992). FUor outbursts occur early in the history of the T Tauri star just after, or in the late stages of, the embedded phase (see Figure 1.2).

Although all FUors possess optical light curves similar to their namesake FU Orionis, rise times vary from six months to decades. Figure 1.3 shows the light curves for FU Orionis, V1057 Cygni, and V1515 Cygni which exhibit rise times of 6 months, $\sim$1 year, and 15 years respectively (Herbig 1977; Kenyon *et al.* 1991). Infrared measurements show a similar behavior but with a smaller magnitude increase. The increase in luminosity of a FUor usually reveals a pre-existing arc-shaped reflection nebula surrounding the central star (Goodrich 1987). Prior to an outburst FUors possess a spectrum of a strong-lined T Tauri star, while afterwards the spectrum is sufficiently unique to allow identification based solely on spectral characteristics (*cf* Hartmann *et al.* 1993). FUors exhibit a later spectral type with increasing wavelength, with their spectrum best described by that of an F or G supergiant with low surface gravity. Absorption lines, evident in Ca, Fe and Li lines, show a double peaked structure whose velocity width increases with frequency and

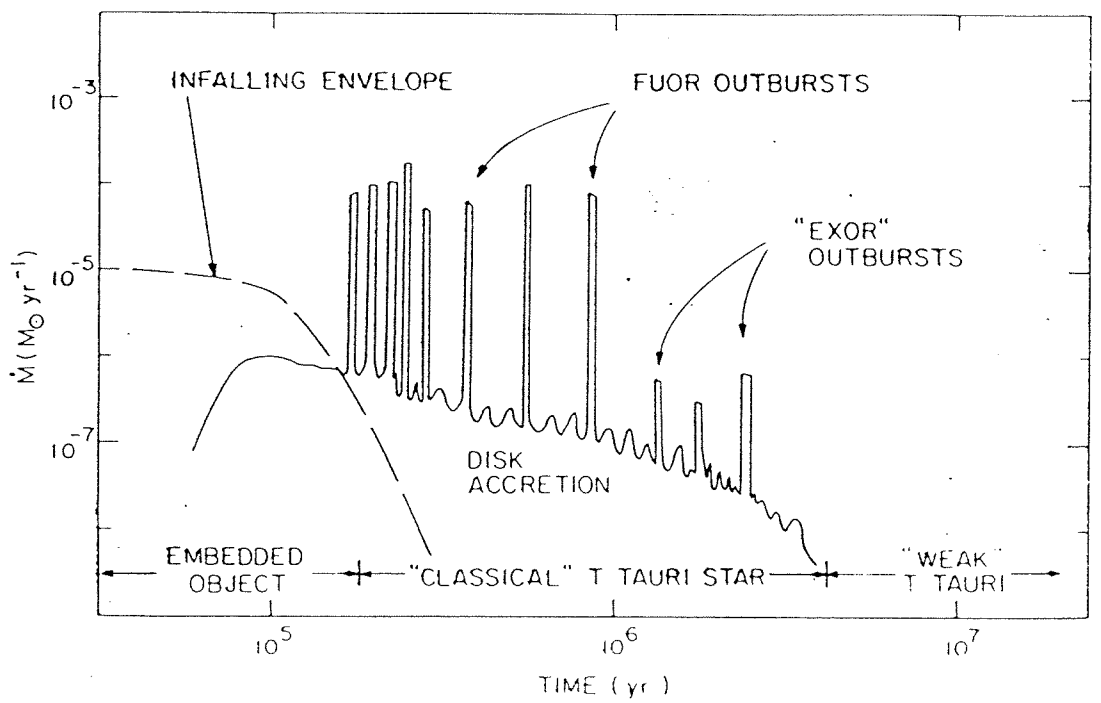

Figure 1.2. Figure from Hartmann *et al.* (1993) showing the variation of accretion rate with time for a young star. Mass from the circumstellar disk or surrounding envelope initially falls directly onto the star. Later accretion occurs through a circumstellar disk. The background accretion is supplemented by recurrent periods of very high $\dot{M}$ (FUor outbursts). Smaller outbursts occur as material begins to run out (Exor outbursts). Eventually accretion from the disk ceases (weak-lined T Tauri star).

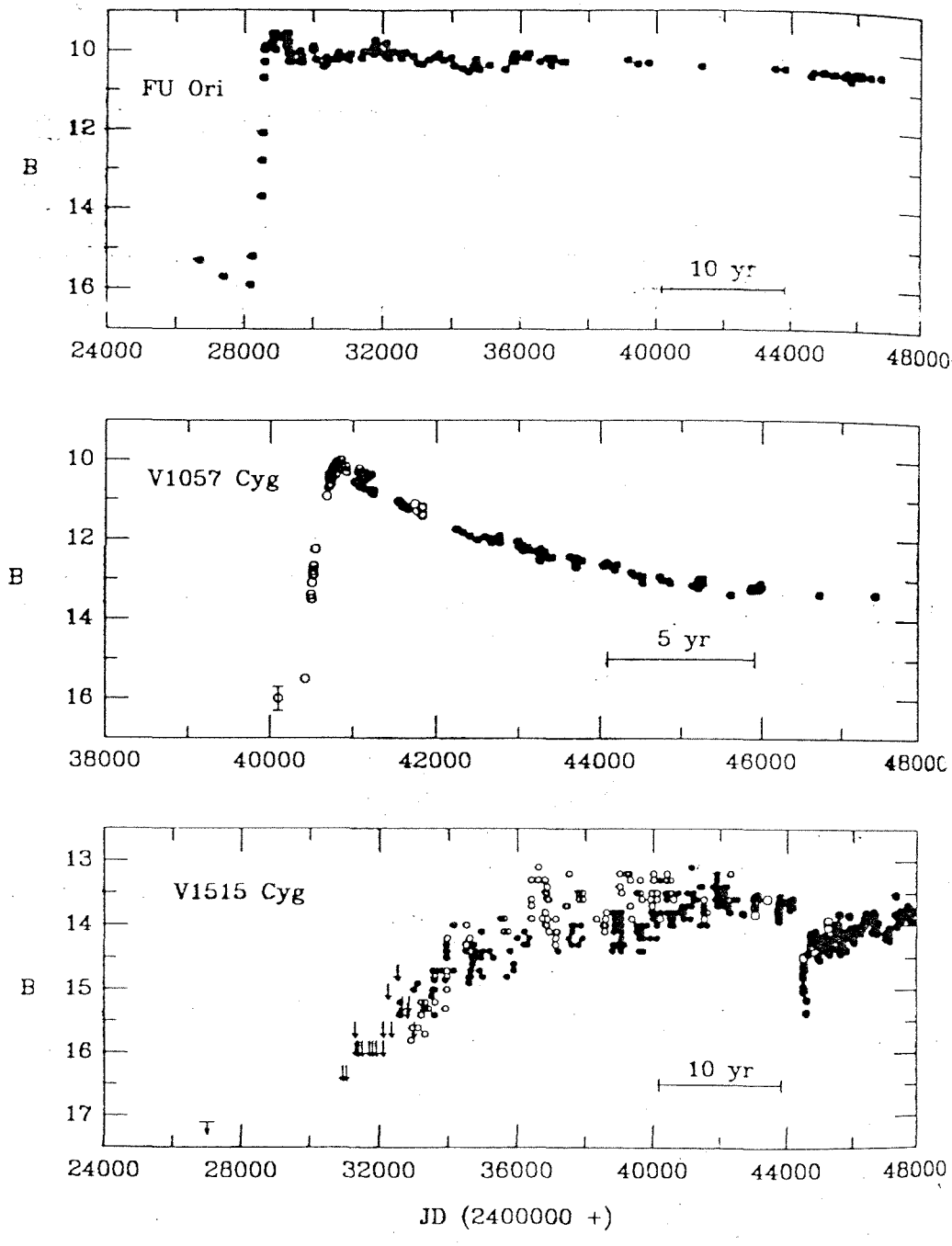

Figure 1.3. Light curves of FU Orionis, V1057 Cygni and V1515 Cygni (see Hartmann *et al.* 1993 and references therein.)

excitation temperature (Hartmann & Kenyon 1987a; 1987b; Welty *et al.* 1992). The Hα and Na I D lines show strong P Cygni profiles with a suppressed emission component and yield mass loss rates of 10^{-5} $M_{\odot}$ yr^{-1}, $\sim$100 greater than during T Tauri activity. Wind velocities are as large as $\sim$600 km s^{-1} (Bastian & Mundt 1985).

FUors possess infrared excesses that cannot be fit by isothermal blackbodies (Simon *et al.* 1972; Rieke *et al.* 1972). Their spectral energy distributions (SEDs) lie, in the classification scheme of Lada (1991), between Class I and II sources with a broad maximum in λF_{λ} centered roughly at 1 μm. Steady accretion disk models provide reasonable fits to data yielding disk masses of $\sim$0.03-0.1 $M_{\odot}$ for values of the dust emissivity index β=1-2 (Weintraub *et al.* 1991). Estimates of disk masses are highly dependent on the choice of the mass opacity (Beckwith & Sargent 1991), making comparisons with T Tauri stars difficult. FUors posses shallow temperature profiles indicative of young active disks. Excess emission exists between 10-20 μm (*cf* Simon & Joyce 1988) and 1-30 mm (Weintraub *et al.* 1989, 1991; Rodríguez *et al.* 1990). Models of the 1-100 μm excess emission suggest the circumstellar disk is surrounded by an infalling flattened dusty envelope that reprocesses light from the central object (Kenyon & Hartmann 1991). Depending on the viewing geometry, the inclination of the envelope may explain the variations in optical extinction seen towards different FUors. No high spatial resolution observations yet exist which can constrain envelope sizes or measure their kinematics directly.

The mass loss seen at optical wavelengths is also evident in the submillimeter and millimeter bands. Strong line wings seen in the rotational transitions of CO and ^{13}CO towards many FUors are indicative of outflow (Levreault 1985; Evans *et al.* 1994). Surprisingly, FU Orionis itself shows no evidence for outflowing molecular gas. Low resolution molecular line maps suggest outflow ages of $\sim 10^4$ years and yield average mass loss rates of $\sim 5 \times 10^{-7}$ $M_{\odot}$ yr^{-1} (Levreault 1988). Radio

continuum emission at centimeter wavelengths from FUors V1057, Elias 1-12, and RNO 1B/1C has a positive spectral index consistent with free-free emission from an ionized component of the outflow (Rodríguez *et al.* 1990; Anglada *et al.* 1994). Finally, transient OH and H_2O maser emission from V1057 Cygni together with maser emission from RNO 1B/1C also suggests vigorous outflow activity.

2. Modelling

2.1 Massive Accretion Disks

Any model of FUor outbursts needs to account for their characteristic spectral signature, the change in luminosity during an outburst, the variation in rise times between different sources, and the repetitive nature of the outbursts suggested by source statistics. Early explanations of the FUor phenomenon, including the rapid dissipation of a dust envelope and the the reorganization of the underlying star, have been superceded by models involving a massive circumstellar accretion disk (*cf* Hartmann *et al.* 1993). Outbursts occur when the disk becomes unstable resulting in an elevated accretion rate onto the central star. Massive accretion disks, whose presence is suggested by the FUor SEDs, can naturally account for the peculiar dependence of spectral type with wavelength and the observed double-peaked absorption features (Hartmann & Kenyon 1985). For a disk, with a radially decreasing temperature dependence, line widths are smaller at longer wavelengths since emission arises in the more slowly rotating outer sectors (Hartmann & Kenyon 1987a; Welty *et al.* 1992). Comparison of optical and infrared synthetic disk spectra with observations of V1057 Cygni and FU Orionis show good agreement (Kenyon *et al.* 1988). Disk models can fit FUor optical and infrared broad-band energy distributions with accretion rates of $\dot{M}\sim10^{-4}\ M_{\odot}\ \mathrm{yr}^{-1}$.

2.2 Outburst Initiation

Two main models exist to explain how FU outbursts are initiated. One class of models involve the influence of a stellar companion, which perturbs the massive circumstellar disk causing an elevated rate of accretion (Bonnell & Bastien 1992). However, it is not known if all FUors are members of binary systems. Alternatively, thermal instabilities within the disk may increase the rate of angular momentum transport and therefore the accretion rate onto the central star. The later model is

more favored since thermal instabilities naturally occur in massive accretion disks.

For a disk to accrete mass onto the central star it must transport angular momentum outward. Among the many proposed angular momentum transport mechanisms, viscous stress is considered the most likely (Pringle 1981). Since simple molecular viscosity is too small, a turbulent viscosity is usually invoked to allow the mixing of adjacent annuli permitting a net outward transport of angular momentum. Standard disk models use the *alpha* (α) prescription to describe the viscosity, an *ad hoc* functional form linking viscosity to the sound speed and the local pressure scale height (Shakura & Sunyaev 1973). Following the models success in explaining the episodic outbursts seen in cataclysmic variables, the α prescription has been applied to the FUor phenomenon (Hartmann & Kenyon 1985; Lin & Papaloizou 1985; Clarke *et al.* 1989, 1990; Bell & Lin 1994). Outbursts occur when sufficient mass builds up in the disk so that temperatures are high enough to ionize hydrogen (T_{crit} ~10000 K). This causes a thermal instability since opacity increases with ionization fraction. The effective viscosity, probably the result of either convective or magnetohydrodynamic instabilities within the disk, increases proportionally. More angular momentum is transported outwards through the disk while mass accretion onto the central star increases by a factor of a hundred.

Thermal instability models can reproduce the observed FUor light curves and time-scales (Bell & Lin 1994). Modeled ionization fronts propagate outward from the inner edge of the disk where they are initiated to several tens of stellar radii. The front's terminus is determined primarily by the mass infall rate and the mass of the central star. After the disk is depleted by a short (100 year) outburst, accretion rates revert to lower levels, and mass begins to accumulate in the disk until another outburst is initiated. FUor outbursts are therefore naturally self-regulating on time-scales of several thousand years.

3. Research Outline

3.1 Motivation

Although copious observations of T Tauri stars have been undertaken, FUors have only been studied extensively at optical and infrared wavelengths. These observations can trace emission from the hot inner disk and reflected light from surrounding material, but cannot delineate the morphology or kinematics of cold molecular gas. This is ideally done at millimeter wavelengths.

This thesis presents new high spatial resolution and high sensitivity millimeter observations of several FU Orionis objects. High spatial resolution observations of molecular line emission can, in principle, detect rotating or infalling gas. Emission at larger spatial scales can reveal outflow structure. Studies of outflowing gas should reveal the source's accretion history, since the accretion rate is correlated to the mass loss rate (Edwards *et al.* 1993), and thereby confirm if FUor outbursts are repetitive. Millimeter continuum observations are the best determinant of mass concentrations in embedded sources and, with sufficient spatial resolution, can examine if FUors are binary systems. Finally, line strengths of different molecular species, when input into radiative transfer codes, yield column densities and fractional abundances which can be compared to those in star forming molecular clouds and other young stellar objects (YSOs).

3.2 Observing Techniques

The spatial resolution of a telescope is proportional to the observed wavelength divided by the telescope diameter. At millimeter wavelengths, this necessitates using an antenna many tens to hundreds of meters across to obtain arcsecond resolution. To circumvent this engineering difficulty, aperture synthesis techniques are used. Signals from different antennas in an array are combined, having been corrected for path delay differences, to produce a telescope with an effective diameter equal to the largest

separation between two elements. This array measures the fourier transform of the brightness distribution on the sky which when transformed yields an emission map.

Aperture synthesis techniques yield maps with high spatial resolution and accurate pointing, but are time consuming to produce. Any constant background or extended emission is also resolved out by the telescope. Although this is advantageous for embedded objects such as young stars, it must be remembered that only a fraction of the available flux is mapped. Filled aperture techniques using single dish telescopes measure all the flux, but at lower spatial resolution. Only by using both aperture synthesis and filled aperture techniques is it possible to obtain an unbiased description of a source. Observations were therefore made of molecular line and associated continuum emission utilizing the Owens Valley millimeter-wave array in the 1.3 and 2.6 mm bands and the Caltech Submillimeter Observatory (CSO) at 230 and 345 GHz.

3.3 Source Sample

Seven FUors were known to exist in the northern hemisphere at the start of this study. All but L1551, which is described extensively elsewhere (Snell *et al.* 1980; Snell & Schloerb 1985; Moriarty-Schieven *et al.* 1987; Uchida *et al.* 1987; Moriarty-Schieven & Snell 1988; Bachiller *et al.* 1994), were included in the source sample. Sources were classified as FUors based on both their light curves and spectral characteristics. FUors FU Orionis, V1057 Cygni, Elias 1-12 (V1735 Cygni), and V1515 Cygni have undergone dramatic increases in luminosity (*cf* Hartmann *et al.* 1993). The young stars RNO 1B/1C both show the spectral characteristics of FUors. Observations of the surrounding nebula suggests one of the stars has also increased in brightness. Also included is the pre-outburst object V1331 Cygni, a T Tauri star exhibiting a spectrum similar to that of V1057 Cygni prior to outburst. Each object is described in an individual chapter. Chapters 2-4 are presented in a style compatible with submission to a journal. Overall characteristics and the implications

for FU Orionis outbursts are discussed in the final chapter.

CHAPTER 2

The Circumstellar Environment of the FU Orionis Pre-Outburst Candidate V1331 Cygni

The Circumstellar Environment of the FU Orionis Pre-Outburst Candidate V1331 Cygni

STUART MCMULDROCH
Division of Geological and Planetary Sciences, 170-25
California Institute of Technology
Pasadena, CA 91125
Electronic mail: sxm@sol1.gps.caltech.edu

ANNEILA I. SARGENT
Division of Physics, Mathematics, and Astronomy
California Institute of Technology, 105-24
Pasadena, CA 91125
Electronic mail: afs@mmstar.caltech.edu

GEOFFREY A. BLAKE
Division of Geological and Planetary Sciences, 170-25
California Institute of Technology
Pasadena, CA 91125
Electronic mail: gab@csardas.gps.caltech.edu

Published in: *The Astronomical Journal*, 106, 2477 (1993)

Abstract

High resolution (∼4″) aperture synthesis maps of the CO (1→0), ^{13}CO (1→0), ^{13}CO (2→1), and associated continuum emission from the FU Orionis candidate V1331 Cygni reveal a massive, 0.5±0.15 $M_\odot$, circumstellar disk surrounded by a flattened gaseous envelope, 6000 × 4400 AU in size, and of mass at least 0.32 $M_\odot$. These images from the Owens Valley millimeter-wave array along with lower resolution measurements from the Caltech Submillimeter Observatory also trace a bipolar outflow and gaseous ring, 4.1 by 2.8 × 10^4 AU, mass ≥0.07 $M_\odot$, radially expanding at 22±4 km s^{-1}. We suggest this ring is a swept-up gaseous torus from an energetic mass ejection stage, possibly an FU Orionis outburst or outbursts, that took place about 4 × 10^3 years ago and imparted more than 10^{45} ergs into the ambient cloud.

1. Introduction

Beginning in 1936, FU Orionis, a little-studied star in Orion, rose in brightness from about 16^m to 10^m over a period of half a year (Wachmann 1939). Since then, several other stars have exhibited similar behavior, most notably V1057 Cygni. These FU Orionis objects (FUors) have distinctive spectral signatures; their Balmer lines exhibit P Cygni profile with a suppressed emission component, while absorption line widths and spectral types vary with wavelength and often show double-peaked profiles (Herbig 1977, 1989; Hartmann & Kenyon 1987a; Reipurth 1990; Petrov & Herbig 1992; Welty *et al.* 1992; Hartmann *et al.* 1993). Several stars have been classified as FUors solely on the basis of their spectra (Mundt *et al.* 1985; Carr *et al.* 1987; Eislöffel *et al.* 1990; Staude & Neckel 1991).

Pioneering work by Hartmann and Kenyon (1985; 1987a) explains many of the observed properties of FUors in terms of accretion through a circumstellar disk onto a T Tauri star; outbursts result when the disk becomes unstable, producing an elevated accretion rate (see also Calvet *et al.* 1991; Hartmann 1992; Hartmann *et al.* 1993). For a few objects, optical and near infrared spectral line profiles suggest that the disk material moves in Keplerian orbits (Hartmann & Kenyon 1987a; Welty *et al.* 1992). Little is known about the pre-outburst nature of FUors, although a pre-outburst spectrogram of V1057 Cygni identifies it as a strong-lined T Tauri star (Herbig 1958). The frequency of detected FUor eruptions suggests that in the T Tauri phase a star may undergo up to 100 outbursts, although this conclusion is based on small sample statistics (Herbig 1977, 1989; Hartmann 1992).

V1331 Cygni is a luminous ($\sim$53 $L_\odot$) T Tauri star, with visual extinction A_v $\sim$2.4, at a distance of 550 pc (Shevchenko *et al.* 1991). Although other distances have been adopted, here all properties are scaled to 550 pc. The similarity of the spectrum of V1331 Cygni to that of V1057 Cygni prior to maximum light, with the K

line of Ca II (3933 Å) strong in emission and the H line (3968 Å) absent, may signify an impending FUor outburst (Welin 1976, Herbig 1989). Optical emission line profiles imply a moderate mass loss rate of 7×10^{-8} $M_\odot$ yr^{-1} to 3×10^{-6} $M_\odot$ yr^{-1}, much less than the large rates exhibited by FUors, typically $\sim 10^{-5}$ $M_\odot$ yr^{-1} (Chavarria 1981; Croswell *et al.* 1987). There is also evidence for a molecular outflow with a mass loss rate of 1.0×10^{-7} $M_\odot$ yr^{-1} (Levreault 1988). Submillimeter continuum observations suggest the presence of a circumstellar disk (Weintraub *et al.* 1991).

If V1331 Cygni is indeed a pre-outburst, or between outbursts, FUor, its circumstellar environment may retain some record of a previous event. The dramatic heating of a FUor outburst could, for example, result in an unusual chemical environment. Additionally, the increased mass loss episode may be reflected in the kinematics of the circumstellar gas. Here we present high resolution (2″.2 – 5″.9) aperture synthesis maps of V1331 Cygni in the CO (1→0), ^{13}CO (1→0) and ^{13}CO (2→1) transitions, along with measurements of the dust continuum emission at λ=1.3 mm and λ=2.6 mm. These observations trace the small scale density and temperature fluctuations in the circumstellar gas and dust. We have also acquired single dish observations of several CO isotopes to determine optical depths, and have mapped the CO (2→1) emission at $\sim$30″ resolution to image the larger-scale circumstellar environment.

2. Observations

2.1 Owens Valley

Aperture synthesis mapping of the J=1→0 rotational transitions of ^{12}CO and ^{13}CO, as well as the J=2→1 transition of ^{13}CO at ν = 115.271, 110.201, and 220.399 GHz respectively, was carried out using the Owens Valley millimeter-wave array between 1990, October and 1991, June. Each of the three 10.4 m diameter telescopes was equipped with an SIS receiver, cryogenically cooled to 4 K. System temperatures were typically 390 K (SSB) at 110 GHz, 850 K (SSB) at 115 GHz and 740 K (SSB) at 220 GHz. Two filter banks, 32 × 1 MHz and 32 × 50 kHz, each centered on the CO velocity in the direction of the star, v_{LSR} = −0.7 km s^{-1} (Levreault 1985), provided velocity resolutions of 2.7 and 0.14 km s^{-1}, 2.6 and 0.13 km s^{-1}, and 1.3 and 0.07 km s^{-1} at 110.201, 115.271, and 220.399 GHz, respectively. Simultaneous continuum observations were obtained in a broadband channel of effective width 375 MHz, centered on the systemic velocity.

The phase and amplitude gains were calibrated by observing the quasar BL Lac at 25 minute intervals, and the absolute flux scale was established by measurements of Neptune and Uranus. Maps were generated from calibrated visibility data using the NRAO AIPS software package. Positional accuracy is ± 2″. At 110.201 GHz and 220.399 GHz, maximum unprojected baselines of 140 m north-south and 200 m east-west gave naturally weighted synthesized beams of 4″.4 ×4″.1 at PA −30° and 3″.6 ×2″.3 at PA −25°. At 115.271 GHz, maximum baselines of 100 m north-south and 100 m east-west resulted in a naturally weighted beam of 5″.9 × 5″.2 at PA −5°. For these beams, T_B = 1 K corresponds to 0.18 Jy/beam, 0.32 Jy/beam and 0.33 Jy/beam respectively. The phase center of the maps is α (1950) = $20^h\ 59^m\ 32.21^s$, δ (1950) = +50° 09′ 55″.5, the position of V1331 Cygni given by Herbig & Robbin Bell (1988).

2.2 CSO Observations

Single dish observations were carried out at the Caltech Submillimeter Observatory (CSO) on Mauna Kea, Hawaii, in 1991, July and 1992, August. The facility 230 GHz and 345 GHz SIS heterodyne receivers were used in conjunction with the CSO 500 MHz and 50 MHz bandwidth acousto-optical spectrometers (Ellison & Miller 1987; Ellison *et al.* 1989). Calibration was accomplished by the standard chopper wheel method, while main beam efficiencies were calculated to approximately 20% accuracy from measurements of Jupiter. At 230 GHz and 345 GHz, the beamwidths were 31″ and 21″ (FWHM), with main beam efficiencies of 0.52 and 0.58, respectively.

Although a number of molecular species were searched for towards V1331 Cygni in the 230 GHz band, only CO and its isotopes were detected towards to a 2σ rms noise limit of ~180 mK. Spectra were acquired for the J=2→1 rotational transitions of CO, ^{13}CO, and C^{18}O, as well as the CO J=3→2 transition. In addition, CO (2→1) emission was mapped on a 150″ × 150″ grid, sampled every 10″, centered on V1331 Cygni. Position switching to a reference position at $\alpha = 20^h\ 56^m\ 43^s$, $\delta = +50°\ 09'\ 55''.5$ produced the least contaminated baselines. Pointing was checked regularly on planets and nearby point sources; absolute positions are accurate to within 5″, relative positions within the maps to ~2″.

3. Results

3.1 Owens Valley Results

Dust continuum emission from V1331 Cygni is unresolved in the 3″.6 × 2″.2 beam at 1.3 mm, indicating a source size less than 2000 AU. Emission appears centered on the star with fluxes of 33 mJy at 2.7 mm and 175 mJy at 1.3 mm.

Figures 2.1 (a) and (b) show the CO (1→0) and ^{13}CO (1→0) emission from V1331 Cygni in the 50 kHz channels integrated over the velocity ranges −0.84 to +0.74 km s^{-1} and −0.97 to +0.25 km s^{-1} (V_{LSR}) respectively. No flux was detected outside these velocity ranges to 3σ limits of 1.5 Jy/beam and 0.15 Jy/beam for CO and ^{13}CO respectively. The ^{13}CO (2→1) emission integrated between −1.21 and +0.12 km s^{-1} is shown in Figure 2.1 (c). No emission was detected outside this velocity range to a 3σ limit of 0.9 Jy/beam. All emission regions appear extended with deconvolved sizes of 5500 × 2750, 6050 × 4400, and 2750 × 2200 AU for CO (1→0), ^{13}CO (1→0), and ^{13}CO (2→1). Within the positional uncertainties, emission in each transition peaks at the star.

The total integrated fluxes for the emission regions depicted in Figures 2.1(a)-(c) are 17, 8, and 22 Jy km s^{-1}. Following Scoville *et al.* (1986), the mass of H_2 implied in each case is given by:

$$M_{H_2} = 2.19 \times 10^{-9} \frac{(T_x + 0.93)}{e^{-5.53/T_x}} \frac{\tau_{CO}}{(1 - e^{-\tau})} \frac{D^2_{kpc}}{X(CO)} \int S_\nu dv \qquad M_\odot, \quad (1)$$

$$M_{H_2} = 2.39 \times 10^{-9} \frac{(T_x + 0.89)}{e^{-5.31/T_x}} \frac{\tau_{^{13}CO}}{(1 - e^{-\tau})} \frac{D^2_{kpc}}{X(^{13}CO)} \int S_\nu dv \qquad M_\odot, \quad (2)$$

$$M_{H_2} = 1.71 \times 10^{-10} \frac{(T_x + 0.89)}{e^{-15.92/T_x}} \frac{\tau_{^{13}CO}}{(1 - e^{-\tau})} \frac{D^2_{kpc}}{X(^{13}CO)} \int S_\nu dv \qquad M_\odot, \quad (3)$$

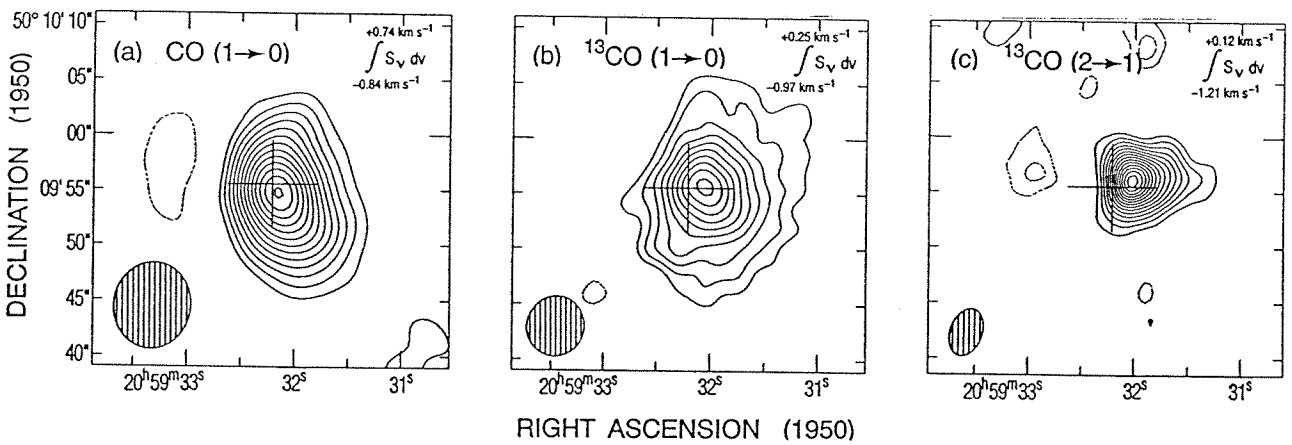

Figure 2.1. a) A map of the CO (1→0) emission integrated between V_{LSR}=−0.84 and +0.74 km s^{-1}. Contours start at the 2σ level, 1.0 Jy/beam km s^{-1}, and are separated by 0.50 Jy/beam km s^{-1}. In all maps, a hatched ellipse denotes the synthesised beam (FWHM), and a cross, 8″ in size, marks the position of the star (Herbig and Robbin Bell, 1988). b) A map of the ^{13}CO (1→0) emission around V1331 Cygni integrated between −0.97 and +0.25 km s^{-1}. Contours are separated by 1σ, 0.15 Jy/beam km s^{-1}, starting at 0.30 Jy/beam km s^{-1}. c) A map of ^{13}CO (2→1) emission integrated from −1.21 to +0.12 km s^{-1}. Contours begin at the 2σ value, 1.0 Jy/beam km s^{-1}, and are spaced by 0.50 Jy/beam km s^{-1}.

where Equations 2.1-2.3 apply to CO (1→0), ^{13}CO (1→0), and ^{13}CO (2→1) line emission respectively. Here, T_x is the excitation temperature, τ is the optical depth determined from line intensity ratios, D is the source distance in kiloparsecs, X is the molecular abundance relative to hydrogen, and $\int S_\nu$ dv is the integrated flux in units of Jy km s^{-1}. We adopt abundances of X(CO)=10^{-4}, X(^{13}CO)=1.7 $\times$ 10^{-6} (Chackerian & Tipping 1983; Langer & Penzias 1993) and assume that the excitation temperature, as approximated by the kinetic temperature, is 25 K. For these values, the calculation is relatively insensitive to temperature - a 5 K difference corresponds to a 20% change in mass. As all lines are optically thick, mass estimates are lower limits only. We calculate minimum masses of 0.32, 0.18, and 0.05 $M_\odot$ for CO (1→0), ^{13}CO (1→0), and ^{13}CO (2→1) respectively. This implies a minimum average density of $n_{H_2} \geq 3 \times 10^5$ cm^{-3} for these masses and source sizes.

Naturally weighted, 1 MHz channel maps of the CO (1→0) emission from V1331 Cygni between −9.8 km s^{-1} and +11.0 km s^{-1} are presented in Figure 2.2. Outside this velocity range, no emission above a 3σ limit of 135 mJy/beam is seen. Near the stellar position, emission is evident from −2.0 to +11.0 km s^{-1}. At distances of up to 50″, two elongated structures extend radially away from the star, concentrated towards PA −25° and 230°. To the northwest, emission is seen between −7.2 and −4.6 km s^{-1}, to the southwest between +0.6 to +8.4 km s^{-1}.

Contours of the CO (1→0) emission, integrated between velocities of −11.1 and −3.3 km s^{-1}, are shown in Figure 2.3(a). A greyscale image of this emission is also shown in Figure 2.3(b) together with contours of the CO (1→0) emission at velocities between +1.9 km s^{-1} and +7.1 km s^{-1}. The greyscale image in Figure 2.3(a), kindly obtained by Nick Weir at the Palomar 60 inch telescope, shows r-band emission in the reflection nebulosity surrounding V1331 Cygni. At blueshifted velocities, CO (1→0) emission lies to the south and east of the star, and at redshifted velocities to the

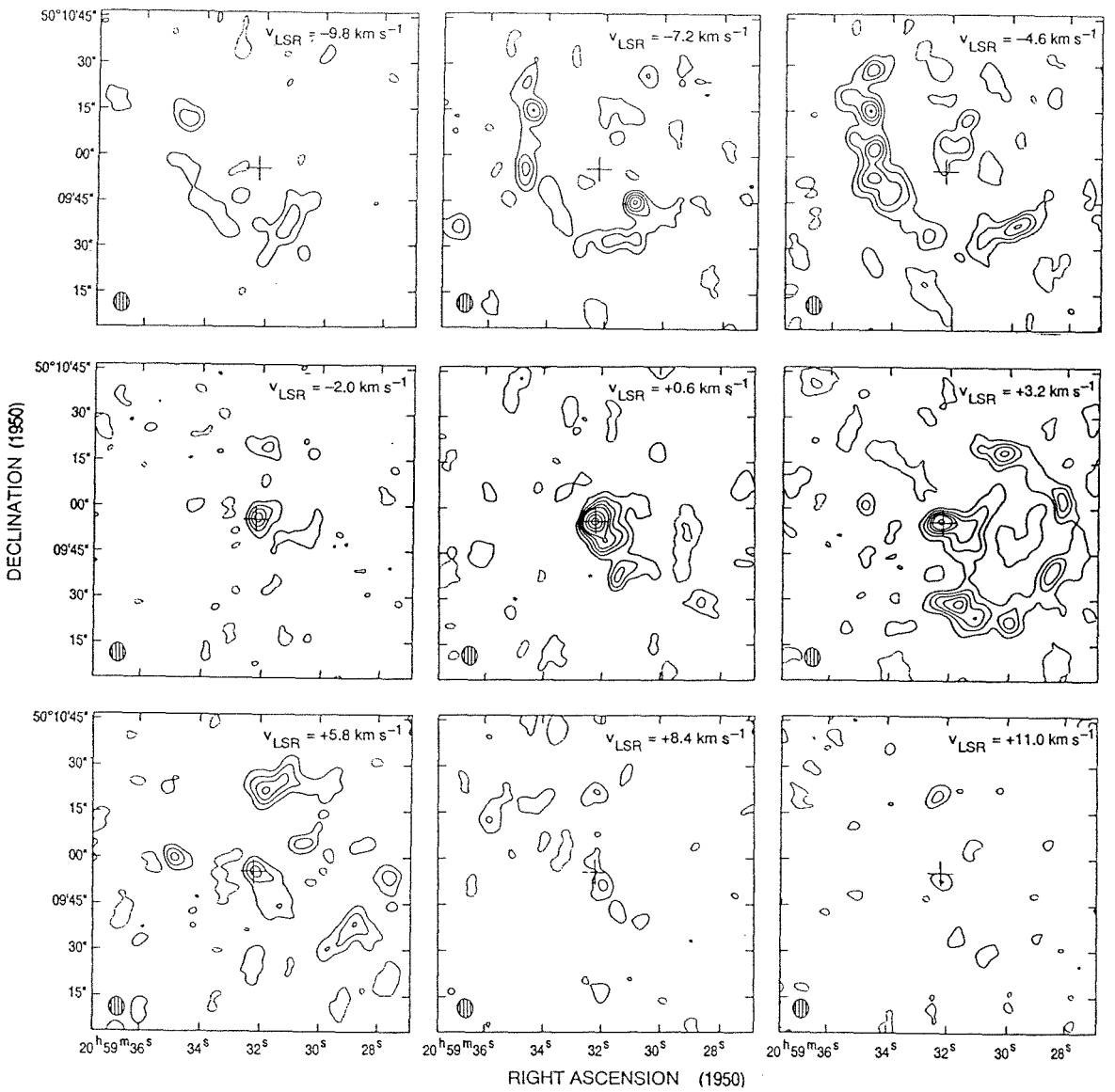

Figure 2.2. Aperture synthesis maps showing the distribution of CO (1→0) emission in individual 1MHz channels. The mean velocity for each map is shown in the top right corner. The peak flux occurs in the velocity range -0.7 km s^{-1} to +1.9 km s^{-1} and is 2.84 Jy/Beam. Contours begin at, and are separated by 2σ, 0.24 Jy/beam.

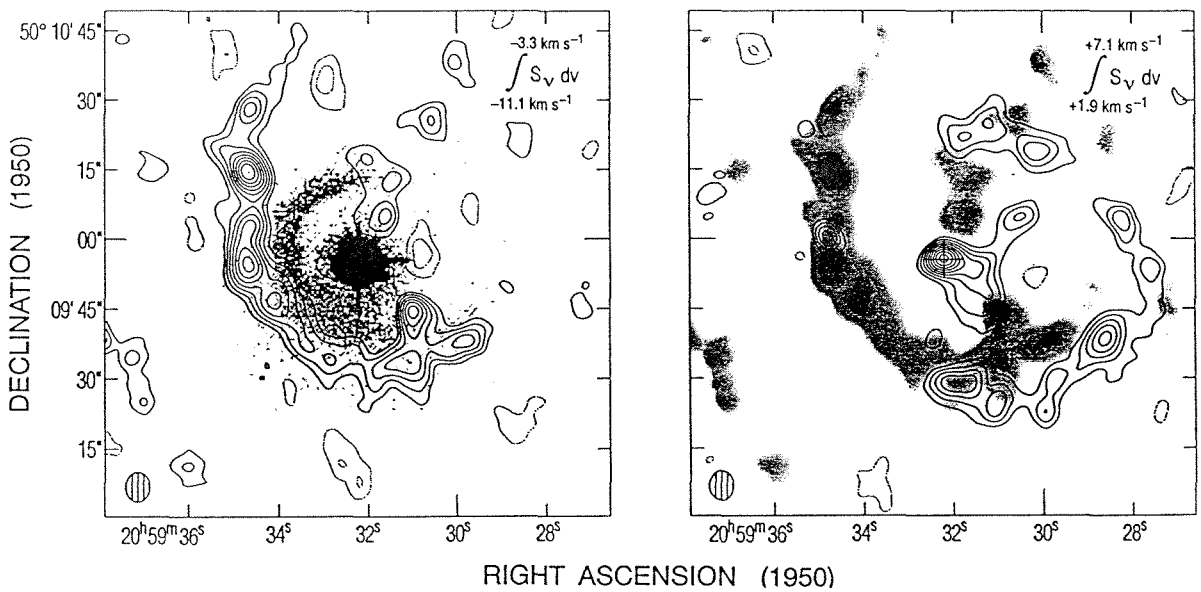

Figure 2.3. Contour maps of the CO (1→0) emission integrated over the velocity ranges -11.1 to -3.3 km s^{-1} (a) and $+1.9$ to $+7.1$ km s^{-1} (b). Optical r-band emission from the reflection nebulosity is depicted in greyscale in (a). CO emission in (a) is shown as a greyscale image in (b) for comparison. The rms noise level, 1σ, is 0.50 Jy/beam km s^{-1}. Contours are at 20, 30, 40, 40, 50, 60, 70, 80, and 90% of the peak flux, 6.7 Jy/beam km s^{-1}.

north and west. Taken together, these regions resemble an elliptical ring, 75″ × 50″ (4.1 by 2.8 × 10^4 AU) in size, with the semi-major axis orientated along PA∼40°. The reflection nebulosity and the CO ring emission appear similar in form, with the nebula lying closer to the star. Within the ring the gas appears distributed in clumps of typical size 9″ × 5″ (5.0 by 2.8 × 10^3 AU). The lack of observed ^{13}CO (1→0) ring emission limits the CO optical depth to $\tau_{CO} \leq 7$. We adopt a minimum excitation temperature of 10 K, as indicated by the peak brightness temperatures. Masses, calculated from Equation 2.1, are 8–52 x 10^{-3}, 6–42 x 10^{-3}, and 1–7 x 10^{-3} $M_\odot$ for the blue arc, red arc, and a typical clump respectively in the limits of $\tau << 1$ and $\tau \leq 7$.

3.2 CSO Results

Emission from V1331 Cygni was detected in four molecular lines at the CSO, namely the J=2→1 transitions of CO, ^{13}CO, and C^{18}O, and the J=3→2 transition of CO. Spectra, corrected for main beam efficiencies, are displayed in Figure 2.4. The CO (2→1) peak brightness temperature, T_{MB} ∼4.8 K, occurs at 0.27±0.32 km s^{-1}. Wing emission extends to −10 and +20 km s^{-1} with a dip in the blueshifted emission occurring at −2.2 km s^{-1}. The CO (3→2) spectrum is similar, albeit weaker, with peak T_{MB}=3.9 K at 0.17±0.21 km s^{-1}. By contrast, the ^{13}CO (2→1) spectrum, with peak T_{MB}=4.1 K at −0.13±0.33 km s^{-1}, displays no redshifted and only weak blueshifted wing emission. ^{13}CO (2→1) emission 15″ to the east does, however, possess a weak redshifted wing. The C^{18}O (2→1) spectrum shows no wing emission with the peak of T_{MB}=0.83 K occurring at a comparatively lower velocity of −1.31±0.34 km s^{-1}. Relative line intensities suggest that CO and ^{13}CO emission is optically thick in the line center but that C^{18}O (2→1) is optically thin, with $\tau_{C^{18}O}$ ∼0.25. The dip in CO emission, centered near the velocity of the C^{18}O peak, most likely arises from self-absorption. Ratios of the CO/^{13}CO line strength suggest

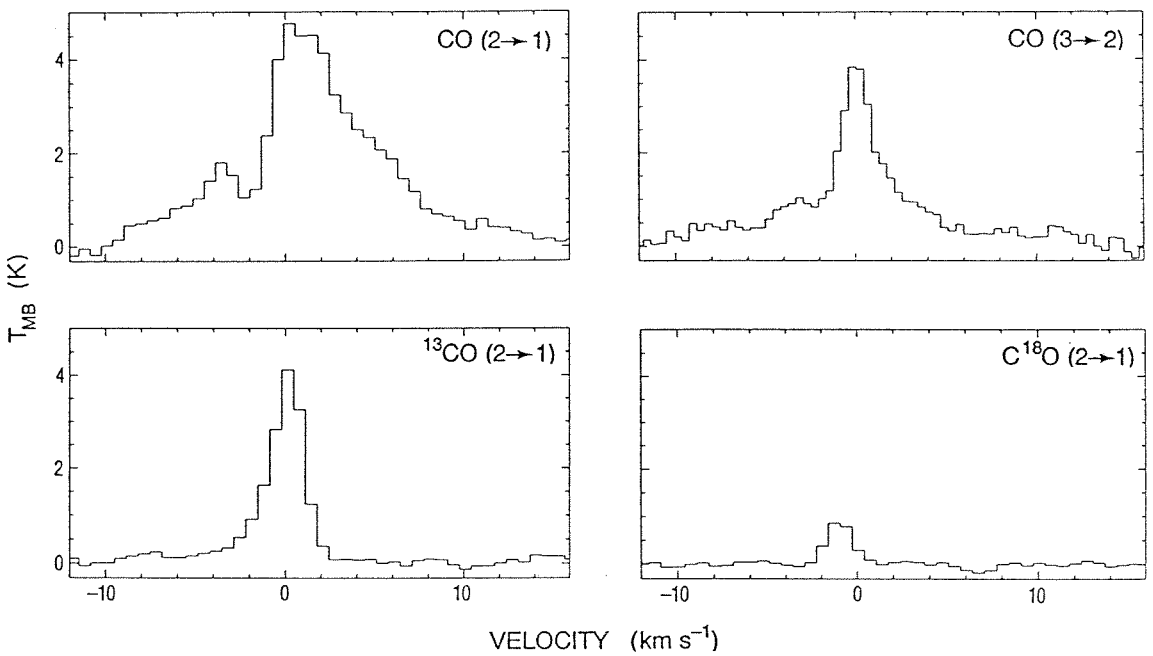

Figure 2.4. Line emission in CO (2→1), CO (3→2), ^{13}CO (2→1), and C^{18}O (2→1), as detected at the CSO. Temperatures have been corrected for main beam efficiencies.

that blueshifted CO (2→1) wing emission between −4 and −8 km s^{-1} possesses an average optical depth τ_{CO} ∼15. As the optical depth of the redshifted wing emission is poorly constrained, we adopt a maximum τ_{CO} ≤15 for both wings in our outflow calculations.

CO (2→1) line emission was mapped at 10″ spacings over a region 150″ × 150″ centered on V1331 Cygni. At velocities between −1.0 and +1.0 km s^{-1}, gas is concentrated at the stellar position; strong extended emission that was resolved out by the interferometer is evident between −4.5 and +2.5 km s^{-1}. Emission is also seen extending radially away from the star to the northwest between −2.0 and −0.75 km s^{-1} and to the south between +1.0 and +2.5 km s^{-1}. Significant gas structure is also present away from the cloud velocity at larger blue and redshifted velocities. Figure 2.5 (a) shows the blueshifted emission structure at velocities between −9.5 and −4.0 km s^{-1} which compares well with the arc in the CO (1→0) image (Figure 2.3 (a)). Likewise, the redshifted emission between +2.0 and +6.0 km s^{-1} (Figure 2.5(b)) resembles the structure in Figure 2.3 (b). In both cases the CO (2→1) emission is stronger and more extended with total integrated fluxes of 620 Jy km s^{-1} and 2000 Jy km s^{-1} for the blue and red arcs, respectively. Because the emission fills the beam, Equation 2.4 can be used to estimate the H_2 mass:

$$M_{H_2} = 1.42 \times 10^{-10} \frac{(T_x + 0.93)}{e^{-16.76/T_x}} \frac{\tau_{CO}}{(1 - e^{-\tau})} \frac{D_{kpc}^2}{X(CO)} \int S_\nu dv \qquad M_\odot, \qquad (4)$$

where parameters are as described for Equations 2.1–2.3. For an excitation temperature of 10 K and τ_{CO} ≤15, we calculate masses of 0.23 and 0.31 $M_\odot$ for the blue and redshifted emission seen in Figures 2.5(a) and (b). Comparison of the derived masses suggests the interferometer has resolved out more than 85% of the single dish flux in the red arc, but less than 50% in the blue arc.

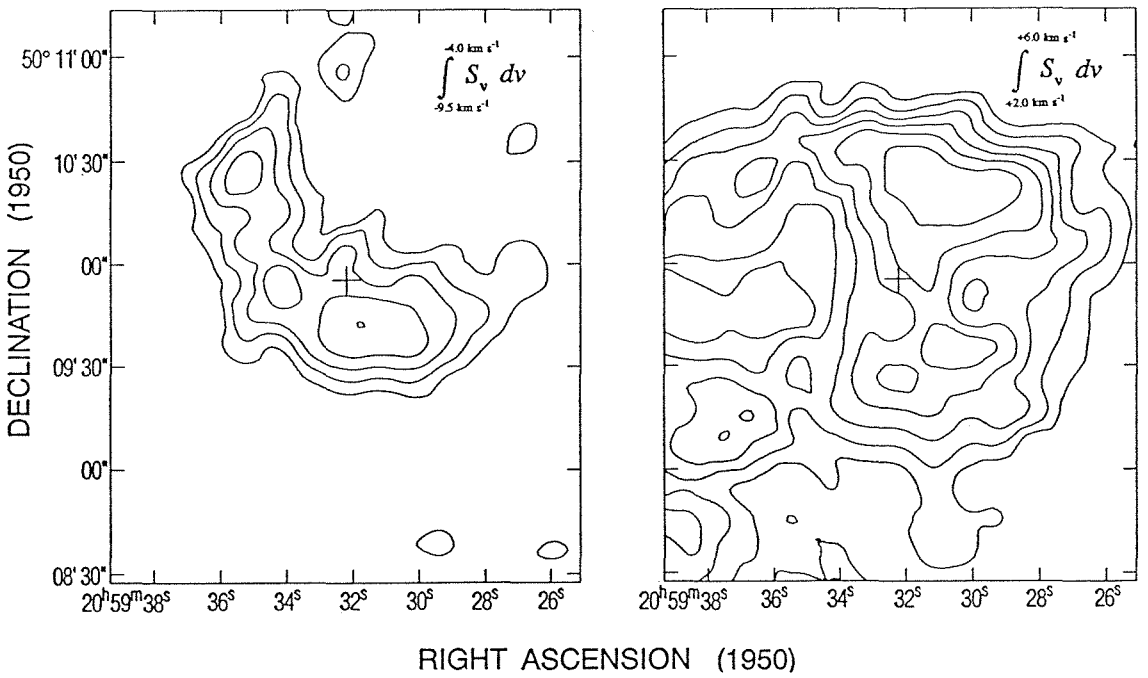

Figure 2.5. Maps of the CO (2→1) emission observed at the CSO integrated over the velocity ranges −9.5 to −4.0 km s^{-1} (a) and +2.0 to +5.0 km s^{-1} (b). Contours are separated by 10% of the peak flux, 10.9 K km s^{-1}, and begin at 30% in (a) and at 50% in (b).

4. Discussion

4.1 The Central Source

Models of the far-infrared and submillimeter spectral energy distribution of V1331 Cygni are consistent with the presence of a circumstellar accretion disk (Weintraub *et al.* 1991). Our longer wavelength continuum measurements can further constrain the disk parameters. Following Beckwith *et al.* 1990, our observations together with those from Weintraub *et al.* and the *IRAS* satellite were modelled as radially averaged emission arising from a disk. We fit power law dependences for density (p=1.5) and temperature (q=0.49) over a radius range of 0.055 AU to 125 AU and find a disk mass of M=0.50±0.15 $M_{\odot}$, with emissivity index β = 1.0± 0.2, assuming a temperature at the disk's inner radius of 1500 K. Our fit to the spectral energy distribution is shown in Figure 2.6 together with that of Weintraub *et al.*; the latter predicts higher fluxes at lower frequencies. We stress that absolute disk mass estimates are accurate only to within an order of magnitude and are sensitive to the assumed mass opacity coefficient (Draine 1989; Beckwith *et al.* 1990; Beckwith & Sargent 1991). For example, Weintraub *et al.* adopt a mass opacity coefficient κ_0=2.0 cm^2 gm^{-1} at 350 μm, while here we adopt 0.1 cm^2 gm^{-1} at 250 μm (*cf* Beckwith & Sargent 1991). Provided κ_ν does not vary significantly with evolutionary state, our result of M=0.5±0.15 implies a considerably more massive disk than those found around classical T Tauri stars (HL Tau $\sim 0.1 M_{\odot}$).

In Figures 2.1 (a)-(b), CO and ^{13}CO (1→0) emission trace a gaseous envelope, ~6000 × 4400 AU in size, mass ≥0.32 $M_{\odot}$, centered near the position of V1331 Cygni. If distributed spherically, this envelope would produce a visual extinction greater than 21^m. This is much larger than the observed value, 2.4, suggesting the gas lies in a flattened structure. This molecular disk or envelope appears smaller (2750 × 2200 AU) in ^{13}CO (2→1) emission (Figure 2.1 (c)), possibly because the

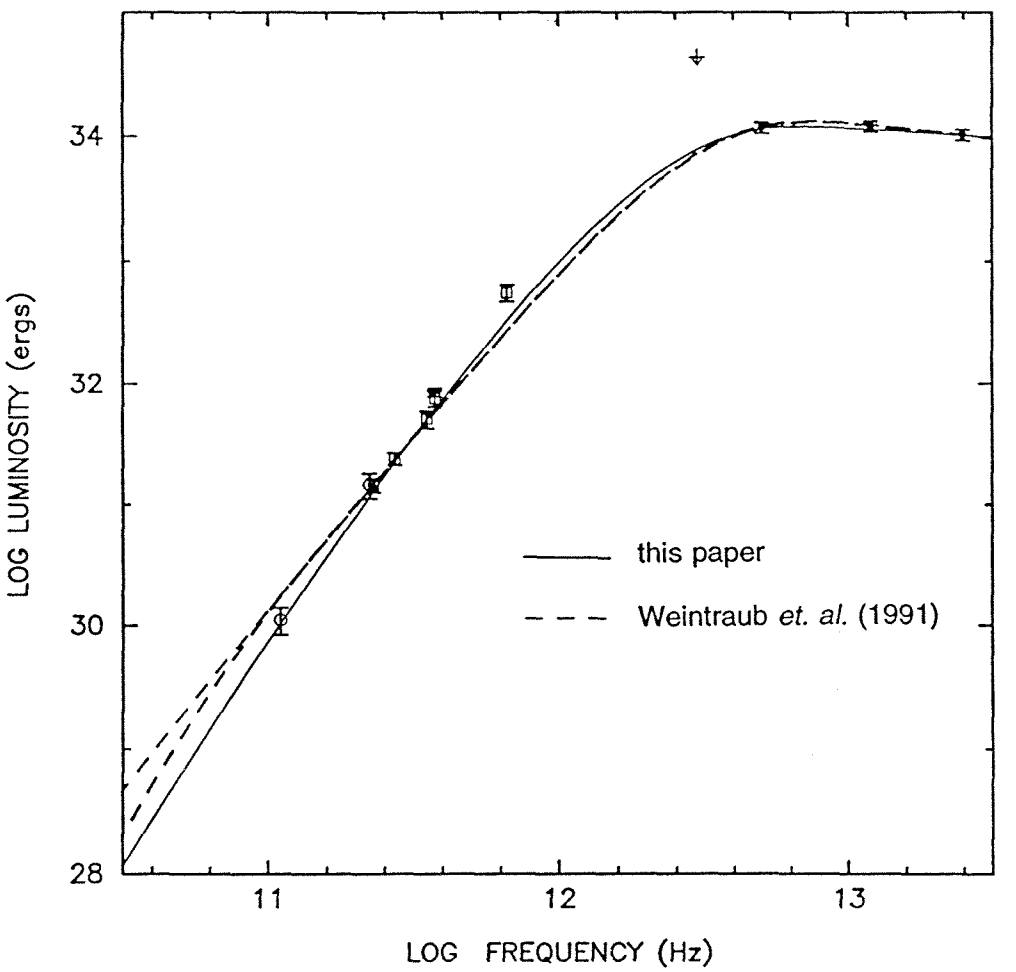

Figure 2.6. The spectral energy distribution of V1331 Cygni with our model disk fit depicted with a solid line. A broken line shows the fit from Weintraub *et al.* (1991). Data points represented by filled circles, squares, and empty circles are from *IRAS*, Weintraub *et al.* (1991), and this paper respectively.

smaller beam resolves out more extended emission. Excitation and optical depth effects may also localize the emission nearer the star. The CO (1→0) and CO (2→1) maps suggest that the line core emission in single dish spectra (Figure 2.4) arises from this envelope. Emission peaks at higher velocities as the optical depth of the transition increases, suggesting collapse. However, in the optically thick CO (2→1) spectrum, redshifted wing emission is dominant, indicative of outflow (Zhou *et al.* 1993).

4.2 Bipolar Outflow

Two linear structures, best seen in the interferometer maps in Figure 2.2 but also detected at the CSO, extend radially away from V1331 Cygni. Blueshifted CO (1→0) and CO (2→1) emission is present to the northwest of the star between velocities of -8.7 km s^{-1} and -0.75 km s^{-1}. Redshifted gas is also evident to the southwest but is not fully mapped here; previous CO (2→1) studies (Levreault 1985) with larger spatial coverage delineate the flow structure more completely. Together these two components form a bipolar outflow with its axis between PA 140° and 230°. The low optical extinction (A_v=2.4) towards V1331 Cygni suggests the star lies on the near side of its parent molecular cloud (Anglada *et al.* 1989). The blueshifted outflow may be weak as it has broken out of the cloud, while its redshifted counterpart propagates into the cloud, sweeping up comparatively more mass and facilitating detection. This suggests that V1331 Cygni is viewed more along its outflow axis than in the plane of the sky.

4.3 Ring Emission

We detect a gaseous ring around V1331 Cygni 4.1 $\times$ 10^4 by 2.8 $\times$ 10^4 AU in size, with a maximum velocity dispersion of $\sim$20 km s^{-1}. Conservative estimates suggest a ring mass of at least 0.07 $M_\odot$ and possibly up to 0.54 $M_\odot$. At these distances and velocities, it is unlikely that the emission is from infalling

material. The observed emission pattern (Figures 2.2, 2.3(a) and (b)) cannot arise from rotating gas, as the angular momentum would be large and the implied velocity gradient of $\sim$120 km s^{-1} pc^{-1} would be much larger than typical cloud core values of $\sim$10 km s^{-1} pc^{-1} (Goldsmith & Arquilla 1985; Myers 1985). We believe the emission arises from outflowing material. However, the observed spatial dependence of emission with velocity cannot be produced by a bipolar outflow or a uniform expanding spherical shell (see Bachiller & Gomez-Gonzalez 1992 and references therein).

A simple model of an optically thick, radially expanding torus, radius $\sim$1.7 $\times$ 10^4 AU, crudely reproduces the observed distribution of emission. The orientation of the torus, major axis position angle $\sim$40° inclined at 30° to the plane of the sky, was deduced from comparison with the integrated CO (1$\rightarrow$0) ring emission detected by the interferometer. We then determined the radial expansion velocity of the torus by modelling the high velocity resolution CO (2$\rightarrow$1) data obtained at the CSO.

Channel maps of the CO (2$\rightarrow$1) blue arc emission between $-$8.75 and $-$4.75 km s^{-1}, averaged to a velocity resolution of 0.5 km s^{-1}, are shown in contours in Figure 2.7. Emission is concentrated toward PA 130° at high velocities and is more extended at lower velocities. Model results for a torus of vertical extent $\sim$8 $\times$ 10^3 AU and width $\sim$2 $\times$ 10^3 AU, expanding at 22 km s^{-1}, are depicted in greyscale. The model emission is normalized to unity for each channel as detailed radiative transfer calculations were not conducted. The asymmetry of the torus, possible evidence of influence by the surrounding ambient cloud, causes discrepancies between the data and the model fit. We also note that the aspect ratio is poorly constrained by the low spatial resolution. Nevertheless, the model faithfully predicts the trends in emission distribution although it overestimates the extent of the high velocity emission. We therefore suggest that V1331 Cygni is surrounded by a torus, radius $\sim$1.7 $\times$ 10^4 AU, expanding at $\sim$22$\pm$4 km s^{-1}, implying an age of $\sim$4 $\times$ 10^3 years at the current

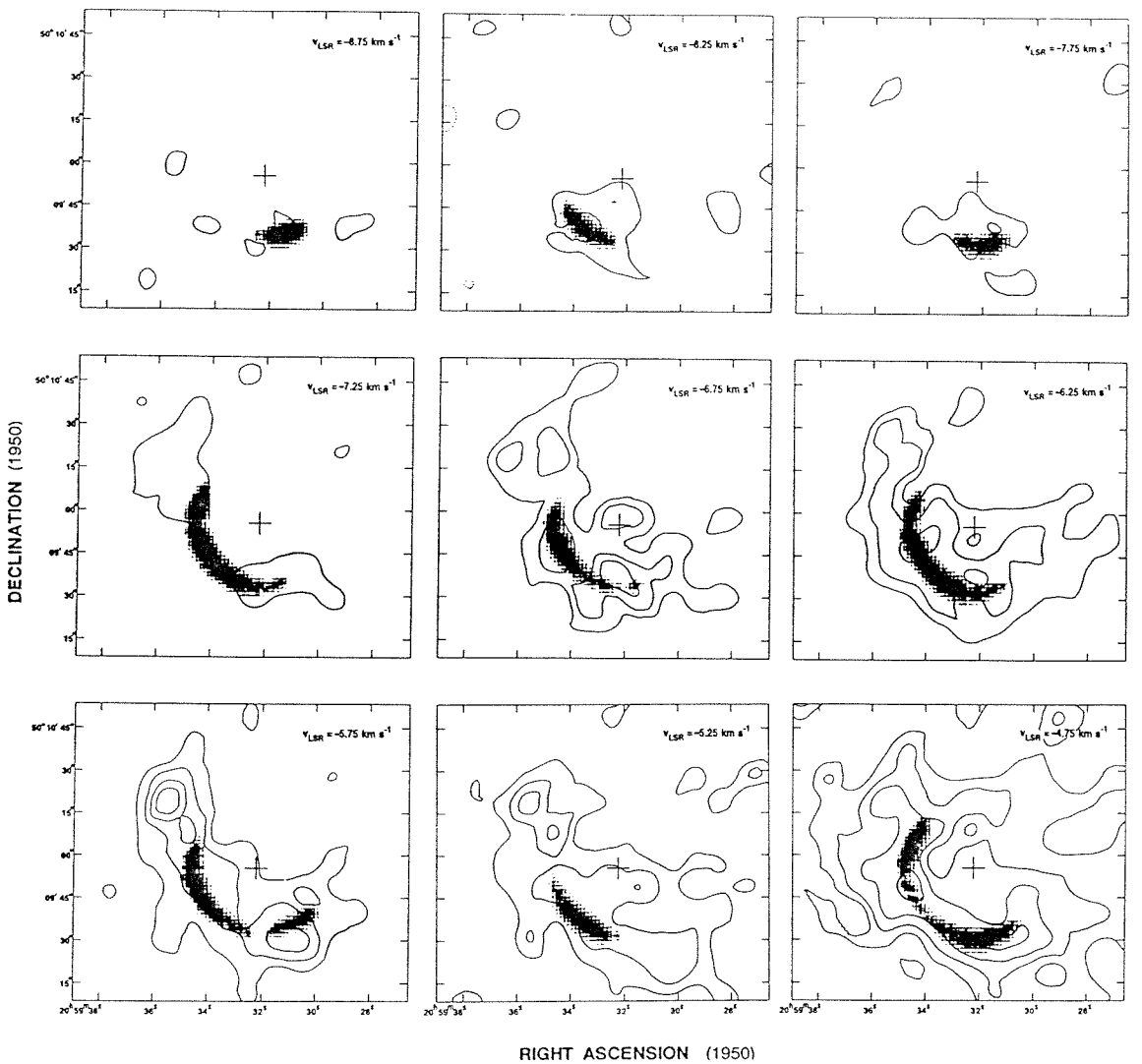

Figure 2.7. Maps of the CO (2→1) emission observed at the CSO between -8.75 and -4.75 km s^{-1}. The mean velocity for each map is shown in the top right corner. Contour levels begin at the 4σ level, 0.8 K, and are separated by 0.4 K (2σ). The optimal model fit torus is depicted in greyscale.

expansion rate.

4.4 Torus Formation Mechanisms

To sweep up the V1331 Cygni torus by radiation pressure requires a stellar luminosity over the torus lifetime of $\geq 10^4$ $L_\odot$, much greater than the present value of ~ 53 $L_\odot$. Theoretical models of rapidly rotating protostars can produce circumstellar rings, but much smaller than the spatial scales here (Williams & Tohline 1988). Therefore the torus is probably wind-driven molecular gas. The torus structure most likely mimics the original gas distribution rather than the wind geometry, for a planar wind though possible is unlikely. As stars form, angular momentum conservation causes accreting material to be concentrated towards the equatorial plane where a more isotropic wind may sweep up gas to form the torus. The torus may therefore be considered as part of an incomplete shell. Indeed, the circular reflection nebulosity may trace the inner edge of an evacuated cavity. The implied torus inclination is $\sim 30°$, suggesting that V1331 Cygni is viewed more pole-on. This is in agreement with the orientation deduced from the bipolar outflow, and with the suggestion that moderately extincted FUors are observed along the system poles (Kenyon & Hartmann 1991).

The torus possesses a momentum between $\sim 1.5 \rightarrow 11.9$ $M_\odot$ km s^{-1}. To sweep up the torus requires a mass loss rate between $1.0 \rightarrow 8.0$ x 10^{-6} $M_\odot$ yr^{-1} over its lifetime, assuming a wind velocity v_{wind}=370 km s^{-1} (Mundt 1984). As the torus in our model only subtends $\sim 0.4\pi$ steradians, the required mass loss rate may be substantially higher for an isotropic wind. The current mass loss rate of $\dot{M} \leq 10^{-6}$ $M_\odot$ yr^{-1} is therefore insufficient to drive the the outflow implying the torus formed at an earlier, more vigorous, stage. Since V1331 Cygni is a FUor pre-outburst candidate, and the FUor phenomenon is possibly repetitive, the torus may have resulted from a previous outburst. For a typical FUor event lasting ~ 100 yrs

(Hartmann 1992), with $\dot{M}\sim10^{-5}$ $M_\odot$ yr^{-1} and v_{wind}=370 km s^{-1} (Croswell *et al.* 1987; Mundt 1984), a total of 0.4 $M_\odot$ km s^{-1} can be entrained by a momentum-conserving stellar wind. For a T Tauri star, V1331 Cygni is moderately massive, lying between the classical T Tauri stars and the Herbig Ae and Be stars in the Hertzsprung-Russell diagram (Chavarria 1981); the distance and A_v adopted here imply $M_{pg}=1^m$, significantly higher than usual for FUors. The outburst may therefore have been even more energetic than average. Clearly, torus formation requires either a single, very vigorous outburst or a series of multiple outbursts; we suggest the torus may be a relic from a younger stage of very energetic activity, possibly when V1331 Cygni was more embedded. The torus expansion time, $\sim4 \times 10^3$ yrs, is thus an upper limit to the time between successive outbursts and is similar to Herbig's (1989) estimate of 5×10^3 yrs.

Such an energetic mass loss stage will have considerable effects on the ambient cloud and possibly serious, although unknown, effects on the circumstellar disk. An isotropic wind would impart $\geq10^{45}$ ergs into the surrounding cloud, comparable to that deposited by bipolar outflows (Beckwith *et al.* 1983), but over a larger angular extent. Although subsequent outbursts may have decreasing effect on the cloud, repeated outbursts may impart $\geq10^{47}$ ergs. This more isotropic form of mass loss suggests FUor outbursts, or their precursors, may considerably change the energy and momentum input to the ambient cloud and that their role has been previously underestimated.

5. Conclusions

The FU Orionis pre-outburst candidate, V1331 Cygni, is surrounded by a massive 0.5±0.15 $M_{\odot}$ circumstellar disk. Surrounding this is a flattened envelope of gas, $\sim 10^4$ AU in diameter, mass ≥ 0.32 $M_{\odot}$ which is in turn surrounded by a nearly circular reflection nebula. At larger scales, we observe both blue and redshifted outflow components of a previously undetected bipolar outflow, whose relative strengths imply V1331 Cygni is viewed more pole-on.

The most striking outflow feature is a large molecular torus surrounding V1331 Cygni, 4.1 by 2.8 $\times$ 10^4 AU in size, mass 0.07–0.54 $M_{\odot}$, expanding at 22±4 km s^{-1} in the system's equatorial plane. The blueshifted component of the torus expands away from the cloud center; it is well defined due to the minimal confusion by emission from foreground gas. The redshifted component that expands into the densest regions, is more massive and more extended. We suggest the torus was swept-up by a roughly isotropic wind ~ 4 $\times$ 10^3 years ago. The outflow energetics require a high mass loss rate, possibly a FUor outburst, which deposited some $\geq 10^{45}$ ergs into the ambient cloud. This may be the first direct observational evidence for the repetitive nature of the FU Orionis phenomenon.

CHAPTER 3

The FU Orionis Binary System RNO 1B/1C

The FU Orionis Binary System RNO 1B/1C

STUART MCMULDROCH, GEOFFREY A. BLAKE
Division of Geological and Planetary Sciences, 170-25
California Institute of Technology
Pasadena, CA 91125
Electronic mail: sxm@sol1.gps.caltech.edu
Electronic mail: gab@csardas.gps.caltech.edu

ANNEILA I. SARGENT
Division of Physics, Mathematics, and Astronomy
California Institute of Technology, 105-24
Pasadena, CA 91125
Electronic mail: afs@mmstar.caltech.edu

To appear in: *The Astronomical Journal*, February 1995

Abstract

Observations of CS (7→6) emission reveal a ~3 $M_\odot$ core, 1.8 × 10^4 AU in size, surrounding the FU Orionis binary system RNO 1B/1C. Fractional chemical abundances, calculated from LVG and LTE codes, are mostly similar to those in the cold core TMC 1. However, values for SiO/H_2 and CH_3OH/H_2 are enhanced, possibly by sputtering reactions or grain-grain collisions in the outflow associated with the young stars.

Aperture synthesis maps of the 2.6 and 3.1 mm continuum emission at ~5″ and ~9″ resolution, respectively, reveal that RNO 1C is surrounded by a flattened, dusty envelope, ~5000 AU in size, with mass ≥1.1 $M_\odot$. High spatial resolution (~3″) interferometer observations of CS (2→1) emission may trace the dense walls of an outflow cavity comprised of two concentric arcs with dynamical ages of 4 × 10^3 and 1 × 10^4 yrs. The velocity structure of lower density gas imaged in the CO (1→0) transition is consistent with the arcs being formed by two energetic FU Orionis outbursts. Each event may have imparted more than 4 $M_\odot$ km s^{-1} to the outflow, implying outburst mass loss rates of ~$10^{-4} M_\odot$ yr^{-1}. It appears that RNO 1C is probably the driving source for the outflow and that while pre-main sequence stars are in the FU Orionis stage, outbursts may dominate both outflow morphology and energetics.

1. Introduction

FU Orionis objects (FUors) may represent a pivotal stage in the evolution of solar mass pre-main sequence stars. They are characterized by a sudden increase in visual brightness of 5-6^m with a much slower decline, and possess distinctive spectral signatures; the Hα and Na I D lines exhibit P Cygni profiles with a suppressed emission component, while absorption line widths and spectral types vary with wavelength and often show a "double-peaked" structure (Herbig 1977, 1989; Hartmann & Kenyon 1987a; Welty *et al.* 1992; Hartmann *et al.* 1993). FUors also display distinctive arcuate reflection nebulae and large infrared excesses (Goodrich 1987). Many of their observed properties have been interpreted in terms of an elevated rate of accretion through a circumstellar disk onto a T Tauri star (Hartmann & Kenyon 1985, 1987a). The number of detected FUor outbursts suggests the phenomenon is repetitive, with stars in the T Tauri stage of evolution undergoing up to 100 outbursts over $\sim 10^6$ yrs (Herbig 1977, 1989; Hartmann 1992). This hypothesis is supported by observations of outflows from young stellar objects (Reipurth 1992; McMuldroch *et al.* 1993).

The main core of the dark cloud L1287, located some 850 pc distant, contains the cometary nebula GN 00.33.9 (Yang *et al.* 1991). Within this nebula lies the proposed binary FUor system, RNO 1B and RNO 1C (Staude & Neckel 1991; Kenyon *et al.* 1993). The binary components are separated by 6″ at PA$\sim$45°. Staude & Neckel (1991) first identified the heavily extincted RNO 1B ($A_v \sim 9^m$) as a FUor and suggested that a nearby bright knot that they designated RNO 1C might contain an even more deeply embedded star. This knot was subsequently identified as a FUor (Kenyon *et al.* 1993). Both objects lie within the positional error bars of IRAS 00338+6312 (L$\sim 680_\odot$) and are associated with water masers (Fiebig *et al.* 1992).

Single dish NH_3 observations reveal a rotating core, $\sim$0.5 $\times$ 0.2 pc in size and elongated along PA 135°, around the FUors (Estalella *et al.* 1993). Maps in the CO (1→0), HCO^+ (1→0), and CO (3→2) transitions indicate that the driving source(s) for an energetic bipolar outflow, oriented at PA$\sim$45° and situated within 30° of the plane of the sky, lie within this core (Snell *et al.* 1990; Yang *et al.* 1991; Evans *et al.* 1994). Infrared polarimetric imaging (Weintraub & Kastner 1993) suggests that the source of the outflow is closer to the nominal position of IRAS 00338+6312 than to RNO 1B or RNO 1C. A VLA map of the 3.6 cm continuum emission also displays a peak within 1″ of the IRAS position and has been interpreted as confirming the presence of a driving source quite distinct from the FUors (Anglada *et al.* 1994).

Although $\sim$7″ resolution aperture synthesis images of CS (2→1) show an intensity maximum near the IRAS position, they lack the sensitivity and spatial resolution to delineate structure reliably (Yang *et al.* 1993). To clarify the detailed structure of the L1287 core, and as part of a larger project to examine FUor characteristics (McMuldroch *et al.* 1993), we have undertaken a program of sensitive high resolution millimeter and submillimeter observations using the Owens Valley millimeter array and the Caltech Submillimeter Observatory, the results of which we describe below.

2. Observations

2.1 CSO Observations

Observations of the core of L1287, encompassing RNO 1B, RNO 1C, and IRAS 00338+6312, were acquired with the Caltech Submillimeter Observatory (CSO) on Mauna Kea, Hawaii, in 1991 July. The facility 230 GHz and 345 GHz SIS heterodyne receivers were used in conjunction with the CSO 500 MHz and 50 MHz bandwidth acousto-optical spectrometers (Ellison & Miller 1987; Ellison *et al.* 1989). Calibration was accomplished by the standard chopper wheel method, while main beam efficiencies were calculated to approximately 20% accuracy from measurements of Jupiter. At 230 GHz and 345 GHz, the beamwidths were 31″ and 21″ (FWHM), with main beam efficiencies of 0.52 and 0.58, respectively. All temperatures quoted in the paper have been corrected for these main beam efficiencies. Position switching to a reference position 10′ west of RNO 1B produced the least contaminated baselines. Pointing was checked regularly on planets and nearby point sources; absolute positions are accurate to within 10″, relative positions within the maps to ∼5″.

Several molecular species were detected towards RNO 1B in the 230 GHz and 345 GHz bands and are listed in Table 3.1. Spectra were acquired for the CO (2→1), $C^{18}O$ (2→1), SiO (5→4), SO ($5_6 \rightarrow 4_5$), HCN (4→3), CH_3OH ($4_2 \rightarrow 3_1$), HCO^+ (4→3), H_2CO ($3_{0,3} \rightarrow 2_{0,2}$), and H_2CO ($3_{2,2} \rightarrow 2_{2,1}$) rotational transitions. In addition, ^{13}CO (2→1) emission at 220 GHz was mapped at half beam spacings over a region ∼45″ × 45″ in size. More extensive maps, 80″ × 80″, also sampled at half beam spacings, were made of the CO (3→2) and CS (7→6) emission. Due to their small Einstein A-coefficients, CO and ^{13}CO trace relatively cold, low density gas while CS, with its higher dipole moment, delineates higher density gas.

2.2 OVRO Observations

Aperture synthesis mapping of the J=1→0 transition of ^{12}CO and the J=2→1

(1) Molecule	(2) Transition	(3) ν (GHz)	(4) Peak T (K)	(5) FWHM (kms^{-1})	(6) Velocity (kms^{-1})	(7) $\int Tdv$ (K kms^{-1})	(8) Wings	(9) N (cm^{-2})	(10) $F_{C^{18}O}$ [1]	(11) F_{CO} [2]	(12) F_{TMC1}
SiO	5→4	217.105	0.3	2.9	-15.7	0.7	?	1(12)	1(-11)	5(-10)	2(-12)
H_2CO	$3_{0,3} \rightarrow 2_{0,2}$	218.222	3.1	4.1	-17.6	14.0	blue	1(14)	1(-9)	5(-8)	2(-8)
CH_3OH	$4_2 \rightarrow 3_1$	218.440	0.71	3.1	-17.4	2.3	?	4(14)	4(-9)	2(-7)	2(-9)
H_2CO	$3_{2,2} \rightarrow 2_{2,1}$	218.475	0.6	3.4	-16.9	2.6	?	2(14)	2(-9)	1(-7)	2(-8)
$C^{18}O$	2→1	219.560	4.96	3.34	-18.3	20.0	no	2(16)	2(-7)	–	2(-7)
SO	$5_6 \rightarrow 4_5$	219.949	1.5	2.7	-17.2	6.0	blue	7(13)	7(-10)	4(-8)	5(-9)
^{13}CO	2→1	220.399	15.9	3.30	-18.6	69.0	blue	1(17)	1(-6)	5(-5)	1(-6)
CO	2→1	230.538	32.9	–	–	–	strong	–	–	–	
CS	7→6	342.883	1.9	3.3	-17.0	8.8	weak	2(14)	2(-9)	1(-7)	1(-8)
CO	3→2	345.796	25.8	–	–	–	strong	–	–	–	
HCN	4→3	354.505	2.5	5.2	-16.4	15.5	yes	1(14)	1(-9)	5(-8)	2(-8)
HCO^+	4→3	356.734	8.8	–	–	–	yes	–	–	–	

Notes to TABLE 1

(1) The fractional abundance relative to H_2 derived using the $C^{18}O$ column density. (2) The fractional abundance relative to H_2 derived using the CO column density.

Table 3.1.

transition of CS at ν = 115.271 and 97.981 GHz, respectively, was carried out using the Owens Valley Radio Observatory (OVRO) millimeter-wave array between 1991 April and 1993 May. Observations at 115.272 GHz employed three 10.4 m diameter telescopes while the 97.981 GHz maps utilized four telescopes. Each telescope was equipped with an SIS receiver, cryogenically cooled to 4 K, producing typical overall system temperatures of 520 K (SSB) at 115 GHz and 320 K (SSB) at 98 GHz.

During the CO observations, two filter banks of 32 $\times$ 1 MHz and 32 $\times$ 50 kHz provided velocity resolutions of 2.6 and 0.13 km s^{-1}. The CS spectral line observations used a digital correlator configured to provide velocity resolutions of 1.53 km s^{-1} and 0.38 km s^{-1}. In both instances, the bandpass was centered on the cloud velocity of -18.3 km s^{-1} (Torrelles *et al.* 1983), while simultaneous continuum observations were obtained in a broadband channel of effective width $\sim$375 MHz.

The phase and amplitude gains were calibrated by observing the quasar 0212+735 at 25 minute intervals, and the absolute flux scale was established from measurements of Neptune and Uranus. Maps were generated from calibrated visibility data using the NRAO AIPS software package. Positional accuracy is $\pm$ 2″. Maximum unprojected baselines of 140 m north-south and 200 m east-west gave a uniform weighted synthesized beam of 3″.8 $\times$ 2″.7, PA 90°, at 98 GHz and a naturally weighted beam of 7″.8 $\times$ 4″.8, PA 85°, at 115 GHz. For these beams, T_B = 1 K corresponds to 0.41 Jy/beam and 0.08 Jy/beam. The phase center of the maps is α (1950) = $00^h\ 33^m\ 52.11^s$, δ (1950) = +63° 12′ 24″.0, the position of RNO 1B (Staude & Neckel 1991).

3. Results

3.1 CSO Results and Analysis

Table 3.1lists the line parameters and integrated fluxes of molecular species observed toward RNO 1B/1C with the CSO. Dashes indicate where spectra are seriously affected by self-absorption or outflow. The presence of wing emission is indicated in column 8, where a question mark indicates too low a signal-to-noise ratio to detect outflow signatures. The velocity of peak flux is indicated in column 6; molecules with low critical densities, such as CO and its isotopes, peak at about -18.3 km s^{-1}, while species with higher critical densities have maxima between -17.6 and -15.7 km s^{-1}. Where collisional cross sections were available, column densities and fractional abundances were calculated using an LVG code. Otherwise an LTE code in the optically thin regime was employed.

3.1.1 The Cloud Core

Contours in Figure 3.1show the CS (7→6) emission integrated over the velocity range -24 to -12 km s^{-1}. Contours begin at 20% of the peak flux of 13 K km s^{-1} and are separated by 10%. Emission is marginally resolved in the 21″ beam. The peak is displaced ∼4″ southwest of the IRAS position and ∼12″ northwest of RNO 1C. As the spectrum inset in Figure 3.1shows, the line peaks at a velocity of -17.0 km s^{-1}. Excitation of the CS (7→6) transition requires densities in excess of 10^6 cm^{-3}, so that the observations trace a high density core surrounding the FUors displaced from the bulk cloud velocity of -18.3 km s^{-1} by 1.3 km s^{-1}. We therefore adopt -17.0 km s^{-1} as the systemic velocity of the core containing the FUors.

The spectra of most species, apart from the CO isotopes, also peak near -17.0 km s^{-1}, implying an origin within the CS core. Calculations utilizing an LVG code and the ratio of the H_2CO line pair indicate a kinetic temperature, T_{kin}, of 30-40 K. At these temperatures, the ratio is only weakly dependent on density, making

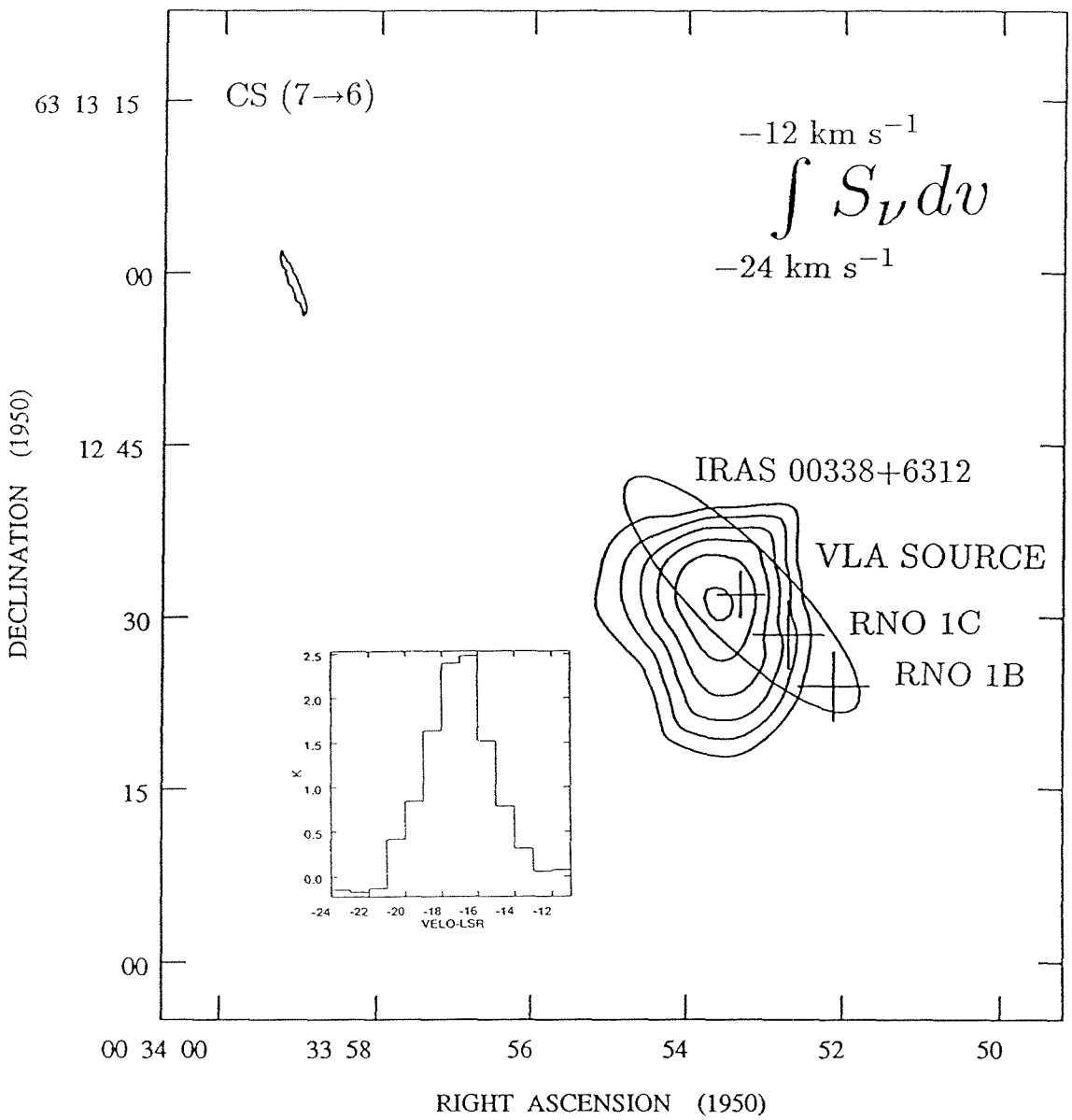

Figure 3.1. A map of the CS (7→6) emission integrated between V_{LSR}=−24 and −12 km s^{-1}. Contours begin at 8 K and are separated by 1 K. The inset shows the CS spectrum in the region of peak emission. A cross, 4″ in size, marks the position of the VLA source, while an ellipse indicates the range of positional uncertainty for IRAS 00338+6312. Crosses 6″ in size mark the positions of RNO 1B and RNO 1C.

this a particularly useful temperature diagnostic (*cf* Jansen *et al.* 1993; van Dishoeck *et al.* 1993; Mangum & Wootten 1993). LTE calculations yield similar values, 30-50 K. Columns 10 and 11 in Table 3.1list the range of fractional abundances for each molecular species, determined by dividing species column density by the molecular hydrogen column density of the cloud and of the outflow respectively. In column 10, lower limits are derived by dividing species column density by the molecular hydrogen column density estimated from $C^{18}O$ measurements assuming a canonical abundance $C^{18}O/H_2=2 \times 10^{-7}$ ((Chackerian & Tipping 1983); these trace the total mass in the core and surrounding cloud. In column 11, upper limits are derived by dividing species column density by the molecular hydrogen column density estimated from the CO (3→2) wing column density of 2×10^{17} cm^{-2}, using $^{12}CO/H_2=10^{-4}$ (Chackerian & Tipping 1983) and assuming that emission originates entirely from outflowing gas. For comparison, column 12 lists fractional abundances for the cold core TMC 1 (van Dishoeck *et al.* 1993 and references therein). In calculating the core mass, we adopt a CS abundance ratio $CS/H_2 = 1 \times 10^{-8}$ (Irvine *et al.* 1987). This is typical of dense cores and intermediate between our two derived extremes. For T_{kin}=35 K, we calculate a core column density of 2.0×10^{22} cm^{-2} in the optically thin limit, leading to a core mass, M_{core}, of 2.6 $M_\odot$.

Figure 3.2 displays the ^{12}CO, ^{13}CO, and $C^{18}O$ (2→1) spectra at the position of RNO 1B. The CO (and HCO^+) spectrum shows a self-absorption minimum centered at -17.0 km s^{-1}, suggesting absorption is associated with a lower excitation cocoon surrounding the core seen in the CS (7→6) map. This feature is not observed in lower spatial resolution CO spectra (Yang *et al.* 1991), consistent with a localized absorbing layer.

3.1.2 Cloud Characteristics

Due to their low critical densities, $n_{crit} \sim 10^3$ cm^{-3}, emission from the J=2→1

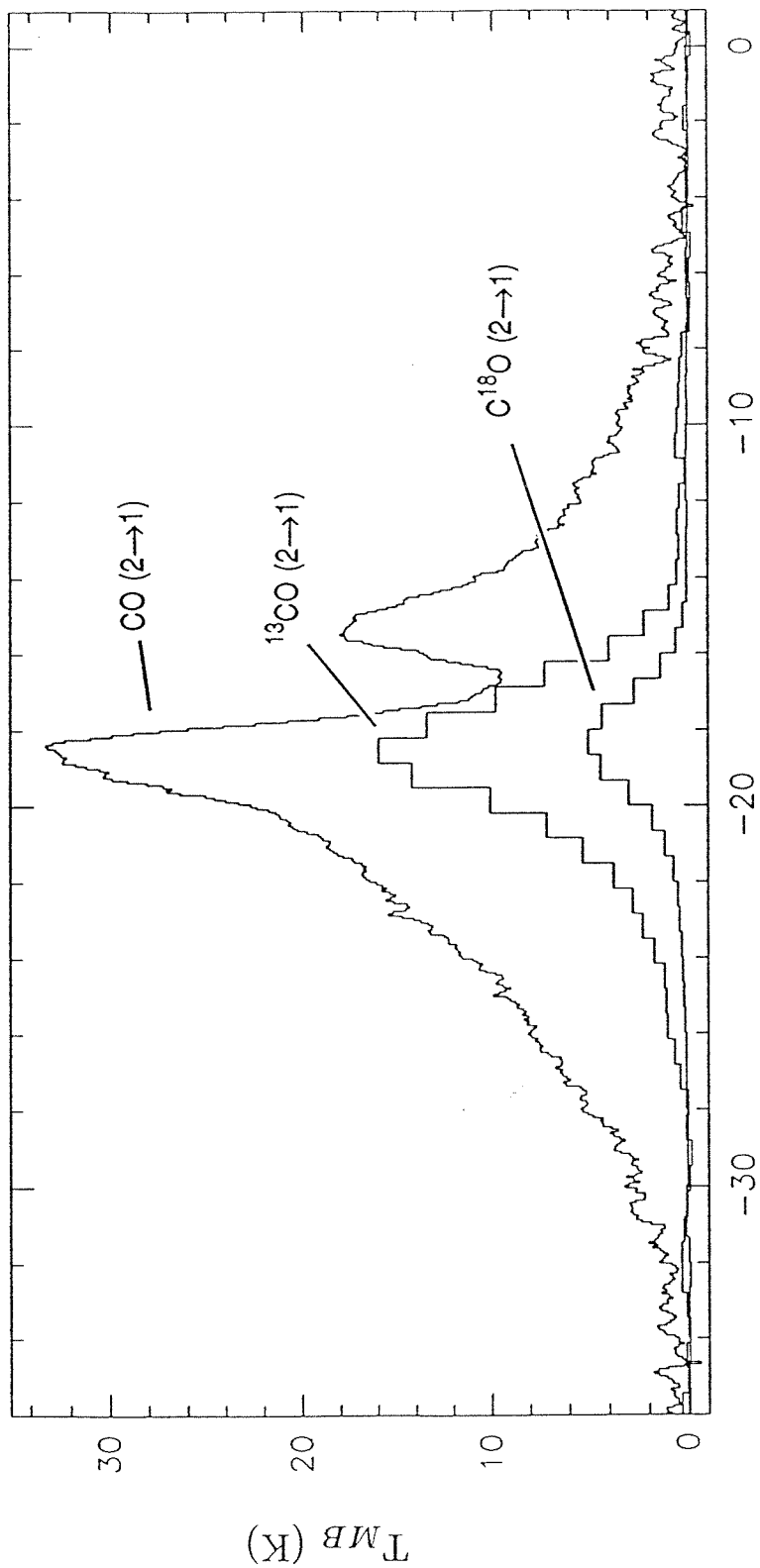

Figure 3.2. Line emission in CO, ^{13}CO, and C^{18}O (2→1) as detected at the CSO. Temperatures have been corrected for main beam efficiencies.

transition of ^{13}CO and $C^{18}O$ molecules probably traces the ambient, larger-scale cloud structure. In both species, the spectra peak near -18.3 km s^{-1}. Line widths are about 2.7 km s^{-1} away from RNO 1B/1C, increasing to 3.4 km s^{-1} in the direction of the FUors. From the ratio of $^{13}CO/C^{18}O$ peak brightness temperatures, we estimate the $C^{18}O$ optical depth, $\tau_{C^{18}O}$, is 0.4. LVG calculations, using the $C^{18}O$ line parameters 42″ away from the core center, yield a cloud column density of 5×10^{22} cm^{-2}, assuming a standard abundance ratio of $C^{18}O/H_2 = 2 \times 10^{-7}$ (Chackerian & Tipping 1983).

3.1.3 Outflow Characteristics

In Figure 3.2, the strong wing emission in ^{12}CO is not evident in $C^{18}O$, while ^{13}CO exhibits only a weak blueshifted wing. Comparison of CO and $C^{18}O$ spectra suggests inner velocity boundaries to the outflow wings of -20 km s^{-1} and -15 km s^{-1}, excluding velocities affected by self-absorption, and similar to estimates based on CO (3→2) measurements at 21″ resolution (Evans *et al.* 1994). To investigate the outflow further, we mapped the CO (3→2) line at 10″ spacings over the region where wings were clearly evident. Emission was detected only between -37 km s^{-1} and -3 km s^{-1} to a 3σ limit of 0.9 K. Self-absorption is clearly evident between -19.5 km s^{-1} and -15 km s^{-1}. In Figure 3.3, broken contours depict the blueshifted CO (3→2) component integrated over the velocity range -37 to -20 km s^{-1}. Solid contours delineate the weaker redshifted emission integrated between -15 and -3km s^{-1}. Taken together, the blue and redshifted CO (3→2) emission regions trace a bipolar outflow extending ∼90″ tip-to-tip along PA ∼45°. The morphology is similar to that observed in CO (1→0) maps (Snell *et al.* 1990; Yang *et al.* 1991) and in the less completely sampled CO (3→2) observations of Evans *et al.* (1994). The positions of IRAS 00338+6312, RNO 1C, and RNO 1B are located between the redshifted and blueshifted emission peaks implying, as expected, that

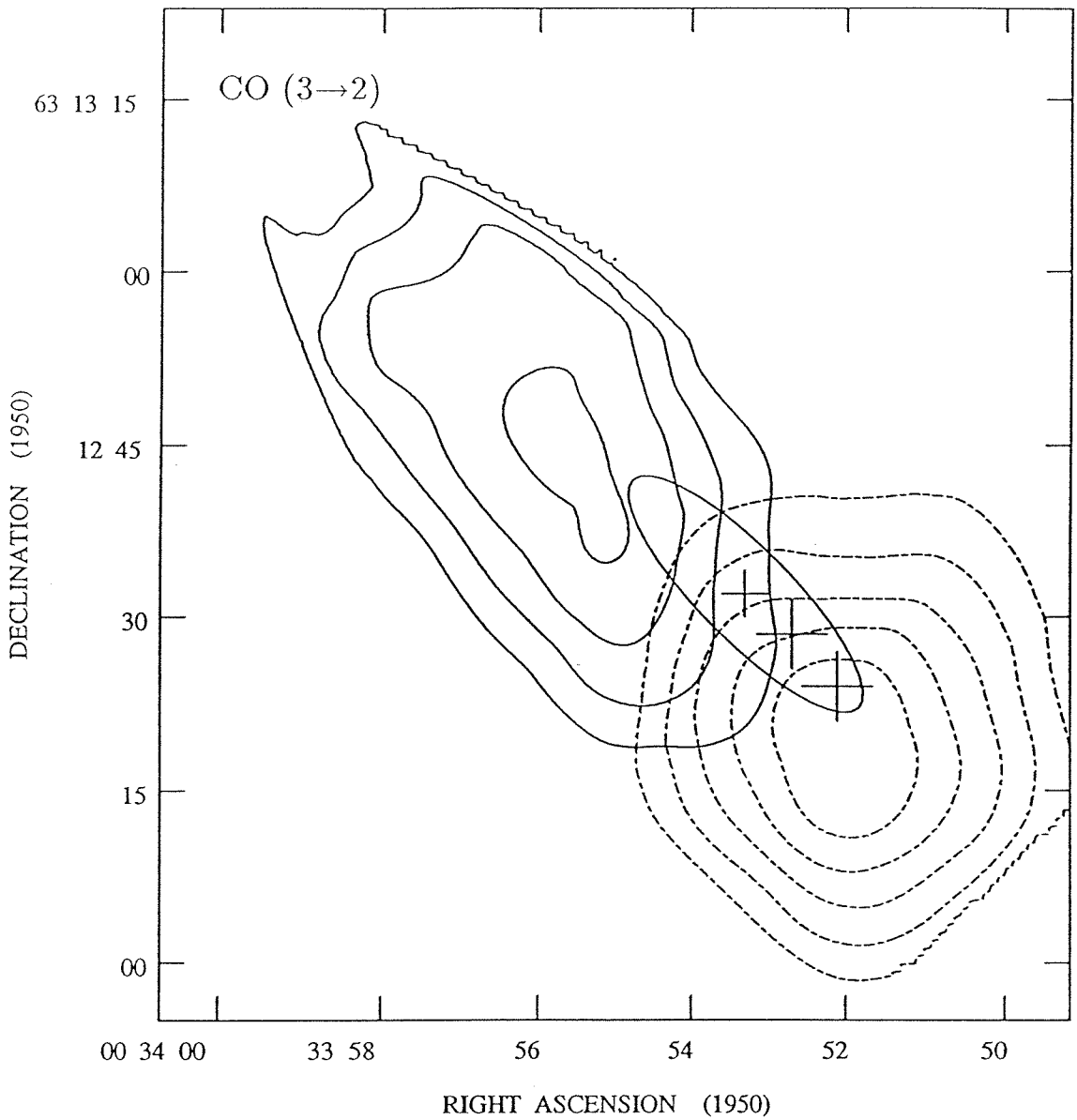

Figure 3.3. A map of the CO (3→2) emission observed at the CSO. Broken contours depict the blueshifted emission, peak 149 K km s^{-1}, integrated between velocities of −37 and −20 km s^{-1}. Solid contours depict the redshifted emission, peak 114 K km s^{-1}, integrated between velocities −15 and −3 km s^{-1}. In both cases, contours begin at 50 K km s^{-1} and are spaced by 20 K km s^{-1}.

one of them is the driving source of the outflow.

Following Scoville *et al.* 1986, we calculate the mass in each outflow lobe from the equations:

$$\int N(CO)\ d\Omega = 4.75\ \times\ 10^{12}\ \frac{(T_x + 0.93)}{e^{-22.34/T_x}}\ \frac{\tau_{CO}}{(1 - e^{-\tau_{CO}})} \int\int T_{MB}\ dv d\Omega \qquad (1)$$

and

$$M = 4.04\ \times\ 10^{9}\ \frac{\mu\ m_{H_2}\ (D_{kpc})^2\ \int\ N(CO)\ d\Omega}{X(CO)} \qquad M_{\odot} \qquad (2)$$

Here, $\int\int\ T_{MB}\ dv d\Omega$ is the integrated line intensity summed over the solid angle dΩ for which emission is apparent, and has values of 2.1 $\times$ 10^{-6} and 3.6 $\times$ 10^{-6} K km s^{-1} sr^{-1} for the blue and red wings respectively. T_x is the excitation temperature; τ is the optical depth; μ is the mean molecular weight; m_{H_2} is the mass of molecular hydrogen; D is the source distance in kiloparsecs, and X(CO) is the CO abundance relative to hydrogen. We adopt X(CO)=10^{-4} (Chackerian & Tipping 1983) and an average excitation temperature of 15 K, the typical kinetic temperature in the outflow. A 5 K temperature difference corresponds to an approximately 20% change in mass. Optical depths of 9.2 and 3.1 for the blue and red wings are calculated from the CO/^{13}CO (3$\rightarrow$2) brightness ratio (Evans *et al.* 1994), with resulting masses of 1.4 and 0.5 $M_{\odot}$. Using flux weighted average outflow velocities of -6.5 and $+3.5$ km s^{-1} relative to the systemic velocity, we estimate the momenta in the blue and red lobes to be 9.1 and 1.8 $M_{\odot}$ km s^{-1}.

3.2 Owens Valley Results and Analysis

3.2.1 Continuum Emission in the Core

Figures 3.4(a) and (b) show maps of the 2.6 and 3.1 mm continuum flux in the vicinity of RNO 1B/1C. Extended flux is at low signal to noise levels at 3.1 mm

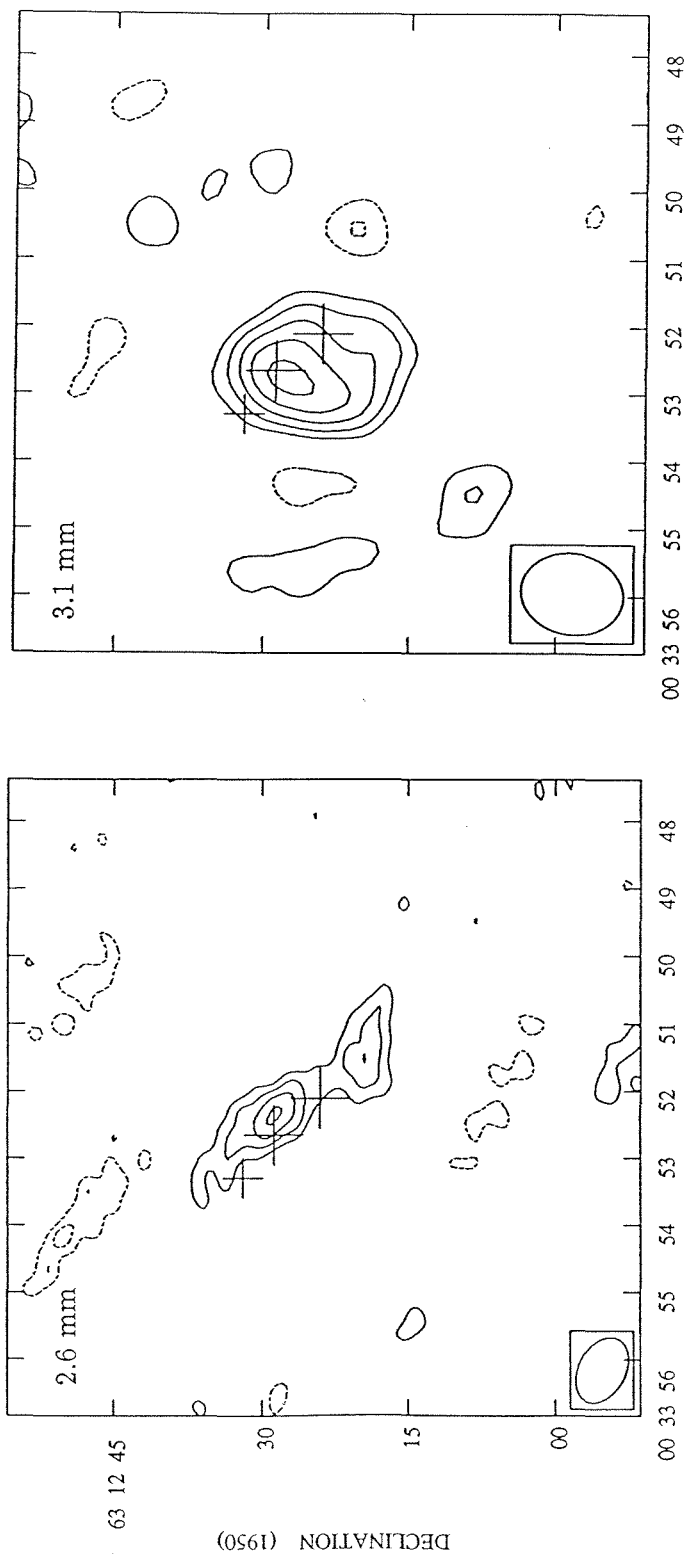

Figure 3.4. Aperture synthesis maps of the 2.6 and 3.1 mm continuum emission observed toward RNO 1B/1C. Contours begin at the 2σ levels (11 mJy/beam at 2.6 mm and 9 mJy/beam at 3.1 mm) and are thereafter separated by 1σ. An ellipse in the lower left corner denotes the size of the synthesised beam in all OVRO maps. In this and all subsequent maps, the error ellipse of the IRAS source position is omitted to minimize confusion.

and contaminated by sidelobes at 2.6 mm. Morphological differences between the two maps are strongly affected by the beam pattern since emission in the central core is only marginally resolved in each case, with a 7″.0 × 4″.0 (PA 37°) beam at 2.6 mm and a 10″.4 × 8″.2 (PA −8°) beam at 3.1 mm. Within the positional errors of ±2″, both the 2.6 mm peak of 26 mJy/beam and the 3.1 mm peak of 29 mJy/beam coincide with RNO 1C. This strongly suggests that emission from RNO 1C dominates the emission pattern. High resolution maps of millimeter continuum emission are probably the most reliable way of identifying embedded thermal sources (*cf* Sargent & Welch 1994).

VLA observations at λ=3.6 and 6 cm revealed a source near the IRAS position with spectral index 1.5, typical of ionized gas (McCutcheon *et al.* 1991; Anglada *et al.* 1994). Extrapolation indicates that such free-free processes contribute less than 6 mJy at λ=3.1 mm. Our aperture synthesis maps therefore trace thermal dust emission. The concentration of dust towards RNO 1C suggests that this source is possibly the primary driver of the outflow.

Following Hildebrand (1983), the mass of molecular gas associated with RNO 1C can be calculated from the 2.6 and 3.1 mm flux densities of 60±30 mJy and 45±20 mJy, respectively, using:

$$M_{H_2} = \frac{0.120\ F_{Jy}\ (D_{kpc})^2\ (\lambda_{mm})^3\ (e^{14.4/\lambda_{mm}\ T_d}\ -\ 1)}{\kappa_\nu} \qquad M_\odot, \qquad (3)$$

where F_{Jy} is the observed continuum flux density in Janskys, λ_{mm} is the observing wavelength in millimeters, T_d is the dust temperature, and κ_ν is the mass opacity coefficient for the dust grains at frequency ν. We assume a characteristic dust temperature of 50 K, slightly larger than our value for the core kinetic temperature of 35 K. Estimates of κ_ν can vary by over an order of magnitude. Here we adopt

$$\kappa_\nu = \kappa_0 \left(\frac{0.25\text{mm}}{\lambda_{mm}} \right)^\beta , \quad (4)$$

with $\kappa_0 = 0.1$ cm^2 gr^{-1} (Hildebrand 1983) and $\beta \sim 1$ (*cf* Beckwith & Sargent 1991). Resulting masses are 1.1±0.6 and 1.4±0.6 $M_\odot$ at 2.6 and 3.1 mm. This value of κ_ν is conservatively high, giving lower limits to the mass surrounding RNO 1C. Upper limits to the mass, using the same coefficients, at the positions of RNO 1B and the VLA source are 0.3 and 0.4 $M_\odot$, at 2.6 and 3.1 mm respectively.

3.2.2 CO (1→0) Maps

Figures 3.5 (a)-(d) show aperture synthesis CO (1→0) line maps of the RNO 1C region at ∼5″ resolution in the velocity ranges −44.2 to −31.2 km s^{-1}, −31.2 to −23.4 km s^{-1}, −23.4 to −18.2 km s^{-1}, and −15.6 to −5.2 km s^{-1}. No flux was detected outside these velocity ranges to a 3σ limit of 240 mJy/beam. At the highest blueshifted velocities, Figure 3.5 (a), the peak flux is centered between RNO 1C and RNO 1B; at smaller blueshifted velocities, Figures 3.5 (b) and (c), emission extends away from the stars to the southwest. At low redshifted velocities seen in Figure 3.5 (d), emission peaks to the northeast of RNO 1C. Taken together, these features form the blue and redshifted components of the bipolar outflow. In our CSO CO (3→2) maps, the blueshifted lobe also extends to the southwest and the redshifted lobe to the northeast, so that highly blueshifted CO (1→0) emission is expected southwest of the driving source, reaffirming the central role of RNO 1C. Indeed, as shown in Figure 3.5 (c), emission near the core velocity peaks within the positional uncertainties at RNO 1C. Strong extended emission lies along PA 115°, approximately perpendicular to the outflow. It is unclear from the present data if this is a disk-like structure or part of the outflow.

The total integrated fluxes for each of the regions depicted in Figures 3.5 (a)-(d) are 15, 233, 401, and 339 Jy km s^{-1} respectively. Following Scoville *et al.* (1986),

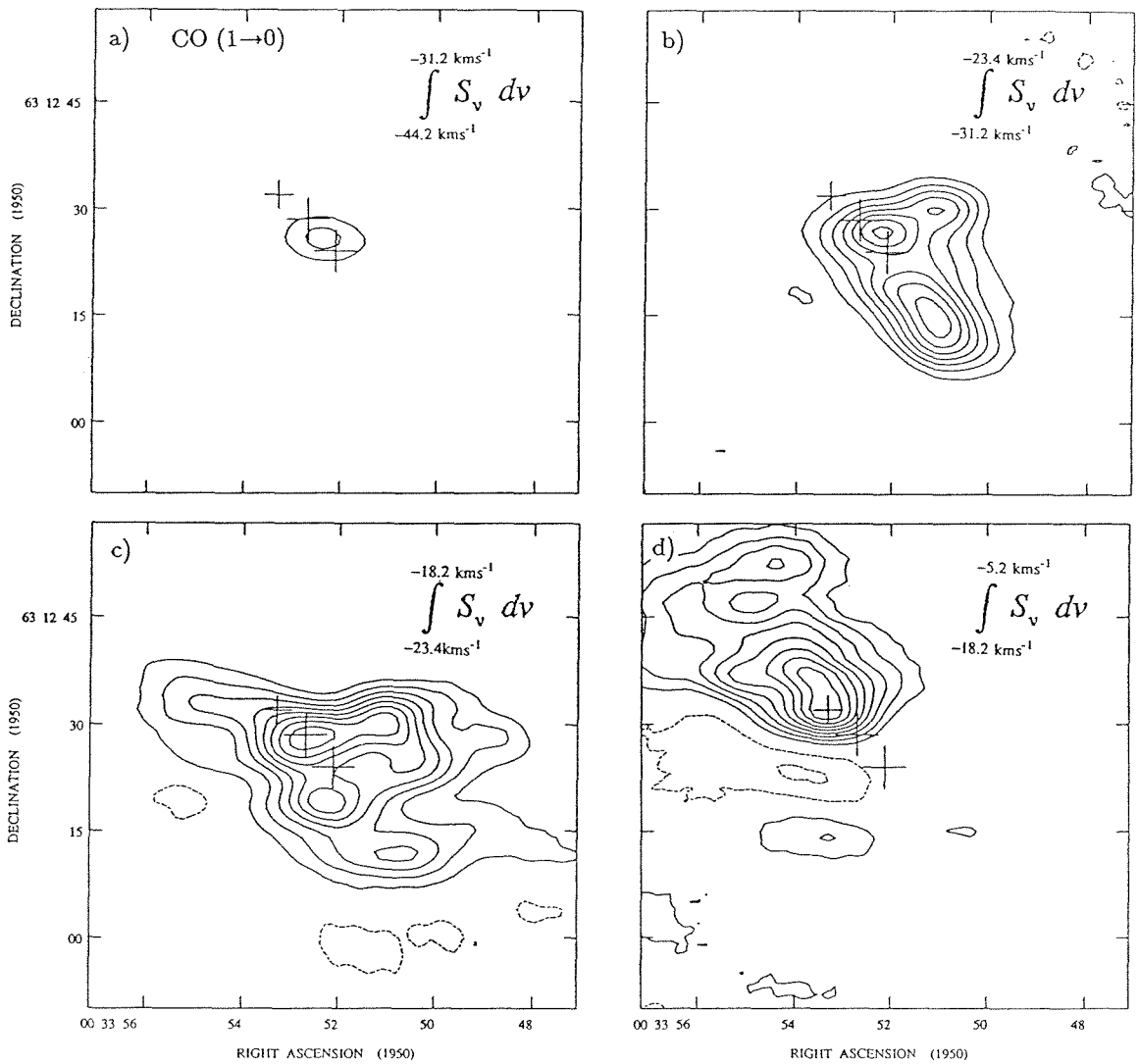

Figure 3.5. Owens Valley array maps of the CO (1→0) emission integrated over the velocity ranges −44.2 to −31.2 km s^{-1}, −31.2 to −23.4 km s^{-1}, −23.4 to −18.2 km s^{-1}, and −18.2 to −5.2 km s^{-1}. Contours begin at and are separated by 0.5 Jy/beam km s^{-1}.

the mass of H_2 implied in each case is given by:

$$M = 2.19 \times 10^{-9} \frac{(T_x + 0.93)}{e^{-5.53/T_x}} \frac{\tau_{CO}}{(1 - e^{-\tau_{CO}})} \frac{D_{kpc}^2}{X(CO)} \int S_\nu \, dv \qquad M_\odot, \quad (5)$$

where $\int S_\nu$ dv is the integrated flux density in units Jy km s^{-1} and the remaining parameters are as described for Equation 3.1. As before, we adopt an excitation temperature for the outflow of 15 K and assume the emission is optically thin. We calculate minimum masses for the regions depicted in Figures 3.5 (a)-(d) of 5×10^{-3}, 0.08, 0.15, and 0.12 $M_\odot$ and associated momenta of 0.12, 0.85, 0.55, and 0.67 $M_\odot$ km s^{-1} respectively.

3.2.3 CS (2→1) Emission

Emission from the CS (2→1) rotational transition was detected only between velocities of −30.6 km s^{-1} and −10.6 km s^{-1} to a 3σ limit of 26 mJy/beam. No high velocity gas corresponding to the CO (1→0) emission seen in Figure 3.5 (a) was observed. The contour and greyscale aperture synthesis maps of Figures 3.6 (a)-(c) show the CS integrated intensity at ∼3″ resolution over the velocity ranges −30.6 to −22.9 km s^{-1}, −22.9 to −16.8 km s^{-1}, and −16.8 to −10.6 km s^{-1}. Figure 3.6 (d) shows the total integrated CS (2→1) emission. The CS (2→1) emission peak is not coincident with the CS (7→6) maximum (Figure 3.1) probably due to the lower resolution and greater positional uncertainties of the CSO data.

At the highest observed blueshifted velocities, Figure 3.6 (a), emission peaks ∼18″ southwest of RNO 1C with a low intensity region extending back toward the star. The morphology is roughly analogous to that in the CO (1→0) map of Figure 3.5 (b). We infer the CS structure represents a denser component of the blueshifted outflow. In Figure 3.6 (b), a possible double arcuate structure lies to the southwest of the FUors; the more prominent arc is located about 25″ from RNO 1C while a possible

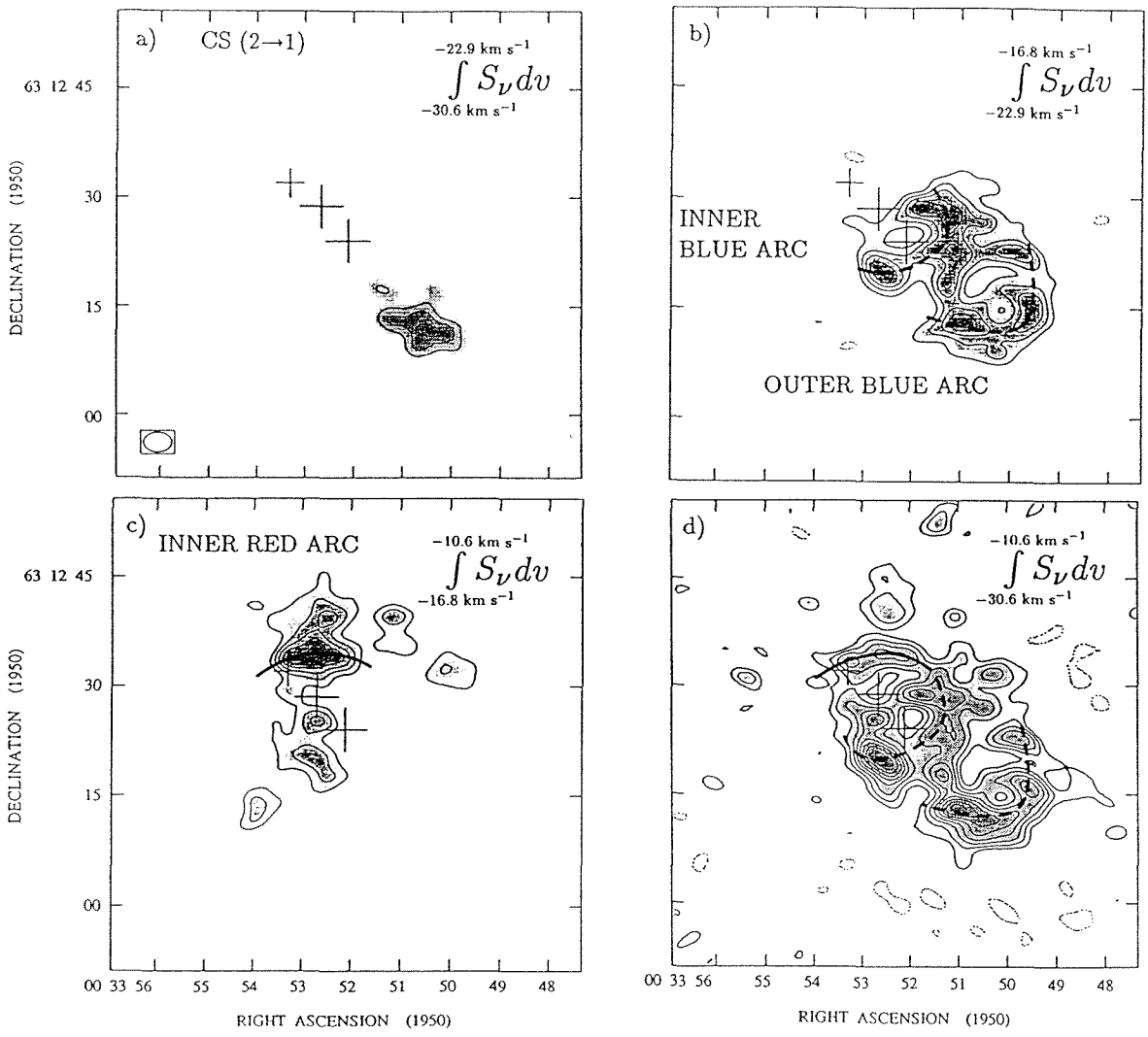

Figure 3.6. Aperture synthesis maps of the CS (2→1) emission integrated over velocities −30.6 to −22.9 km s^{-1}, −22.9 to −16.8 km s^{-1}, −16.8 to −10.6 km s^{-1}, and −30.6 to −10.6 km s^{-1} respectively. Contours in each map begin at 20% of the peak total integrated flux, 3.42 Jy/beam km s^{-1}, and are separated by 10%. The greyscale image depicts the same emission for clarification. Heavy broken lines trace the blueshifted arcs described in the text while a solid line follows the redshifted arc.

inner arc lies within 10″. Redshifted emission shown in Figure 3.6 (c) peaks ∼5″ north of RNO 1C and may be the redshifted counterpart of the inner arc seen in Figure 3.6 (b). Overall, the redshifted emission is less prominent than the blueshifted component. Indeed, our CSO observations demonstrate that the red outflow has a lower peak intensity and is slightly more extended so that it may be resolved out. Within 1 km s^{-1} of the systemic velocity, −17 km s^{-1}, emission also appears resolved out or possibly self-absorbed.

Maps presented in Figure 3.7 illustrate the behavior of blueshifted CS emission between −22.32 and −18.11 km s^{-1} at a velocity resolution of 0.38 km s^{-1}. There is a condensation 25″ southwest of RNO 1C at the highest velocities. Approaching the systemic velocity, −17 km s^{-1}, this bifurcates forming a loop. Emission is also present ∼10″ to the south and west of RNO 1C and forms a possible inner arc between velocities of −21.55 and −20.02 km s^{-1}. At distances of ∼10-25″ (8.5-21.2 × 10^3 AU) from RNO 1C the observed velocity displacements are not consistent with rotation or infall. We suggest emission arises from outflowing gas. Between −19.64 and −18.49 km s^{-1}, the morphology is dominated by a dumbbell structure oriented perpendicularly to the outflow. For these velocities which are closer to the systemic value, it is difficult to ascertain whether emission arises from rotation, infall, or outflow.

The mass of swept up gas can again be calculated (*cf* Scoville *et al.* 1986; Ohashi *et al.* 1991) using

$$M = 1.3 \times 10^{-11} \frac{(T_x + 0.4)}{e^{-7.1/T_x}} \frac{\tau_{CS}}{(1 - e^{-\tau_{CS}})} \frac{D_{kpc}^2}{X(CS)} \int S_\nu \, dv \qquad M_\odot, \qquad (6)$$

where we use the same parameters as in for Equation 3.5 but with a CS abundance ratio, X(CS), of 1 × 10^{-8} (Irvine *et al.* 1987). Assuming optically thin emission, we calculate masses of 0.24, 1.20, and 0.94 $M_\odot$ for the structures observed in each of the

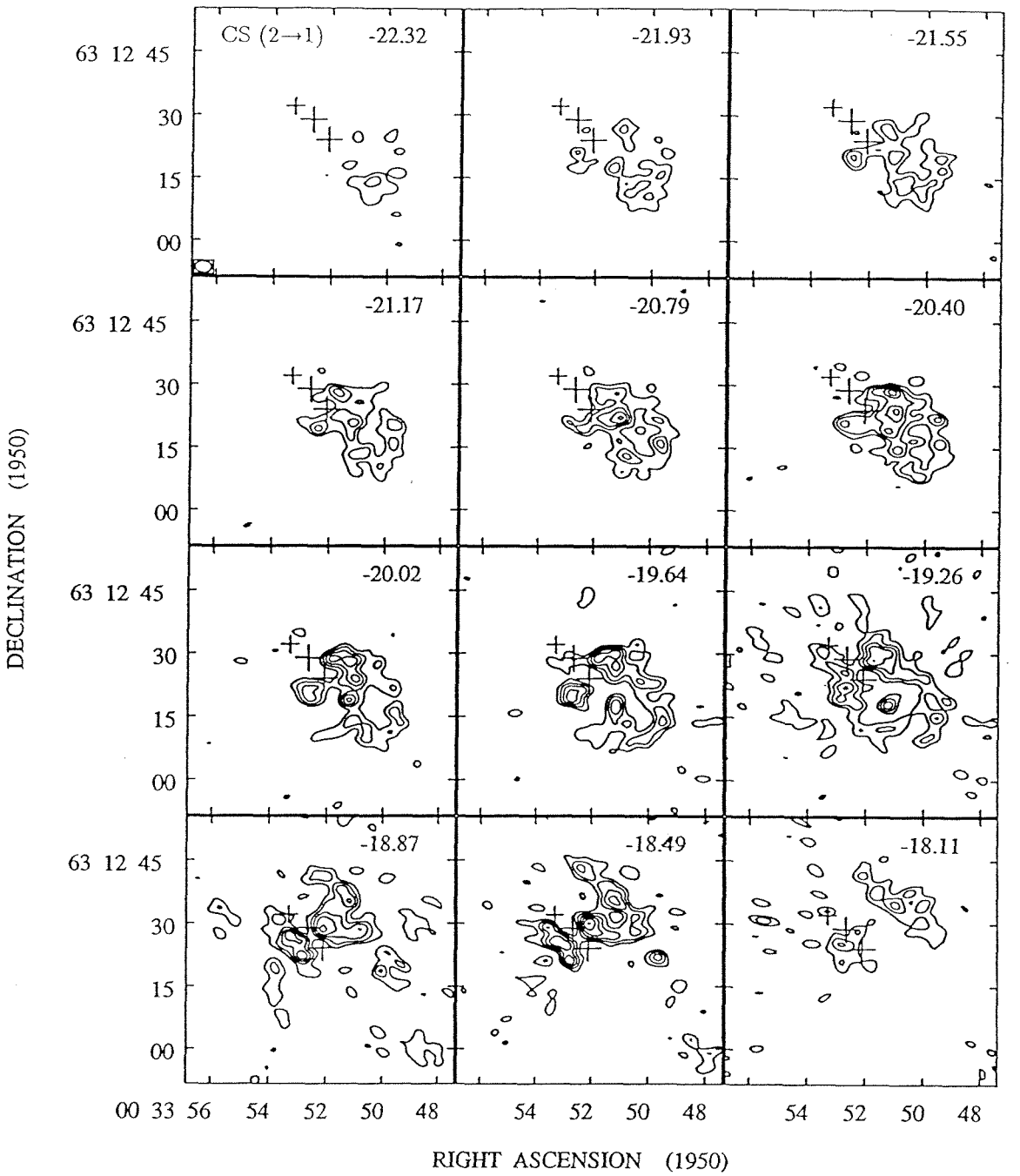

Figure 3.7. High velocity resolution maps of the blueshifted CS (2→1) emission observed toward RNO 1B/1C over the velocity range −22.32 to −18.11 km s^{-1}. The velocity of each channel is indicated in the upper right corner. Contours begin at the 3σ level, 270 mJy/beam, and are thereafter separated by 2σ.

velocity ranges of Figures 3.6 (a)-(c). Estimated masses and momenta for the outer and inner "arcs" are 0.58 and 0.52 $M_{\odot}$, and 2.20 and 2.08 $M_{\odot}$ km s^{-1}.

4. Discussion

4.1 Chemistry

Our CSO maps demonstrate that the FU Orionis binary system, RNO 1B/1C, is surrounded by a dense core, 1.8 $\times$ 10^4 AU in size, of mass $\sim$3 $M_\odot$. Although the core is only weakly offset from the bulk cloud velocity, outflowing gas is kinematically quite distinct from the ambient cloud material. Mass estimates of the quiescent and outflowing components are provided by the $C^{18}O$ and ^{12}CO J=2$\rightarrow$1 lines, from which we derive the fractional abundances limits presented in Table 3.1. For comparison, this table also presents the abundances found in the TMC 1 dark cloud.

The abundances of most molecules, especially those not obviously associated with the outflow, are comparable to those in molecular cloud cores devoid of star formation. Certain species, notably CS, H_2CO, and SO are weakly enhanced in the outflowing gas; by contrast CH_3OH and SiO show enhancements larger than an order of magnitude. While the small enrichments may result from density and temperature enhancements caused by the outflow, the enhancements of SiO and CH_3OH are likely the result of chemical interactions.

Moderate enhancements in SiO and CH_3OH are not unusual in regions of outflow activity (*cf* Bachiller & Gomez-Gonzalez 1992; van Dishoeck *et al.* 1993), where low velocity shocks can drive new reaction routes even for low luminosity sources. The refractory SiO molecule is most likely produced by sputtering or evaporation of dust grains in regions of directly shocked and entrained material. Alternatively, SiH_4 may sublime from grain surfaces to react with OH to form SiO. The high observed abundances of CH_3OH towards RNO 1B/1C cannot be produced either by low temperature ion-molecule or gas phase shock chemistry (Sandell *et al.* 1994). However, grain mantle evaporation can provide the needed methanol (Blake *et al.* 1991); the increased velocity dispersion surrounding bipolar outflows may

result in shorter grain-grain collision times at relatively low collision velocities thereby increasing grain mantle evaporation rates without shattering the grains themselves (Blake *et al.* 1994). These two distinct processes of grain sputtering as opposed to softer grain-grain collisions should have different spatial distributions. However, higher spatial resolution observations are required to investigate the RNO 1B/1C morphology further.

4.2 The Driving Source of the Outflow

Aperture synthesis maps of the continuum emission at 2.6 and 3.1 mm shown in Figures 3.4 (a) & (b), suggest a lower limit of 1.1 $M_{\odot}$ for the mass around RNO 1C. Reprocessed radiation from the dust may account for the sharp rise in the RNO 1B/1C spectral energy distribution beyond 12 μm (Kenyon *et al.* 1993). For a source ~5000 - 7000 AU in size, a spherical dust distribution produces a visual extinction $A_v \geq 50^m$ (Spitzer 1978), much larger than the observed value of $A_v \sim 12^m$ (Staude & Neckel 1991). It seems likely that the dust is asymmetrically distributed, but the large size precludes a truly centrifugally supported circumstellar accretion disk. Since continuum emission appears marginally resolved at different beam sizes, we suggest that the material surrounding RNO 1C follows a power law density distribution (Ladd *et al.* 1991; Terebey *et al.* 1993).

The location of RNO 1C at the peak of millimeter continuum emission, its central position between the peaks of the blue and redshifted outflow lobes (Figures 3.5 (a)-(d)), and its association with the CS (2→1) dumbbell structure (Figure 3.7), together indicate that the FUor is the driving source for the outflow in L1287. Infrared polarization measurements and centimeter continuum emission suggest a third more embedded source near the IRAS position is possibly the driving source ((McCutcheon *et al.* 1991; Weintraub & Kastner 1993; Anglada *et al.* 1994). However, the millimeter continuum peak is located ~8″ from the IRAS position, virtually excluding it as

the outflow source, since millimeter continuum measurements are probably the most accurate determinant of the position of an embedded object. We suggest that the infrared observations are sensitive to the dust geometry surrounding RNO 1C and are therefore affected by the outflow cavity structure. Moreover, the radio continuum spectral index of 1.5 is characteristic of free-free emission regions frequently observed at moderate distances from energetic, outflow sources (McMullin *et al.* 1994). The error in the IRAS position encompasses both RNO 1B and RNO 1C. It is difficult to reconcile the spatial coincidence of the IRAS source, the centimeter emission peak, and pattern of polarization with our new observations.

4.3 Outflow Structure

High spatial resolution (3″.8 × 2″.7, PA 90°) maps of the CS (2→1) emission reveal the high density structure of the L1287 outflow in Figures 3.6 (a)-(d) and 3.7. We do not detect the axisymmetric offset in the outflow noted by Yang *et al.* (1993) and interpreted as evidence of helical structure. Overall, the emission pattern resembles a limb-brightened outflow cavity lying nearly in the plane of the sky. The morphology is consistent with CS emission tracing the cavity walls that have been compressed by the outflow wind and with the higher velocity CO emission tracing entrained low-density gas.

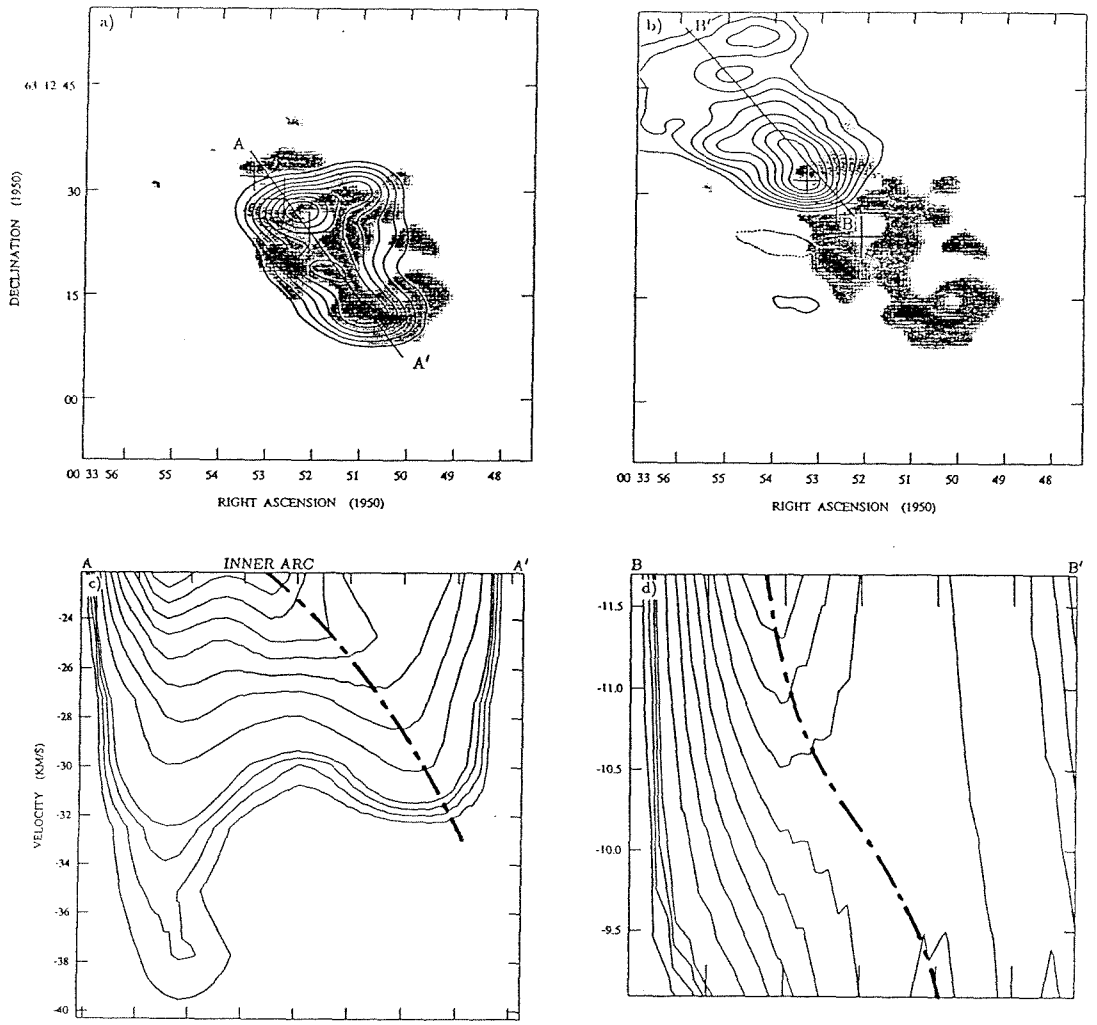

Figure 3.8. Aperture synthesis maps of CO (1→0) and CS (2→1) emission towards RNO 1B/1C. Contours in (a) depict the blueshifted CO emission integrated over velocities −44.2 to −20.8 km s^{-1} while contours in (b) depict the redshifted CO emission integrated between −15.6 and −5.2 km s^{-1}. Contours start at 20% and are separated by 10% of the peak flux in each velocity interval. In both cases, the greyscale shows the total integrated CS emission. Figures (c) and (d) are the position-velocity diagrams of emission along AA' and BB" respectively. Contours are at 4%, 6%, 8%, 10%, 20%, 30%, 40%, 50%, 60%, 70%, 80%, and 90% of the peak flux in each diagram. Heavy dashed lines trace the approximately linear velocity trends discussed in the text.

In Figure 3.8 (a), contours of the blueshifted CO (1→0) emission integrated between velocities −44.2 to −20.8 km s^{-1} are shown, while in Figure 3.8 (b), contours trace the redshifted CO emission integrated between −15.6 and −5.2 km s^{-1}. In both figures, a greyscale image shows the total integrated CS (2→1) emission which we believe traces the outflow cavity. The maximum blueshifted CO intensity occurs southwest of RNO 1C and extends to the southwest. Secondary peaks occur at the positions of the inner and outer arcs described in Section 3.2.3. By contrast, redshifted CO peaks at the position of the northern inner arc and extends to the northeast. Figures 3.8 (c) and 3.8 (d) are position-velocity (PV) cuts through the blue and red lobes along lines AA′ and BB′ respectively. It is clear from Figure 3.8 (c), that gas over a wide velocity range contributes to the emission around RNO 1C. Across the southern inner arc, emission appears at velocities between $\sim$ −22 and −32 km s^{-1}. Between the arcs, peak velocity linearly increases with distance from the source as marked by a dashed line. A similar although much weaker trend is apparent for the redshifted emission in Figure 3.8 (d).

Although outflow models predict the existence of cavities (Masson & Chernin 1993; Raga & Cabrit 1993; Chernin *et al.* 1994), few have been confirmed (Uchida *et al.* 1987; Moriarty-Schieven *et al.* 1987; Avery *et al.* 1990; Meyers-Rice & Lada 1991). There is some suggestion that cavities around FUors may be more common (Moriarty-Schieven *et al.* 1987; McMuldroch *et al.* 1993). In terms of time-scales and velocities characteristic of outflows, a FUor event is explosive and instantaneous. The inner and outer arcs traced in CS (2→1) may be interpreted as dense gas swept up by two separate FUor outbursts. Material is driven at all velocities by an outburst, which becomes velocity sorted with increasing distance from the source, leading to the PV structures seen in Figures 3.8(a) and (b). Gas swept up by the more recent outburst lies close to the source at all velocities, while velocity-sorting of the gas swept up

earlier has produced the observed linear position-velocity relationship. Alternatively, the observed velocity pattern can be interpreted in terms of time-dependent collimated jet outflow models (Raga & Biro 1993; Raga & Cabrit 1993), in which internal working surfaces propagate along a collimated jet entraining gas in the wake of a bowshock. These models produce cavity morphologies comparable to those presented here and also yield radial velocities that increase away from the source. However, these models are for outflows with a time-dependent wind velocity rather than mass loss rate as is the case for FUors.

The momenta of the cavity's inner and outer arcs, estimated from measurements of CS (2→1) emission, are 2.0 and 2.1 $M_\odot$ km s^{-1} respectively, while the momenta of the CO (1→0) outflow lobes are 1.6 and 1.0 $M_\odot$ km s^{-1}. A classical FUor outburst lasting 100 years, with a wind velocity of 500 km s^{-1} and a mass loss rate of 10^{-4} $M_\odot$ yr^{-1}, imparts only ~0.5 $M_\odot$ km s^{-1} of momentum. This suggests that if the arcs were formed by FUor activity then the outbursts were exceptionally energetic entraining ~4 $M_\odot$ km s^{-1}. The present luminosity of L_{bol} ~1000 $L_\odot$ for RNO 1B/1C suggests the current outburst is also exceptionally energetic, assuming wind energy scales with accretion luminosity (Cabrit & Bertout 1992).

Single dish CO (3→2) observations yield an outflow lifetime of ~10^4 years. The velocity dispersions seen in Figures 3.8(c) and (d) suggest a repetition timescale of 4 × 10^3 yrs, while dynamical age estimates of the arcs, made from CS observations assuming an inclination angle i=30°, yield lower bounds of 4 × 10^3 and 1 × 10^4 yrs. A maximum of three outbursts could have occurred in the lifetime of the outflow yielding ~12 $M_\odot$ km s^{-1} of momentum, approximately the total outflow momentum of 11 $M_\odot$ km s^{-1} (see Section 3.3). If the arcs are indeed caused by FUor activity, then FUor outbursts possibly dominate both outflow morphology and outflow energetics in this source.

5. Conclusions

We have carried out sensitive high resolution millimeter and submillimeter observations of the FU Orionis binary system RNO 1B/1C. CS (7→6) measurements trace a dense core, 1.8 × 10^4 AU in size, mass ~3 $M_\odot$, at V_{LSR}=−17.0 km s^{-1}. Fractional chemical abundances in this core, calculated from LVG and LTE codes, are largely similar to those in the cold core TMC 1. Enhancements in the SiO and CH_3OH abundances are consistent with a low velocity shock liberating grain mantle material to the gas phase. Indeed, observations of the CO (3→2) emission delineate a bipolar outflow, oriented at PA 45°, with blueshifted emission lying to the southwest of RNO 1B/1C.

Aperture synthesis observations of 2.6 and 3.1 mm continuum emission from the RNO 1B/1C core at 7″.0 × 4″.6 (PA 62°) and 10″.4 × 8″.2 (PA −8°) resolution lead us to conclude that RNO 1C is surrounded by a flattened dusty envelope, ~5000 AU in size, with a minimum mass of 1.1 $M_\odot$ The morphology of the CO (1→0) aperture synthesis images also suggests RNO 1C is possibly the driving source. A dumbbell structure oriented at 90° to the outflow axis and 3″ southwest of RNO 1C is visible in CS (2→1) images and further strengthens this interpretation.

The CS (2→1) interferometer maps are consistent with the presence of an outflow cavity lying nearly in the plane of the sky. Two concentric arcs, 9 × 10^3 and 21 × 10^3 AU from RNO 1C, are apparent in blueshifted emission, although only the inner arc has a redshifted counterpart. The gas velocity structure is consistent with formation by two energetic FU Orionis outbursts, 4 × 10^3 and 1 × 10^4 yrs ago. The time between outbursts, ~5 × 10^3 yrs, is comparable to previous estimates of 2 × 10^3 yrs based on source frequency statistics. Each outburst may have imparted more than 4 $M_\odot$ km s^{-1} to the outflow, implying a mass loss rate of $\dot{M}$~10^{-4} $M_\odot$ yr^{-1} for a 500 km s^{-1} wind lasting 100 yrs. It appears that while young pre-main sequence

stars are in the FU Orionis stage, outbursts may possibly dominate both outflow morphology and energetics.

CHAPTER 4

The FU Orionis Object V1057 Cygni

The FU Orionis Object V1057 Cygni

STUART MCMULDROCH
Division of Geological and Planetary Sciences, 170-25
California Institute of Technology
Pasadena, CA 91125
Electronic mail: sxm@sol1.gps.caltech.edu

ANNEILA I. SARGENT
Division of Physics, Mathematics, and Astronomy
California Institute of Technology, 105-24
Pasadena, CA 91125
Electronic mail: afs@mmstar.caltech.edu

GEOFFREY A. BLAKE
Division of Geological and Planetary Sciences, 170-25
California Institute of Technology
Pasadena, CA 91125
Electronic mail: gab@csardas.gps.caltech.edu

To be submitted to: *The Astronomical Journal*

Abstract

High resolution aperture synthesis maps of the CO (1→0), ^{13}CO (1→0), ^{13}CO (2→1) and associated continuum emission from the FU Orionis object V1057 Cygni trace an unresolved 0.09 $M_\odot$ dusty envelope surrounded by a extended molecular gas envelope, some 7500 × 4700 AU in size, of mass ≥0.2 $M_\odot$. Further from the star, maps trace a bipolar outflow oriented at PA 150° of mass ∼3.2 $M_\odot$, age 9.4 × 10^4 years. Envelope kinematics suggest that gas maybe infalling with $\dot{M}_{env}$ ≥1.5 × 10^{-5} $M_\odot$ yr^{-1}. This infall rate cannot sustain the current FU Orionis outburst. If the FU Orionis phenomenon is repetitive, the average time interval between outbursts of V1057 Cygni is ∼600 years, much shorter than previous estimates. Higher spatial resolution observations are needed to confirm this result.

1. Introduction

The pre-main sequence star V1057 Cygni is located 700 pc distant on the southern edge of the North American Nebula, NGC 7000 (Chavarria-K 1981). In 1970, the star increased in visual brightness by 6^m over approximately one year and has subsequently dimmed by $\sim 2^m$ (Welin 1971; Herbig 1977). V1057 Cygni possesses a reflection nebula and spectrum characteristic of an FU Orionis object (FUor); the Balmer lines exhibit P Cygni profiles with a suppressed emission component, while absorption line widths and spectral type vary with wavelength and show a "double-peaked" structure (Herbig 1977, 1989; Goodrich 1987; Welty *et al.* 1992). Spectra prior to the outburst are consistent with those of a strong-lined T Tauri star (Herbig 1958). Many of the observed outburst properties of V1057 Cygni have been interpreted in terms of an elevated rate of accretion through a circumstellar disk onto the central star (Kenyon *et al.* 1988; Welty *et al.* 1992; Hartmann *et al.* 1993). The frequency of FUors suggests the phenomenon is repetitive, with stars in the T Tauri stage of evolution undergoing up to 100 outbursts over $\sim 10^6$ yrs (Herbig 1977, 1989; Hartmann 1992).

Models of infrared emission from V1057 Cygni suggest it is surrounded by a flattened infalling envelope viewed less than 30° from pole-on (Kenyon & Hartmann 1991). Low values of vsini, and variable circular polarization, are also consistent with a nearly pole-on geometry (Wolstencroft & Simon 1975). Models of the continuum spectral energy distribution yield an envelope mass of $\sim 0.1\ M_\odot$ (Weintraub *et al.* 1991). Optical emission is linearly polarized at PA 68° suggesting that the envelope maybe aligned along this direction (Bastien 1982; Whitney & Hartmann 1993).

Low resolution CO (1→0) maps possibly trace a ring at V_{LSR}=+4.2 km s^{-1}, radius 2′, centered on V1057 Cygni (Bechis & Lo 1975). The ring is not seen in ^{13}CO (1→0) emission which traces density variations and the curvature of the

reflection nebulosity (Bechis & Lo 1975). Maps of the CO emission wings reveal a blueshifted outflow lobe to the north (Levreault 1985). Radio emission at centimeter wavelengths, probably from free-free processes, suggests 10% of the driving wind from the FUor is ionized (Rodríguez *et al.* 1990; Rodríguez & Hartmann 1992). Transient H_2O and OH maser emission most likely arises in the vigorous outflow (Lo & Bechis 1973, 1974; Anderson *et al.* 1979; Winnberg *et al.* 1981; Rodríguez *et al.* 1987). As part of a larger project to examine FUor characteristics, we have undertaken a program of sensitive high resolution millimeter and submillimeter observations of V1057 Cygni using the Owens Valley millimeter array and the Caltech Submillimeter Observatory.

2. Observations

2.1 CSO Observations

Observations of V1057 Cygni were acquired with the Caltech Submillimeter Observatory (CSO) on Mauna Kea, Hawaii, in 1991 June, 1992 August, and 1993 June. The facility 230 GHz and 345 GHz receivers were used in conjunction with the CSO 500 and 50 MHz bandwidth acousto-optical spectrometers (Ellison & Miller 1987; Ellison *et al.* 1989). Position switching to a reference position at α=20^h 59^m 56^s, $\delta = +44°\ 03'\ 46''.42$ produced the least contaminated spectra. All temperatures quoted in the paper have been corrected for the main beam efficiencies of 0.52 and 0.58 at 230 and 345 GHz, respectively. Further details of the observational techniques are given by McMuldroch *et al.* (1993).

Although several molecular species in the 230 GHz band were searched for towards V1057 Cygni, only the J=2→1 transitions of CO and its isotopes were detected above a 3σ rms noise limit of 0.5 K. Extended CO (2→1) emission was also mapped on a $6' \times 6'$ grid, sampled every $10''$, centered on V1057 Cygni. In the 345 GHz band, spectra were obtained of the CO (3→2) line towards the FUor.

2.2 OVRO Observations

Aperture synthesis mapping of the rotational transitions of ^{12}CO (1→0), ^{13}CO (1→0), and ^{13}CO (2→1) at ν=115.271, 110.201, and 220.399 GHz respectively, was carried out using the Owens Valley millimeter-wave interferometer between 1990 October and 1991 June. At 110.201 GHz and 220.399 GHz, maximum unprojected baselines of 140 m north-south and 200 m east-west gave naturally weighted synthesized beams of $4''.4 \times 4''.1$ at PA $-30°$ and $3''.6 \times 2''.3$ at PA $-25°$. At 115.271 GHz, maximum baselines of 100 m north-south and 100 m east-west resulted in a naturally weighted beam of $5''.9 \times 5''.2$ at PA $-5°$. For these beams, T_B = 1 K corresponds to 0.18 Jy/beam, 0.32 Jy/beam and 0.33 Jy/beam respectively.

The phase center of the maps is α=20^h 57^m 06.6^s, δ = +44° 03′ 46″.42. Positional accuracy is ± 2″. Observations were track shared with those of V1331 Cygni, and detailed descriptions of the observational technique are given in McMuldroch *et al.* (1993).

3. Results

3.1 CSO Results and Analysis

Emission from V1057 Cygni was detected in four molecular transitions at the CSO, namely CO (3→2), CO (2→1), ^{13}CO (2→1), and C^{18}O (2→1). Spectra, corrected for main beam efficiencies, are displayed in Figure 4.1. The CO (2→1) peak brightness temperature, T_{MB} ~7.8 K, occurs at 4.9±0.3 km s^{-1}, with wing emission extending to −6 and +10 km s^{-1}. The CO (3→2) spectrum is similar, albeit weaker, with peak T_{MB}=5.9 K at 4.6±0.21 km s^{-1}. By contrast, the ^{13}CO (2→1) spectrum, with peak T_{MB}=5.3 K at 3.6±0.3 km s^{-1}, displays no redshifted and only weak blueshifted wing emission. The C^{18}O (2→1) profile, with a peak brightness temperature of T_{MB}=1.5 K at a velocity of 3.8±0.3 km s^{-1}, contains only a very weak blueshifted wing component. The full width at half maximum velocities for ^{13}CO and C^{18}O are 2.2 and 2.1 km s^{-1} respectively.

Relative line intensities suggest that CO and possibly ^{13}CO emission is optically thick at line center, but that C^{18}O (2→1) is optically thin, with $\tau_{C^{18}O}$ ~0.3. We suggest that C^{18}O best traces the kinematics of the gas towards V1057 Cygni, and therefore adopt 3.8 km s^{-1} as the systemic velocity. Comparison of CO and C^{18}O spectra suggests inner boundaries to the wings of +2 and +5 km s^{-1}. Ratios of the CO/^{13}CO line strength indicate an average optical depth τ_{CO} ~20 for the blueshifted CO (2→1) wing emission between −6 and +2 km s^{-1}, with opacity increasing towards lower offset velocities. As the optical depth of the redshifted wing emission between +5 and +10 km s^{-1} is poorly constrained, we adopt τ_{CO} ≤20 for both wings in our calculations.

CO (2→1) emission was mapped at 10″ spacings over a region 360″ × 360″ centered on V1057 Cygni. Figure 4.2 (a) shows in contours and greyscale the CO (2→1) emission integrated over velocities −5.8 to +9.2 km s^{-1}. Gas is

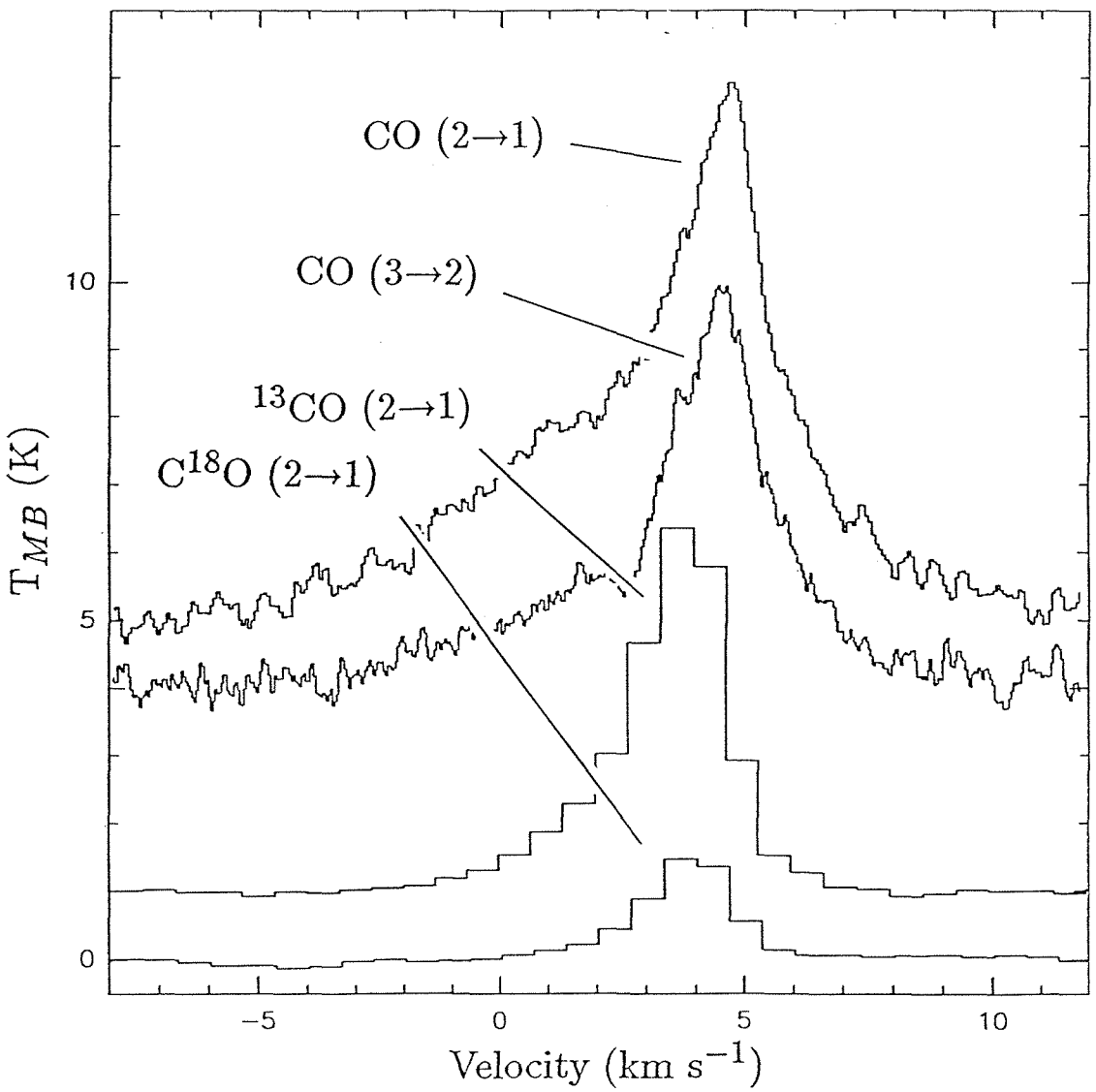

Figure 4.1. Line emission in CO (2→ 1), CO (3→2), ^{13}CO (2→1), and C^{18}O (2→1) as detected at the CSO. Temperatures have been corrected for main beam efficiencies.

Figur

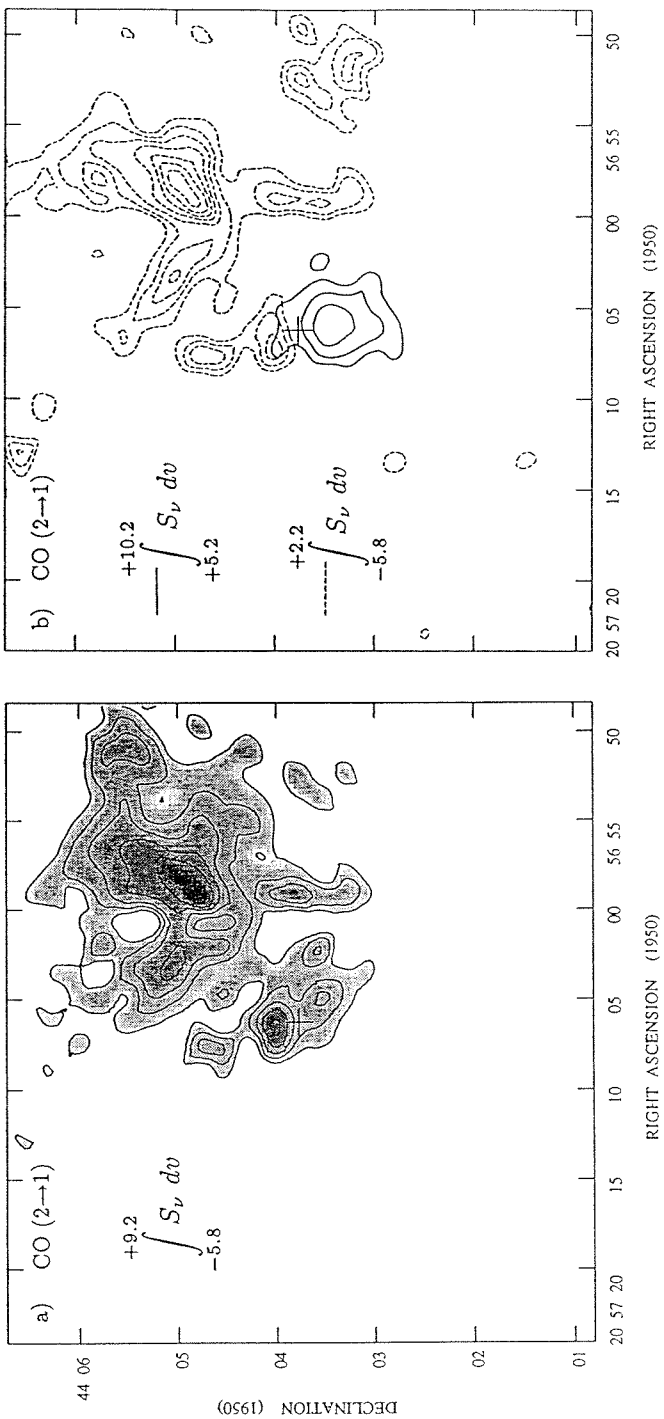

Figure 4.2. Maps of the CO (2→1) emission toward V1057 Cygni. In Figure (a), contours and greyscale trace emission integrated between V_{LSR}=−5.8 and +9.2 km s^{-1}. In Figure (b) solid contours trace redshifted emission integrated between velocities +5.2 and +10.2 km s^{-1} while broken contours show blueshifted emission integrated from −5.8 to +2.2 km s^{-1}. Contours begin at 20 K and are separated by 2 K in Figure (a) while in Figure (b) contours being at 4 K and are separated by 1 K. A cross, 16″ in size, marks the position of V1057 Cygni.

concentrated to the north and west of V1057 Cygni with a peak flux of 31 K km s^{-1} at a distance of 100″, PA−50°. In Figure 4.2 (b), broken contours trace blueshifted emission integrated between −5.8 and +2.2 km s^{-1} while solid contours show redshifted emission integrated from +5.2 to +10.2 km s^{-1}. Within 80″ of the star, blue and redshifted CO (2→1) emission trace the components of a bipolar outflow oriented north-south. Blueshifted emission at larger distances lies between PA∼20° and ∼ −120°. The region of maximum emission extends linearly away from the FUor at PA∼ −45° suggesting an association with the outflow. No evidence is seen of the "ring" structure seen at systemic velocities in CO (1→0) (Bechis & Lo 1975).

Following Scoville *et al.* (1986), we calculate the mass in each outflow lobe from the equations:

$$\int N(CO)\, d\Omega = 1.07 \times 10^{12} \frac{(T_x + 0.93)}{e^{-16.76/T_x}} \frac{\tau_{CO}}{(1 - e^{-\tau_{CO}})} \int\int T_{MB}\, dv d\Omega \qquad (1)$$

and

$$M = 9.1 \times 10^{9} \frac{\mu\, m_{H_2}\, (D_{kpc})^2 \int N(CO)\, d\Omega}{X(CO)} \qquad M_{\odot} \qquad (2)$$

Here, $\int\int T_{MB}\, dv d\Omega$ is the integrated line intensity summed over the solid angle dΩ for which emission is apparent, and has values of 10.6×10^{-6} and 1.4×10^{-6} K km s^{-1} sr^{-1} for the velocity ranges −5.8 to +2.2 km s^{-1} and +5.2 to +10.2 km s^{-1} respectively. T_x is the excitation temperature; τ is the optical depth; μ is the mean molecular weight; m_{H_2} is the mass of molecular hydrogen; D is the source distance in kiloparsecs, and X(CO) is the CO abundance relative to hydrogen. We adopt $X(CO)=10^{-4}$ (Chackerian & Tipping 1983) and an average excitation temperature of 10 K, the typical kinetic temperature in the outflow. Using an optical depth τ_{CO}=20, we calculate masses of 2.8 and 0.36 $M_{\odot}$ for the blue and red lobes

respectively. Associated momenta are 10.2 and 0.7 $M_\odot$ km s^{-1}, adopting flux weighted average outflow velocities of -3.7 and $+2.0$ km s^{-1} relative to the systemic velocity.

3.2 Owens Valley Results and Analysis

3.2.1 Dust and Gas Surrounding V1057 Cygni

Dust continuum emission at 1.3 mm lies 4″ north of V1057 Cygni and is unresolved in the 2.″2 × 2.″0 (1540 × 1400 AU), PA 50°, beam with a peak flux of 55 mJy/beam. This offset is larger than the positional uncertainties but its significance is compromised by the low signal to noise ratio since 1σ=14 mJy/beam. Emission is undetected at 2.7 mm to a 3σ limit of 27 mJy/beam. The mass of associated molecular gas can be calculated from the 1.3 mm flux density following Hildebrand (1983). Assuming a dust temperature of 50 K characteristic of circumstellar material, and adopting an emissivity index $\beta \sim 1$ (*cf* Beckwith & Sargent 1991), we estimate the mass surrounding V1057 Cygni to be 0.09 $M_\odot$.

Figure 4.3 shows in contours the ^{13}CO(1→0) emission integrated over the velocity range +1.55 to +6.95 km s^{-1}. No ^{13}CO (1→0) flux was detected outside these velocities to a 3σ limit of 0.15 Jy/beam. Within the positional uncertainties, the peak of 2.7 Jy/beam km s^{-1} is coincident with V1057 Cygni. Close to the star, emission is extended along PA 42° with a deconvolved size of 7400 × 5200 AU. At greater distances, emission follows the curvature of the reflection nebulosity (Goodrich 1987).

The channel maps in Figure 4.4 show ^{13}CO (1→0) emission over the velocity range +2.84 to +5.28 km s^{-1} at a resolution 0.27 km s^{-1}. For the most redshifted velocities, emission peaks northeast of the FUor. Approaching the systemic velocity of 3.8 km s^{-1}, emission peaks further south. At blueshifted velocities, emission in the stellar vicinity peaks to the southwest while emission at greater distances extends to the northwest. Emission near the star therefore exhibits a northeast-southwest

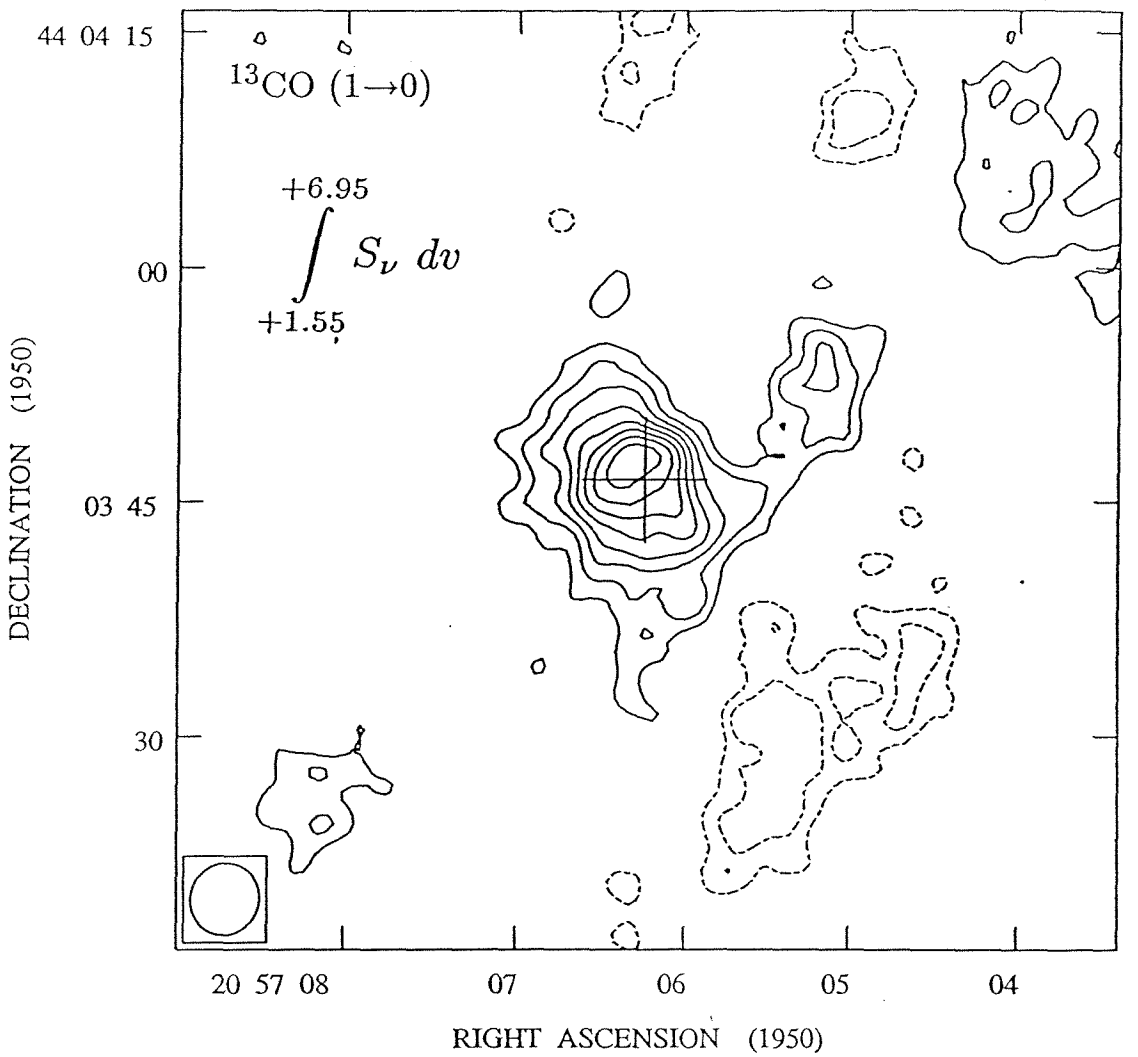

Figure 4.3. Aperture synthesis map of the ^{13}CO (1→0) emission integrated over the velocity range +1.55 to 6.95 km s^{-1}. Contours begin at 20% of the peak flux 2.57 Jy/beam km s^{-1} and are spaced by 10% intervals. In this and all subsequent maps, a cross 8″ in size marks the position of V1057 Cygni.

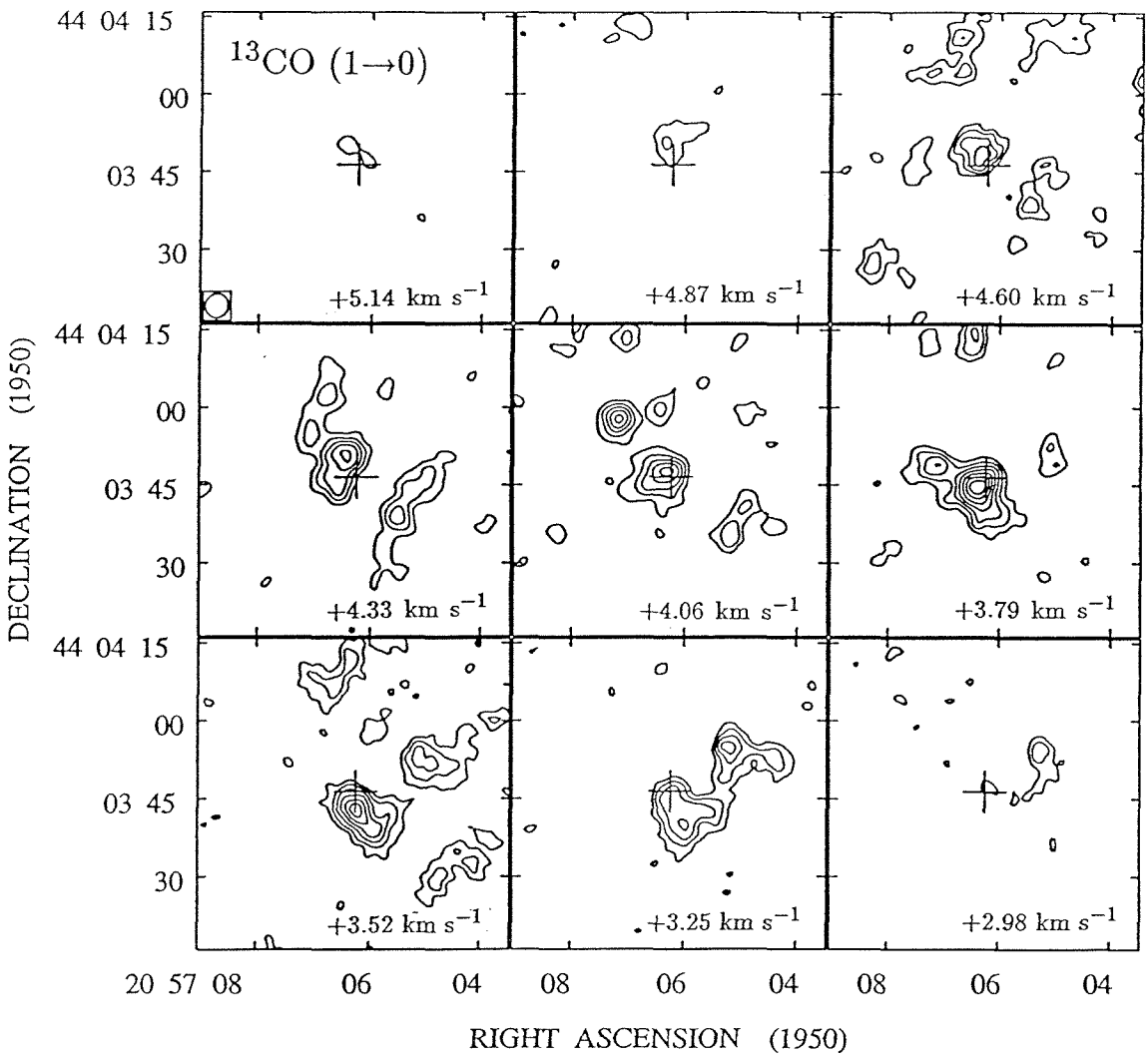

Figure 4.4. Individual channel maps of ^{13}CO (1→0) emission at 0.27 km s^{-1} velocity resolution. Contours begin at the 2σ level of 0.5 Jy/beam and are separated by 1σ.

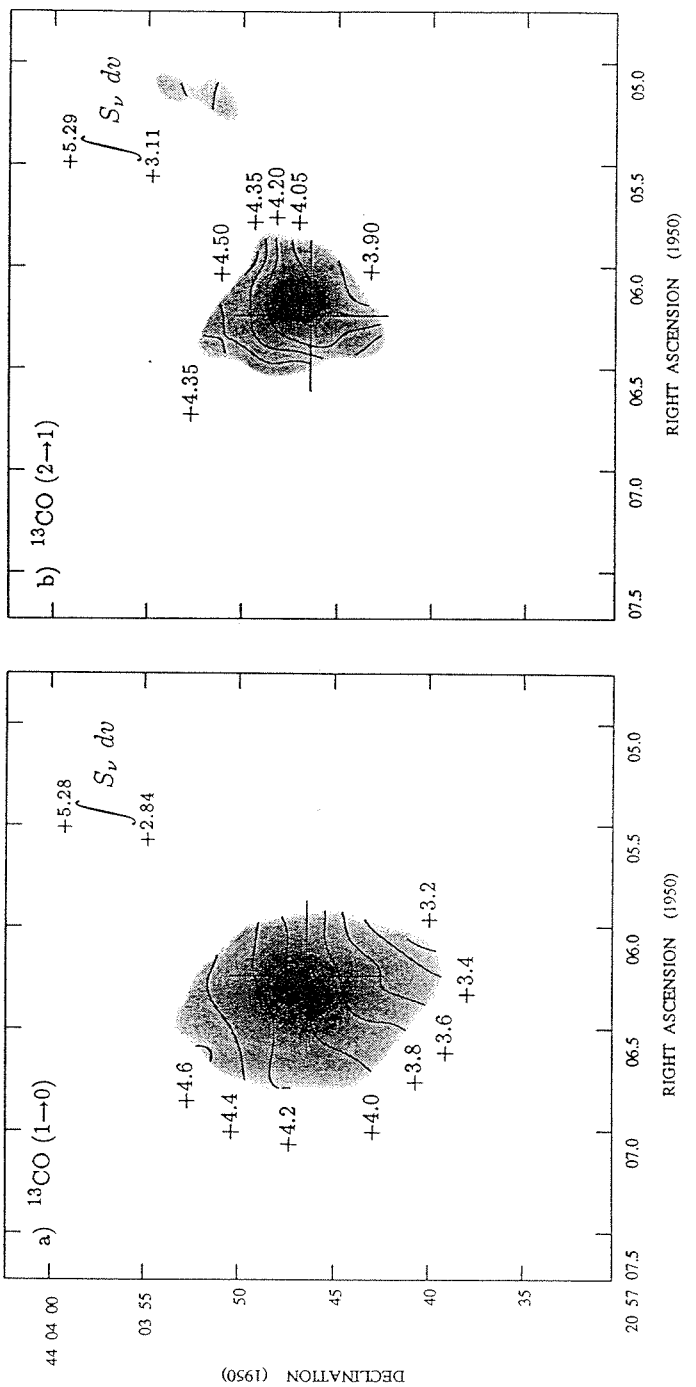

Figure 4.5. Aperture synthesis maps of ^{13}CO (1→0) and ^{13}CO (2→1) emission. Greyscale images show emission integrated over the velocity ranges +2.84 to +5.28 km s^{-1} and +3.11 to 5.29 km s^{-1} ^{13}CO (1→0) and (2→1) transitions respectively. Contours trace the velocity gradient and are separated by 0.2 and 0.15 km s^{-1}.

velocity trend along an axis perpendicular to the outflowing gas. This pattern is clear in Figure 4.5 (a) where the greyscale image traces ^{13}CO (1→0) emission integrated over the velocity range shown in Figure 4.4 and contours trace the velocity gradient, PA∼20°. Figure 4.5 (b) shows the ^{13}CO (2→1) emission over a comparable velocity range. The emission region, with peak flux 7.5 Jy/beam km s^{-1}, exhibits similar morphology and kinematics to that seen at ^{13}CO (1→0). In both cases, emission peaks within the uncertainties at the stellar position. Beam deconvolution yields a source size of 5300 × 3900 AU, PA 40°.

The mass of H_2 associated with the ^{13}CO (1→0) and ^{13}CO(2→1) emission regions in the immediate vicinity of V1057 Cygni can be calculated from their total integrated fluxes of 9.7 and 36.5 Jy km s^{-1} respectively (*cf* Scoville *et al.* 1986; McMuldroch *et al.* 1993). Adopting an abundance X(^{13}CO)=1.7 × 10^{-6} (Chackerian & Tipping 1983; Langer & Penzias 1993) and an excitation temperature of 20 K, we calculate minimum masses of 0.18 and 0.08 $M_\odot$ in the optically thin limit.

3.2.2 Outflowing Gas

Contours and greyscale in Figure 4.6 trace the CO (1→0) emission from V1057 Cygni over the velocities -3.6 to +9.4 km s^{-1}. No CO flux was detected outside this velocity range to a 3σ limit of 0.36 Jy/beam. Close to the systemic velocity between +0.3 and +5.5 km s^{-1}, molecular emission is concentrated near V1057 Cygni. Emission at greater distances extends linearly away from the FUor. Blueshifted gas lies between PA 0° and PA −60°, with the most distant emission tracing the reflection nebula seen in optical images (Goodrich 1987). By contrast, redshifted emission lies along PA 160° and does not correlate with optical images. Taken together, the molecular emission delineates a bipolar outflow, PA∼150±30°, in agreement with the outflow direction estimated from CSO measurements.

The emission appears "clumpy" in the 6″.0 × 5″.2 PA −4° beam. At

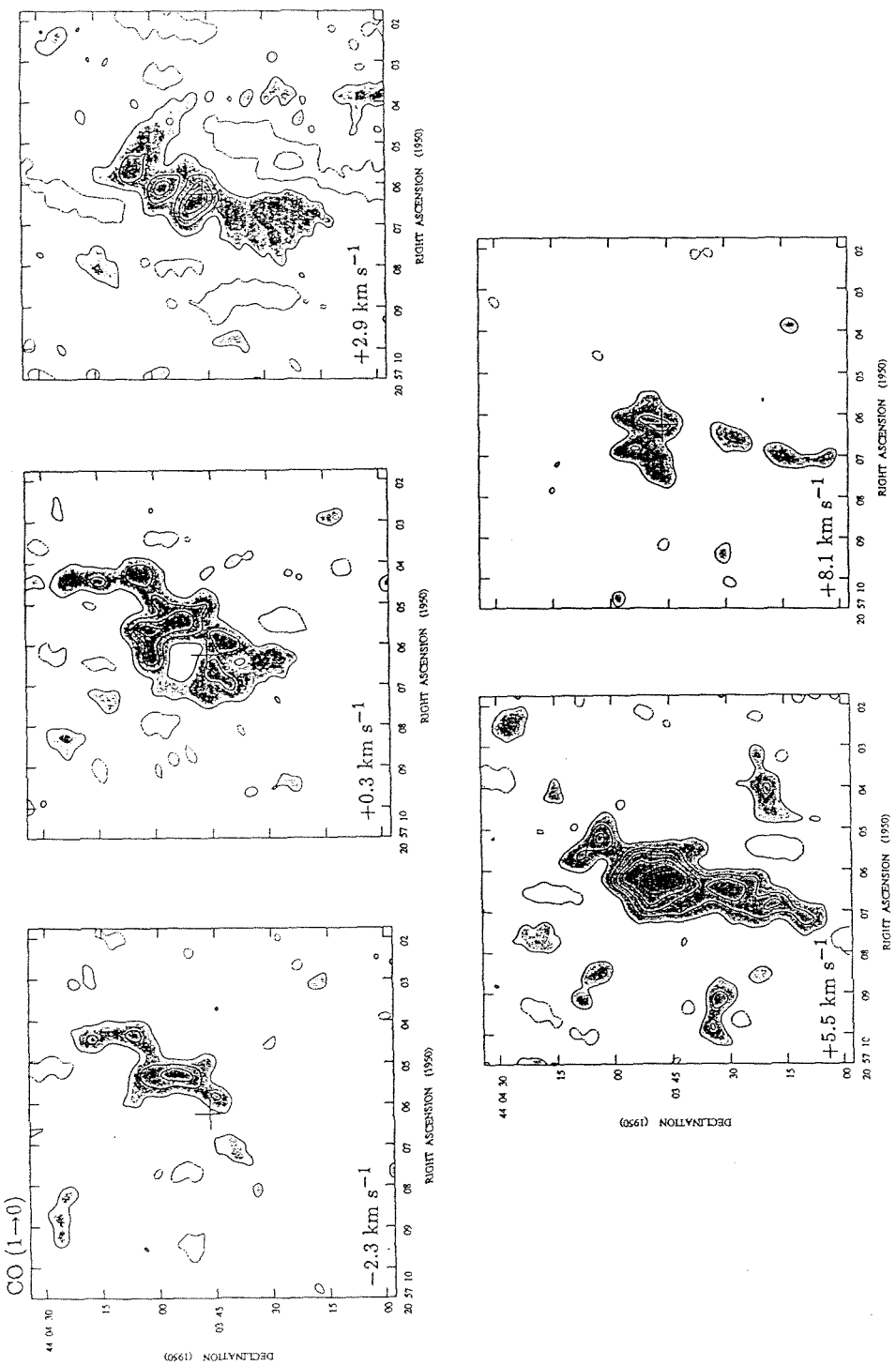

Figure 4.6. Contours delineate CO emission observed with the Owens Valley array. They begin at, and separated by, 2σ, 0.36 Jy/beam. Greyscale images also trace CO emission for clarity.

+2.9 km s^{-1}, two concentrations at distances of 12″ and 20″, PA∼60°, from the star are found. Similarly, contours at +5.5 km s^{-1} delineate two clumps, located at distances of 16″ and 28″ from V1057 Cygni, but lying at PA∼190°. The mass of H_2 in a clump can be calculated as before with parameters appropriate for CO (1→0) (*cf* Scoville *et al.* 1986; McMuldroch *et al.* 1993). For a typical clump of size 10″ × 5″ (7000 × 3500 AU), with an integrated flux of ∼5 Jy km s^{-1}, adopting an abundance X(CO)=10^{-4} and an excitation temperature of 10 K, we calculate a minimum mass of 10^{-3} $M_{\odot}$.

4. Discussion

4.1 Dust and Gas Surrounding V1057 Cygni

Models of the spectral energy distribution of V1057 Cygni are consistent with the presence of a centrifugally supported circumstellar disk surrounded by a more extended envelope (Weintraub *et al.* 1991; Kenyon & Hartmann 1991). Our measurements of the continuum emission at λ=1.3 mm probably arise from the envelope (*cf* Tereby *et al.* 1993) and yield a source size less than $\sim$1500 AU of mass $\geq$0.09 $M_{\odot}$.

In Figures 4.5 (a) and (b), our aperture synthesis maps reveal a larger molecular gas envelope surrounding V1057 Cygni of mass $\geq$0.2 $M_{\odot}$, size 7600 $\times$ 4700 AU, elongated at PA$\sim$40°, or approximately perpendicular to the molecular outflow direction. We calculate a column density towards the central source of n_{H_2} $\geq 1.4 \times 10^{22}$ cm^{-2} implying a visual extinction of $\geq$14, substantially larger than the the observed value of A_V=3.5$\pm$0.5 (Kenyon *et al.* 1988). This discrepancy probably results from the outflow evacuating material from directly around the star and from the gas being asymmetrically distributed in a flattened, disk-like structure observed nearly pole-on. Assuming circular symmetry, the envelope's aspect ratio suggests an inclination of $\sim$40°, slightly larger than previous estimates for the system.

As shown in Figures 4.5 (a) and (b), the molecular gas envelope surrounding V1057 Cygni exhibits a velocity gradient along PA 20°. Our maps suggest that the velocity pattern is minimally affected by outflowing gas. Indeed, the emission pattern shown in individual channel maps (Figure 4.4) possesses characteristics that could be interpreted as a combination of infall and rotation; near systemic velocities, emission is extended along the the major axis at PA 60°, indicative of infalling gas. However, inner contours are oriented perpendicularly to this, more characteristic of rotation. Emission at the largest velocities peaks furthest from the star as expected for solid-

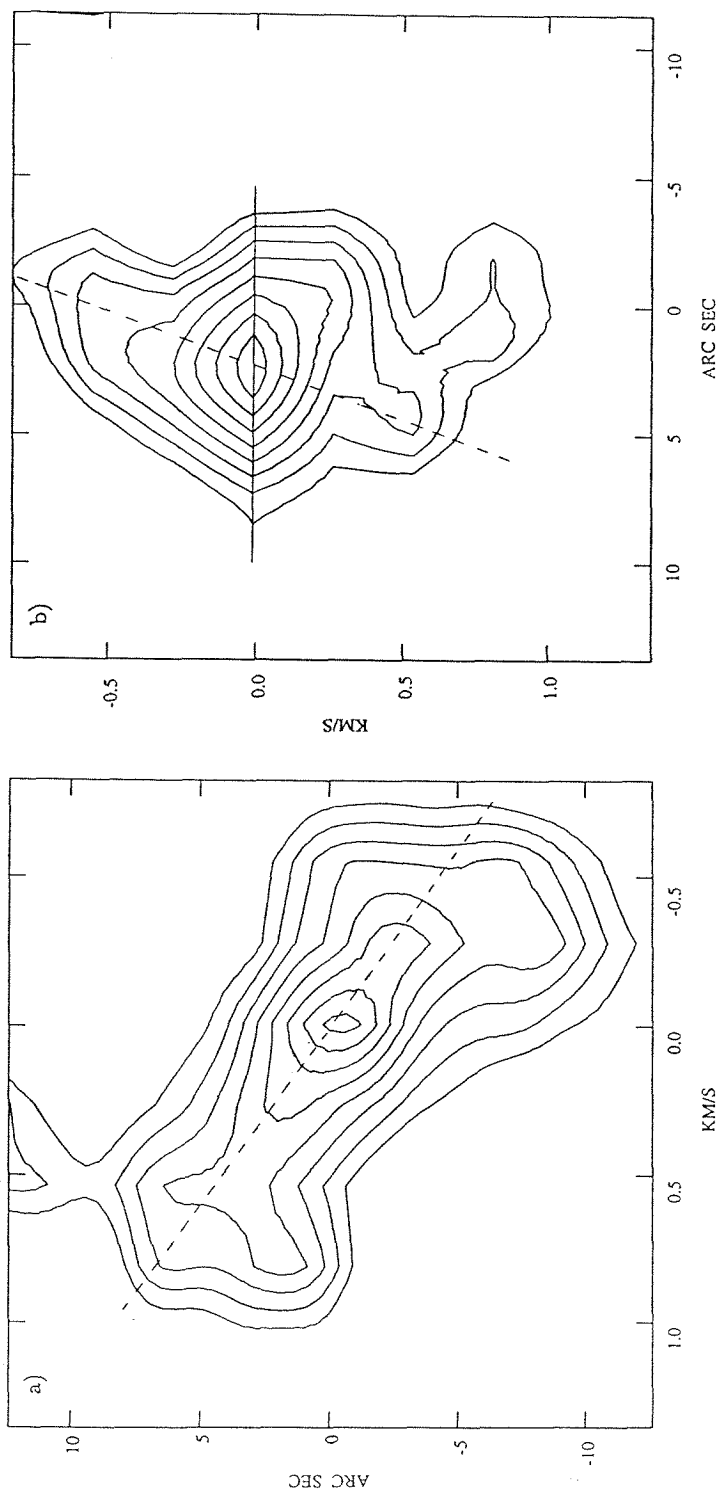

Figure 4.7. Position-velocity diagrams showing cuts along the major (PA 40°) and minor (PA 130°) axes respectively of the ^{13}CO (1→0) emission region. Contours in both figures begin at 6 Jy/beam and are spaced by 2 Jy/beam intervals.

body rotation. These tendencies are seen more clearly in Figures 4.7 (a) and (b) representing position-velocity cuts along the major axis, PA 40°, and minor axis, PA 130° respectively. In Figure 4.7 (a), the linear velocity trend marked by a dotted line possibly indicates rotation. Figure 4.7 (b) shows more complicated behavior with emission at the velocity extremes forming a linear trend at PA 160°, marked by a dotted line, while emission at systemic velocities is oriented at PA 90°. Emission at extreme velocities may trace infalling gas along the minor axis with redshifted material on the near side of the disk and blueshifted material opposite. The emission pattern at systemic velocities is confused by a combination of rotational velocity components. Overall, the size scales and disk-like structure are consistent with those of a large "pseudodisk" formed from the collapse of a molecular cloud core in the presence of a magnetic field (Galli & Shu 1993). Similar structures are also formed in the inviscid disk models of Stahler *et al.* (1994). Kinematic models confirm the existence of such disks around T Tauri stars (Koerner 1994). However, higher spatial resolution observations of V1057 Cygni are needed to determine the gas kinematics accurately and to confirm this hypothesis.

The large molecular gas envelope surrounding V1057 Cygni maybe infalling onto a centrifugally supported inner disk which drives the FUor outbursts. This gas disk, mass M_{env} $\geq$0.2 $M_{\odot}$, contains material for more than 20 high mass accretion events. From Figure 4.7 (b), we measure an average infall velocity of v_r $\sim$0.7 km s^{-1} correcting for projection effects. We estimate the mass accretion rate $\dot{M}_{env}=2\pi r_{env} v_r \Sigma$ to be $\geq 1.5 \times 10^{-5}$ $M_{\odot}$ yr^{-1} where the surface density $\Sigma=M_{env}/(\pi r_{env}^2)$. Although M_{env} and v_r are poorly constrained, this is smaller than the value of $\sim 10^{-4}$ derived from outburst luminosity measurements (*cf* Hartmann *et al.* 1993) which suggests that the present FUor outburst cannot be sustained by the current levels of mass accretion from the envelope. The FUor outburst will therefore continue to deplete the

mass of the inner disk until surface densities become sufficiently low that accretion rates drop to T Tauri levels, $\sim 10^{-6}$ $M_\odot$ yr^{-1}. Mass will then accumulate in the inner disk until the next FUor outburst. The time between outbursts, estimated from $t_{int} \sim \dot{M}_{out} t_{out} / \dot{M}_{env}$, is 600 years assuming a outburst mass accretion rate $\dot{M}_{out}=10^{-4}$ $M_\odot$ yr^{-1} and an outburst duration t_{out}=100 years. This is much smaller than the outburst interval of $\sim 10^4$ years implied by the number of FUors. However, estimates depend critically on values of v_r and Σ which are poorly constrained at these spatial resolutions with these transitions. Higher spatial observations in more optically thin transitions are needed to constrain v_r and Σ further to confirm this result.

4.2 Outflowing Gas

High resolution aperture synthesis maps trace a bipolar outflow along an axis at PA$\sim$150°, within 40″ of V1057 Cygni. The outflow is "clumpy" with concentrations of typical size 7000 × 3500 AU, mass 10^{-3} $M_\odot$. Two clumps are seen at comparable distances from V1057 Cygni in each outflow lobe. Although models of envelope emission suggest a low inclination for the V1057 Cygni system, the molecular outflow is at relatively low velocities. The clumps are therefore poorly coupled to the high velocity driving wind and probably do not result from any time-dependent events in the outflow source. Instead, emission probably traces inhomogenities in the surrounding cloud swept up by outflowing gas. Such short scale spatial variations are probably accentuated by the interferometer's ability to resolve out extended flux.

V1057 Cygni is surrounded by a reflection nebulosity that may trace the walls of an outflow shell (Goodrich 1987). Our aperture synthesis maps suggest that low velocity blueshifted ^{13}CO (1→0) emission traces the northwest arc of the reflection nebula. Blueshifted CO (1→0) emission partially traces the nebula but at greater distances from V1057 Cygni. We also suggest the emission associated

with the nebula traces gas swept-up at the edges of an outflow shell, formed by the blueshifted component of the bipolar outflow, and seen nearly pole-on. However, the reflection nebula is oriented at PA$\sim$45°, compared to the bipolar outflow PA$\sim$150°. This suggests the outflow may wander in direction or be more uncollimated than suggested by our OVRO maps.

CSO maps of CO (2$\rightarrow$1) emission trace the bipolar outflow, PA$\sim$0°, up 80″ away from the FUor. Calculations yield mass and momentum estimates for the blue and redshifted lobes of 2.8 $M_\odot$ and 10.2 $M_\odot$ km s^{-1}, and 0.36 $M_\odot$ and 0.7 $M_\odot$ km s^{-1} respectively. We estimate a dynamical age of the outflow from the blueshifted lobe as 9.4 $\times$ 10^4 years and derive an average mass loss rate of 2.4 $\times$ 10^{-7} $M_\odot$ yr^{-1}, assuming a wind velocity of 480 km s^{-1} (Levreault 1988). If outbursts occur every $\sim$600 years, as suggested by our infalling envelope calculations, then V1057 Cygni may have experienced $\gtrsim$150 outbursts. Outburst statistics suggest FUor undergo between 10-100 events. For typical FUor mass loss rates of 10^{-5} $M_\odot$ yr^{-1} and an outburst duration of 100 years, the total momentum entrained in the outflow would be $\sim$26 $M_\odot$ km s^{-1}. This suggests that either the repetition timescale estimated in our envelope calculations is too small or that V1057 Cygni underwent fewer outbursts in the past.

5. Conclusions

We have carried out sensitive high resolution millimeter and submillimeter observations of the FU Orionis object V1057 Cygni. Aperture synthesis maps of the CO (1$\rightarrow$0), ^{13}CO (1$\rightarrow$0), ^{13}CO (2$\rightarrow$1) and associated continuum emission trace an unresolved 0.09 $M_\odot$ dusty envelope surrounded by a extended molecular gas envelope, 7500 $\times$ 4700 AU in size, mass $\geq$0.2 $M_\odot$.

Estimates of the visual extinction towards the central source are larger than observed values implying that the molecular gas envelope is flattened. Gas kinematics

are consistent with both infalling and rotating material. The size scales and structure are consistent with the large molecular gas disks predicted by theoretical models (Galli & Shu 1994; Stahler 1994). For gas infalling at 0.7 km s^{-1}, we estimate a mass accretion rate onto the inner disk of $\dot{M}_{env} \geq 1.5 \times 10^{-5}\ M_{\odot}\ yr^{-1}$. This infall rate cannot sustain the current FU Orionis outburst. Once accretion rates revert to T Tauri levels of $\sim 10^{-6}\ M_{\odot}\ yr^{-1}$, mass will begin to accumulate in the inner disk until the next FU Orionis outburst. We calculate an average time interval between outbursts of ~600 years, shorter than estimates implied by the frequency of FU Orionis objects, suggesting that V1057 Cygni may undergo outbursts more frequently or that outburst duration is longer than the usually assumed 100 years. However, higher spatial resolution observations are needed to determine the gas kinematics accurately.

Maps of blueshifted ^{13}CO (1→0) emission trace the northwest arc of the reflection nebula. Blueshifted CO (1→0) emission also traces the reflection nebulosity but at greater distances from the star. Emission probably delineates the walls of a swept-up shell of outflowing molecular gas. Further from the star, aperture synthesis maps of CO (1→0) emission and maps from the CSO of CO (2→1) emission trace a bipolar outflow oriented at PA 150°of mass ~3.2 $M_{\odot}$, age 9.4×10^4 years. The outflow is "clumpy" with concentrations of typical size 7000 × 3500 AU, mass $10^{-3}\ M_{\odot}$. Such clumps probably arise from inhomogenities in the surrounding cloud being swept-up by outflowing gas.

CHAPTER 5

The Outflow Cavity of the FU Orionis Object Elias 1-12

1. Introduction

The fourth member to be added to the FUor class was the young star V1735 Cygni or Elias 1-12, which rose to maximum light sometime between 1957 and 1965 (Elias 1978; Rodríguez *et al.* 1990). Located in the dark cloud IC 5146, some 900 pc away in Cygnus, the high optical extinction of $A_v \sim 10^m$ towards the star makes stellar classification difficult. However, the object possesses the spectral energy distribution, reflection nebulosity, wavelength dependent spectral type, and P Cygni profiles characteristic of an FU Orionis object (Elias 1978; Bastien & Mundt 1985; Goodrich 1987).

Submillimeter and millimeter continuum observations suggest Elias 1-12 is surrounded by a circumstellar disk of mass $\leq 0.2\ M_\odot$, assuming an emissivity dependence of β=2 (Weintraub *et al.* 1991). At 800 μm the emission is resolved into an extended dusty envelope $18'' \times 24''$ in size surrounding Elias 1-12 (Weintraub *et al.* 1991). Infrared observations suggest the dust temperature is less than 45 K (Evans *et al.* 1986). Single dish studies of molecular line emission in the rotational transitions of CO, ^{13}CO, and HCO^+ in the 115, 230 and 345 GHz bands reveal an area of disturbed gas, 0.3 pc in diameter, centered on the FUor (Levreault 1983, 1988; Evans *et al.* 1994). The complicated outflow geometry may result from a dense swept-up shell of predominantly redshifted gas or from two separate outflows powered by Elias 1-12 and another, yet undetected, source (Levreault 1983; Evans *et al.* 1994). At centimeter wavelengths the continuum flux spectral index is 0.7, typical of free-free emission. This could arise from ionized gas in the driving wind (Rodríguez *et al.* 1990).

2. Observations

2.1 CSO Observations

Single telescope observations towards Elias 1-12 were acquired with the Caltech Submillimeter Observatory (CSO) on Mauna Kea, Hawaii, in 1991 July. The facility 230 and 345 GHz receivers were used in conjunction with the CSO 500 and 50 MHz acousto-optical spectrometers (Ellison & Miller 1987; Ellison *et al.* 1989). Position switching to a reference position 30′ east, 15′ north of the source produced the least contaminated spectra. All quoted temperatures have been corrected for main beam efficiencies of 0.52 and 0.58 at 230 and 345 GHz respectively. For further information concerning the observational technique see Chapter 2.

Table 5.1 lists the molecular species detected towards Elias 1-12 in the 230 and 345 GHz bands. Spectra were acquired for the CO (3→2), CO (2→1), ^{13}CO (2→1), C^{18}O (2→1), HCN (4→3), CH_3OH ($4_2 \rightarrow 3_1$), HCO^+ (4→3), and H_2CO ($3_{0,3} \rightarrow 2_{0,2}$) rotational transitions. Emission from SiO (5→4), SO ($5_6 \rightarrow 4_5$), H_2CO ($3_{2,2} \rightarrow 2_{2,1}$), and CS (7→6) was searched for but not detected to 3σ limits of 0.27 K.

2.2 OVRO Observations

Aperture synthesis mapping of the ^{12}CO (1→0), ^{13}CO (1→0), and C^{18}O (1→0) rotational transitions at ν=115.271, 110.201, and 109.782 GHz, respectively, was carried out using the Owens Valley millimeter-wave interferometer between 1993 September and 1993 October. System temperatures were typically 560 and 320 K (SSB) at 115 and 110 GHz. The OVRO digital correlator provided velocity resolutions of 0.33 and 1.30 km s^{-1} at 115 GHz and 0.34 km s^{-1} at 110 GHz. Simultaneous continuum observations were obtained at 2.7 mm in a broadband channel of effective width 1 GHz. Both the correlator and broadband channel were centered on the systemic velocity of the star, v_{LSR} = 3.9 km s^{-1} (Levreault 1988).

Phase and amplitude gains were established by observing the quasar BL Lac

(1) Molecule	(2) Transition	(3) ν (GHz)	(4) Peak T (K)	(5) FWHM (kms^{-1})	(6) Velocity (kms^{-1})	(7) $\int Tdv$ (K kms^{-1})	(8) Wings	(9) N (cm^{-2})	(10) $F_{C^{18}O}$	(11) F_{TMC1}
H_2CO	$3_{0,3} \rightarrow 2_{0,2}$	218.222	0.8	3.1	3.8	2.7	red?	2(13)	8(-10)	2(-8)
CH_3OH	$4_2 \rightarrow 3_1$	218.440	0.2	4.1?	3.2	0.6	?	2(14)	6(-9)	2(-9)
$C^{18}O$	2→1	219.560	2.9	1.9	3.9	8.5	weak	5(15)		2(-7)
^{13}CO	2→1	220.399	5.5	2.7	3.9	19.0	yes	–	–	1(-6)
CO	2→1	230.538	10.3	–	–	–	strong	–	–	8(-5)
CO	3→2	345.796	9.8	–	–	–	strong	–	–	8(-5)
HCN	4→3	354.505	0.4	4.1	3.3	2.0	red?	2(12)	8(-11)	2(-8)
HCO^+	4→3	356.734	2.1	–	–	–	red?	–	–	8(-9)

Table 5.1.

at 25 minute intervals. The absolute flux scale was established by measurements of Uranus. Maps were generated from calibrated visibility data using the NRAO AIPS software package. Maximum unprojected baselines of 60 m north-south and 60 m east-west gave naturally weighted synthesized beams of 6″.7 × 5″.5, PA 85° at 115 GHz and 7″.2 × 5″.8, PA 85° at 110 GHz. For these beams and frequencies, T_B = 1 K corresponds to 0.36 and 0.42 Jy/beam respectively. Individual maps were constructed from observations taken at three phase centers, namely the position of Elias 1-12 at α (1950) = 21^h 45^m 26.9^s, δ (1950) = +47° 18′ 8″.0, together with a second center P2 at α (1950) = 21^h 45^m 29.4^s, δ (1950) = +47° 18′ 23″.0 and a third center P3 at α (1950) = 21^h 45^m 27.9^s, δ (1950) = +47° 17′ 38″.0. These positions optimally encompass the outflow mapped with filled aperture telescopes (Levreault 1983; Evans *et al.* 1994) and the region of the optical reflection nebula. Positional accuracy is ± 2″.

3. Results

3.1 CSO Results

Table 5.1 lists the line parameters and integrated fluxes of molecular species observed toward Elias 1-12 with the CSO. Dashes indicate where spectra are affected by self-absorption or outflow, while question marks indicate a low signal-to-noise ratio. The velocity of peak flux is indicated in column 6; most molecules peak near the systemic velocity of 3.9 km s^{-1}. The total integrated flux is listed in column 7 while the presence of wing emission is indicated in column 8. Column densities, calculated using an LTE code in the optically thin regime, are listed in column 9.

3.1.1 The Cloud Core

The spectra of H_2CO, CH_3OH, $C^{18}O$, and HCN show little or no evidence of outflowing gas and no evidence of self-absorption. Column 9 lists the column densities for these species calculated using an LTE code assuming a temperature of 20 K, typical of circumstellar molecular gas and consistent with the infrared observations of Evans *et al.* (1986). The fractional abundances for each molecular species was then calculated by dividing species column density by the total H_2 column density, estimated from $C^{18}O$ measurements assuming a canonical abundance of $C^{18}O/H_2 = 2 \times 10^{-7}$ (Chackerian & Tipping 1983). The strength of the $C^{18}O$ transition was used to estimate N_{H_2} since its low optical depth, τ=0.75, calculated from relative line intensities, and low critical density make it an optimal tracer of the total molecular mass. Column 10 in Table 5.1 lists the derived fractional abundances while column 11 lists fractional abundances of the cold core TMC 1 for comparison (van Dishoeck *et al.* 1993 and references therein). The abundance of CH_3OH is comparable to that found in TMC 1 while H_2CO and HCN are depleted by factors of ~30 and ~270 respectively.

3.1.2 Outflowing Gas

Figure 5.1 shows the ^{12}CO (3→2), ^{12}CO (2→1), ^{13}CO (2→1), and C^{18}O (2→1) spectra at the position of Elias 1-12. The CO (3→2) and CO (2→1) line profiles show minima at +3.2 and +4.1 km s^{-1} indicative of self-absorption and cold foreground gas. HCO$^+$ also shows a self-absorption minimum at +3.2 km s^{-1}. All lines presented in 5.1 possess display blue and redshifted outflow wings, although C^{18}O wing emission is very weak. Comparison of C^{18}O and CO line profiles suggest wing emission extends from −4.5 to +0.5 km s^{-1} and +7.0 to +18.0 km s^{-1}, values similar to earlier estimates (Levreault 1983; Evans *et al.* 1994). Relative line strengths yield optical depths of $\tau_{^{13}CO}$=0.43 and 0.08 for the blue and red wings respectively, assuming CO emission is optically thick.

3.2 OVRO Results

Dust continuum emission from Elias 1-12 was not detected at 2.7 mm to a 3σ limit of 6 mJy/beam. This is consistent with extrapolations from measurements taken at shorter wavelengths which suggest a 2.7 mm flux of 4.5 mJy/beam (Weintraub *et al.* 1991). By comparison, molecular gas emission was detected in all three observed transitions.

Figure 5.2 shows the individual channel maps, velocity resolution 0.34 km s^{-1}, of C^{18}O (1→0) emission toward Elias 1-12. The position of the FUor is marked by a cross 8″ in size while the positions of the two other pointing centers are indicated by 4″ crosses. No emission was detected outside of these velocities to a 3σ limit of 0.3 Jy/beam. Emission at +3.22 km s^{-1} peaks ∼2″ northeast of the stellar position; at redshifted velocities emission peaks to the southwest. Emission is also apparent ∼25″ north of Elias 1-12 near the second pointing position (P2).

Emission from the rotational transition of ^{13}CO (1→0) was detected between velocities of +0.67 and +8.49 km s^{-1} to a 3σ limit of 0.1 Jy/beam. Figure

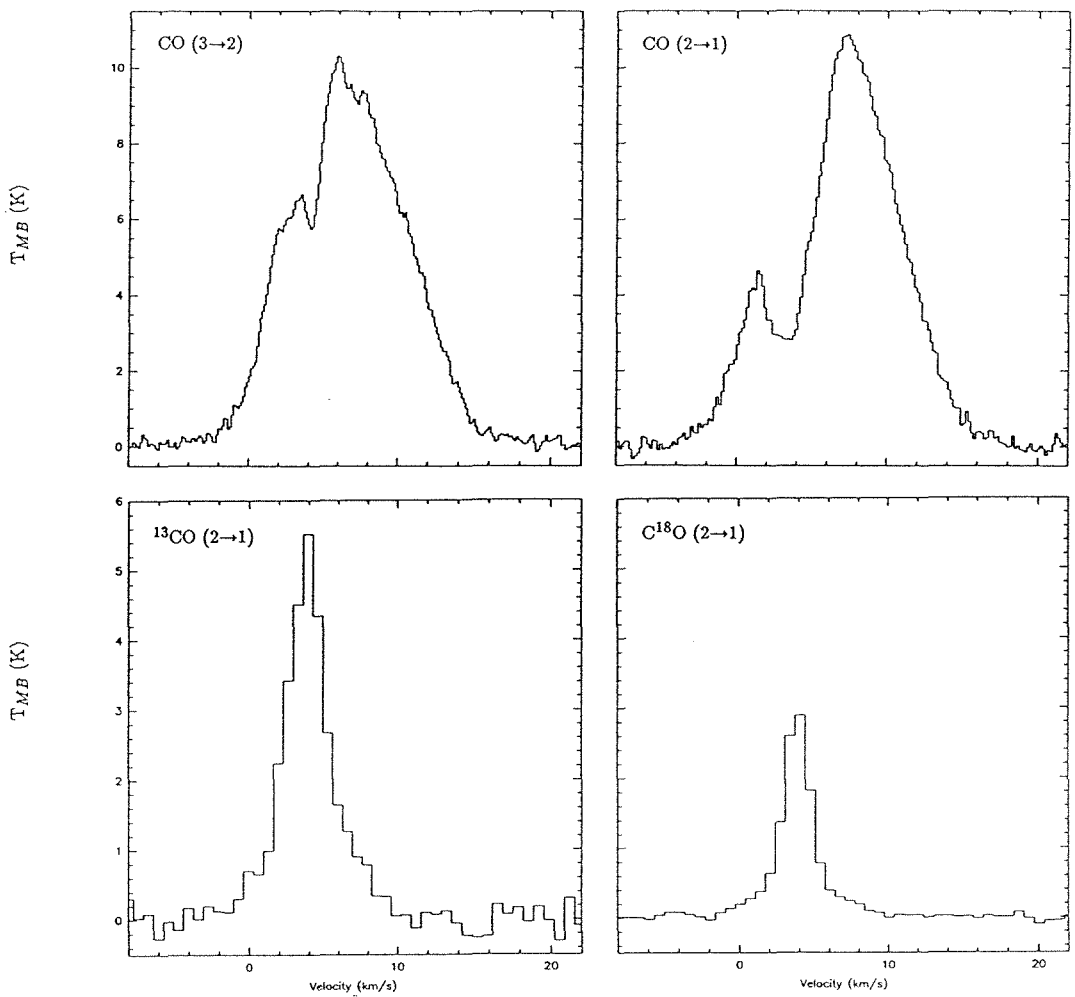

Figure 5.1. Line emission in ^{12}CO (3→2), ^{12}CO (2→1), ^{13}CO (2→1), and C^{18}O (2→1) as detected at the CSO. Temperatures have been corrected for main beam efficiencies.

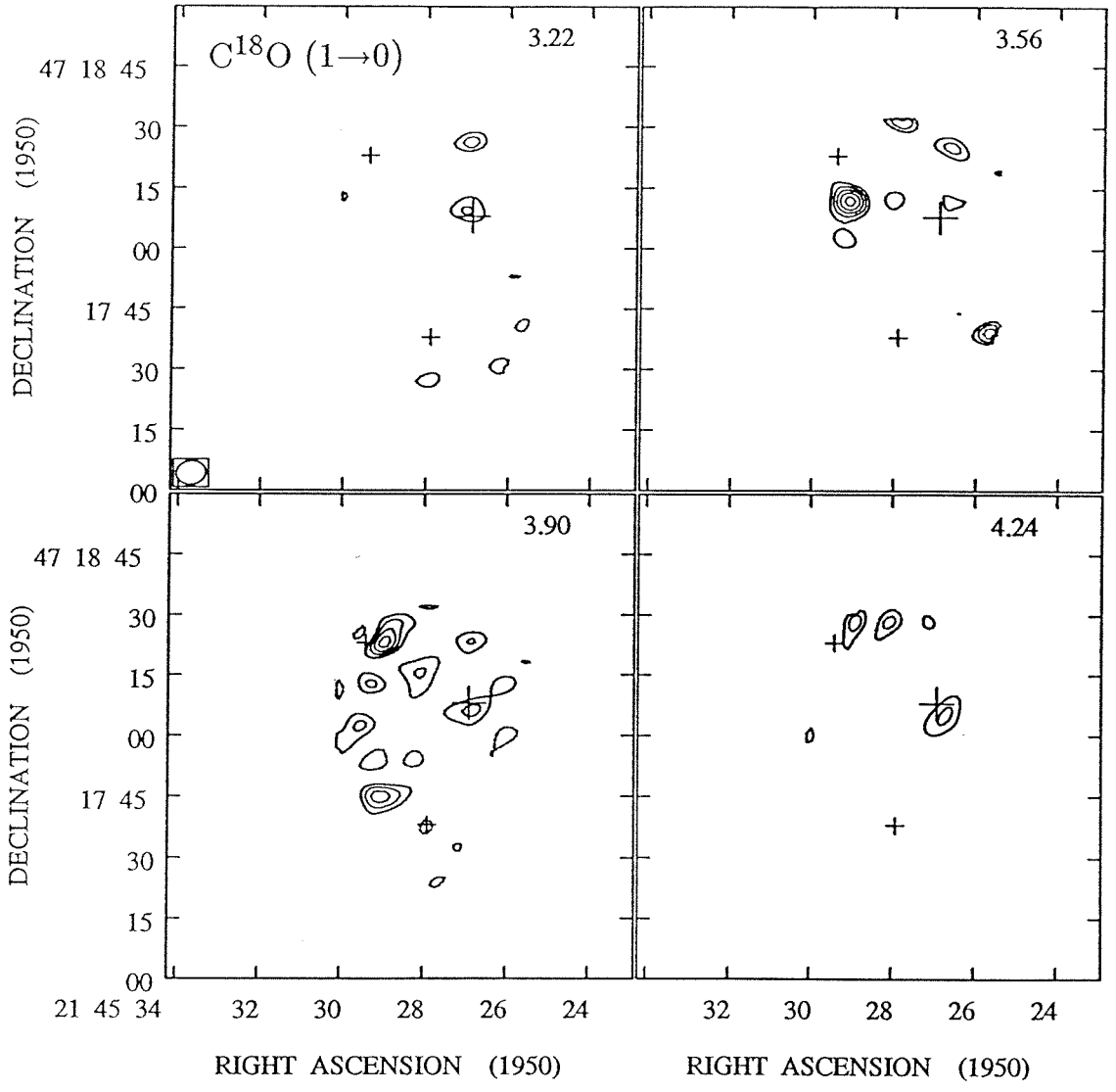

Figure 5.2. Individual channel maps of $C^{18}O$ emission from Elias 1-12 detected by the Owens Valley millimeter-wave interferometer. Contours are separated by 1σ, and begin at the 2σ level of 0.2 Jy/beam. A cross 8″ in size marks the position of Elias 1-12 while smaller crosses, 4″ in size, indicate the positions of the other pointing centers. An ellipse in the lower left corner denotes the size of the synthesised beam.

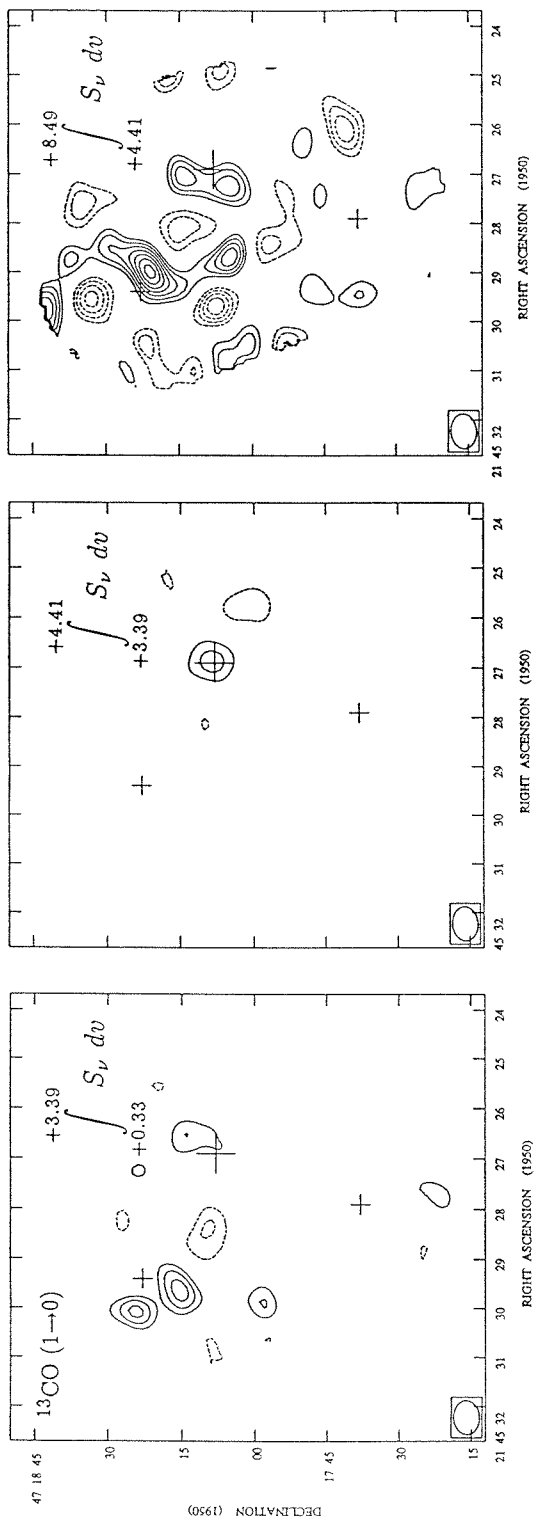

Figure 5.3. Aperture synthesis maps of the ^{13}CO (1→0) emission integrated over the velocity ranges +0.33 to +3.39 km s^{-1}, +3.39 to +4.41 km s^{-1}, and +4.41 to +8.49 km s^{-1}. Contours in each map begin at 20% of the peak total integrated flux, 1.23 Jy/beam km s^{-1}, and are separated by 10%.

5.3 shows blueshifted, systemic, and redshifted ^{13}CO emission integrated over the velocity ranges +0.33 to +3.39 km s^{-1}, +3.39 to +4.41 km s^{-1}, and +4.41 to +8.49 km s^{-1} respectively. These velocity bins were chosen to emphasize the distinct morphologies evident in individual channel maps. The blueshifted emission peak of 0.57 Jy/beam km s^{-1} lies 9″ south of the second pointing position. Weak emission is also detected ~6″ northwest of Elias 1-12. At systemic velocities, the peak flux occurs at the stellar position and is unresolved in the 7″.1 × 5″.4, PA −85° beam; no emission comparable to that seen at blueshifted velocities is present near P2. Flux at redshifted velocities also peaks close to the second pointing center and is extended forming a ridge elongated at PA 140°. A smaller peak lies ~20″ east of the FUor and is linked at low signal to noise levels with the emission near P2. Weak emission, elongated along PA 0°, is present within ~4″ of the stellar position.

Figures 5.4 (a)-(c) show aperture synthesis maps of CO (1→0) line emission towards Elias 1-12 in the velocity ranges −3.25 to +1.95 km s^{-1}, +4.55 to +8.45 km s^{-1}, and +8.45 to +16.25 km s^{-1}. No flux was detected outside of these velocity ranges to a 3σ limit of 0.6 Jy/beam. Blueshifted emission, shown in Figure 5.4 (a), extends radially away from Elias 1-12 starting near P2. Near the systemic velocity between +1.95 and +4.55 km s^{-1}, individual channel maps show minimal flux, possibly because emission is self-absorbed in this velocity range, as indicated by CSO measurements. CO is probably very optically thick at these velocities and is not a reliable indicator of the gas structure. Redshifted emission between +4.55 to +16.25 km s^{-1}, shown in Figure 5.4 (b), peaks ~4″ east of the stellar position. Emission is also seen up to 55″ away to the northeast and east. Within 25″, emission is concentrated to the north of the stellar position. The linear feature detected at ^{13}CO (1→0) at these velocities is not evident possibly due to emission being self-absorbed. Taken together, the emission pattern resembles a parabola, oriented at

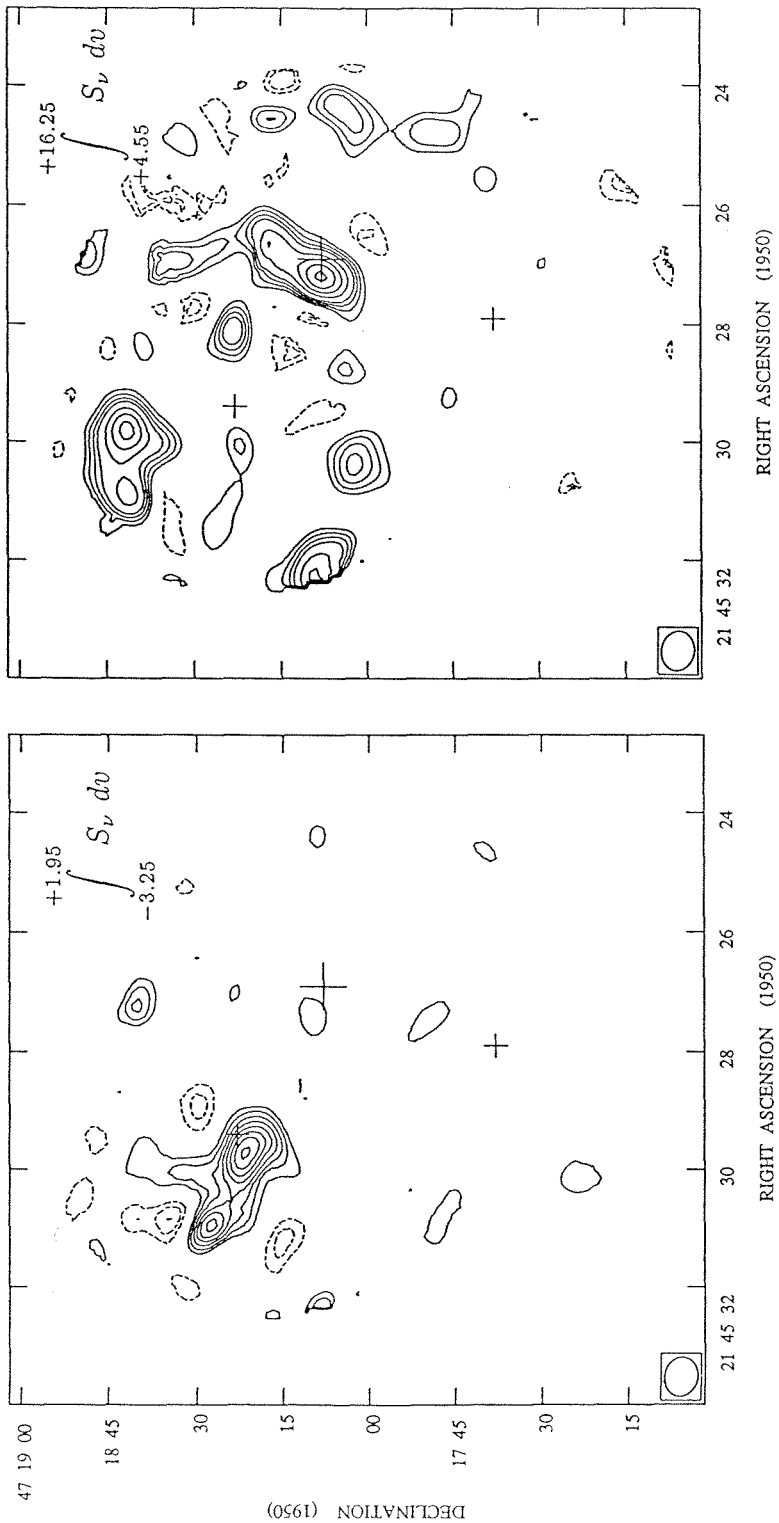

Figure 5.4. Contours in (a) and (b) trace CO (1→0) emission integrated over velocities −3.25 to +1.95 km s^{-1} and +4.55 to 16.25 km s^{-1}. Contours in (a) begin at 2 Jy/beam km s^{-1} and are separated by 1 Jy/beam km s^{-1}. In (b), contours are at −4, −3, −2, 2, 3, 4, 5, 7, 9, 11, and 13 Jy/beam km s^{-1}.

PA$\sim$45°, with Elias 1-12 at the apex.

4. Discussion

4.1 Chemistry

Several molecules were detected at the CSO towards the FUor Elias 1-12 in the 230 and 345 GHz bands. Fractional abundances of the quiescent gas, calculated by dividing species column density derived from an LTE code by the column density of $C^{18}O$, are presented in Table 5.1. For comparison, this table also presents the abundances found in the TMC 1 dark cloud.

Around Elias 1-12 the abundance of methanol is comparable to, or perhaps slightly enhanced over, that of TMC 1. However, both HCN and H_2CO are depleted by orders of magnitude. While small enrichments may result from density and temperature effects, such large depletions are probably the result of chemical interactions. Outflow shocks can drive new reaction routes even for low luminosity sources. However, any shock powerful enough to dissociate HCN and H_2CO would also destroy methanol.

The low fractional abundances of HCN and H_2CO are probably caused by depletion onto dust mantles. In such instances, methanol should be trapped in a water rich amorphous ice. However, if heated to $\sim$140 K, the ice can spontaneously form a highly porous type II clathrate hydrate (Blake *et al.* 1991). Any methanol above a 7% abundance ratio with respect to water is driven out to form a highly volatile surface layer around the clathrate substrate. By comparison other molecules, such as HCN and H_2CO, can be retained in the smaller more numerous cage sites, up to abundances of 14% that of water. Methanol would therefore be enhanced in the gas phase relative to other molecules. Such heating may result from low velocity grain-grain collisions in the turbulent shear zones present in bipolar outflows. Therefore, the relative molecular abundances measured towards Elias 1-12 may result from depletion of HCN and H_2CO onto grains coupled with the return of methanol into the gas phase

by grain-grain collisions in the outflow.

4.2 The Envelope Surrounding Elias 1-12

Aperture synthesis maps reveal a molecular gas condensation surrounding Elias 1-12 (see Figures 5.2, 5.3 (b), and 5.4 (b)). Relative emission line strengths towards the FUor, measured in maps of comparable velocity resolution, suggest that CO and ^{13}CO are optically thick while C^{18}O is optically thin with $\tau_{C^{18}O}$=0.8. C^{18}O emission therefore optimally traces the mass and kinematics of gas in the immediate vicinity of Elias 1-12.

The greyscale image in Figure 5.5 shows the total integrated C^{18}O emission towards Elias 1-12. The peak of 0.32 Jy/beam km s^{-1} occurs, within the positional uncertainties, at the stellar position. Deconvolution yields a source size of 9$''$.1 $\times$ 5$''$.1 (8200 $\times$ 4600 AU), PA 105°. The total mass surrounding the star can be calculated from the C^{18}O integrated flux density of 0.8 Jy km s^{-1} using:

$$M = 1.39 \times 10^{-2} \frac{(T_x + 0.88)}{e^{-5.27/T_x}} \frac{\tau_{CO}}{(1 - e^{-\tau_{CO}})} D_{kpc}^2 \int S_\nu \, dv \qquad M_\odot, \qquad (1)$$

Adopting an abundance ratio of C^{18}O/H$_2$ = 2 $\times$ 10^{-7} (Chackerian & Tipping 1983), an excitation temperature of 20 K, and an optical depth $\tau_{C^{18}O}$=0.8, the mass surrounding the FUor is 0.36 $M_\odot$. If distributed spherically, this mass would give an extinction of A$_v$ $\geq$25, somewhat larger than the observed value of A$_v$ $\sim$11. This may result from gas evacuating material from around the poles or from gas lying in a disk-like structure.

Contours in Figure 5.5 trace a velocity gradient oriented between PA 30°and 0°. Optically thick CO (1$\rightarrow$0) emission, which is detectable at low column densities and is most sensitive to outflowing gas, does not show similar kinematics. C^{18}O emission may therefore trace either infalling or rotating gas. Optical polarization

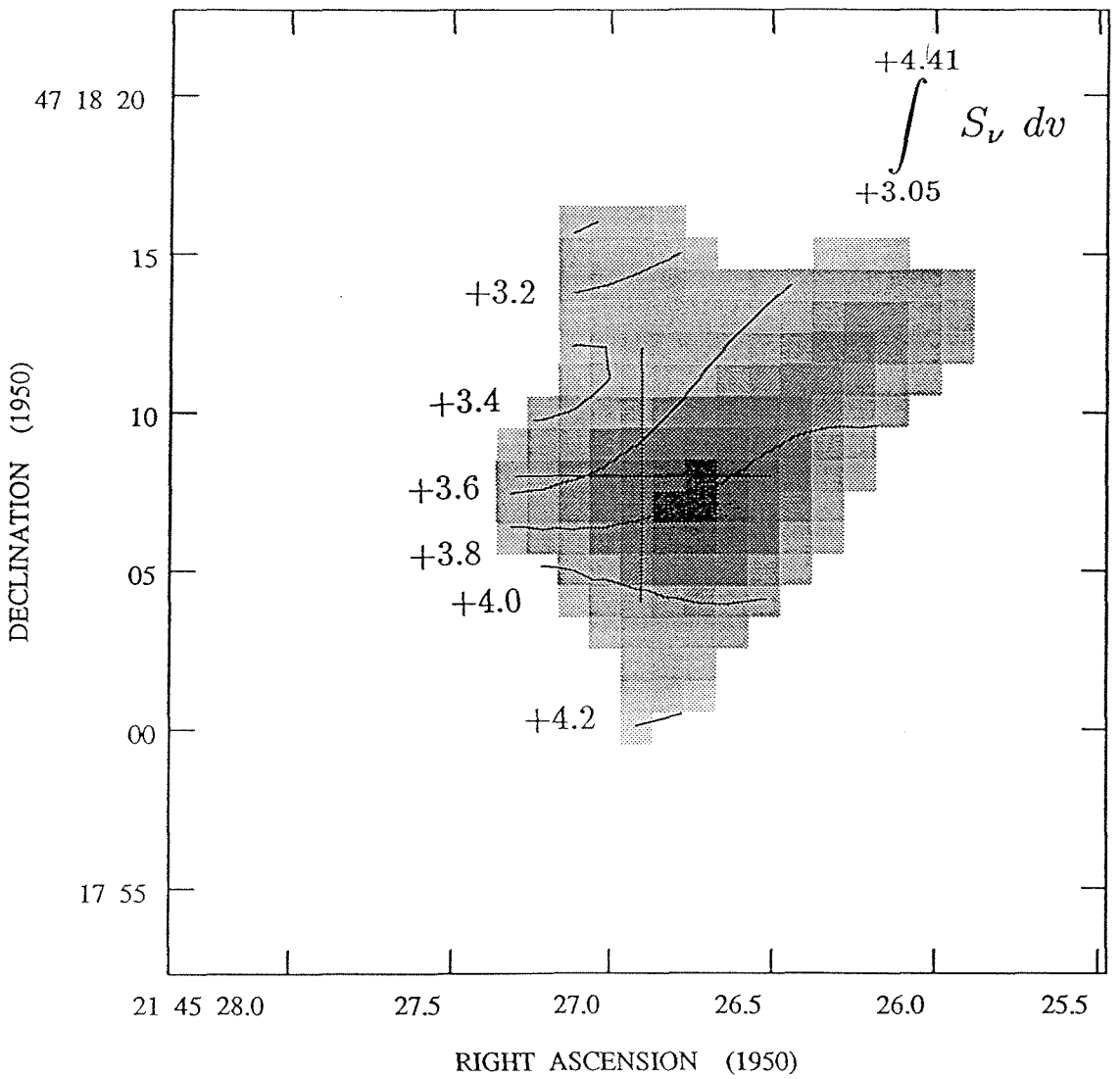

Figure 5.5. Aperture synthesis map of $C^{18}O$ (1→0) emission. The greyscale image shows emission integrated over the velocity range +3.05 to 4.41 km s^{-1}. Contours trace the velocity gradient and are separated by 0.2 km s^{-1}.

measurements suggest the envelope is elongated along PA$\sim$17°, perpendicular to the direction suggested by the OVRO maps (Ménard & Bastien 1992; Whitney & Hartmann 1994). Polarization studies at optical wavelengths may possibly be effected by dust not associated with the envelope in such an embedded source as Elias 1-12. However, emission in the aperture synthesis maps is at low signal to noise ratios. The orientation of the outflow should be approximately perpendicular to the envelope's elongation. The envelope elongation deduced from aperture synthesis maps of PA 105°. is most consistent with the direction of outflowing gas at PA 45°. The $C^{18}O$ velocity gradient is approximately perpendicular to the elongation of the envelope consistent with emission arising from infalling gas. However, more sensitive higher spatial resolution observations are needed to conclusively determine whether gas is infalling or rotating.

4.3 Outflowing Gas

CSO observations reveal strong redshifted and weak blueshifted wing emission in CO (3$\rightarrow$2), CO (2$\rightarrow$1), and ^{13}CO (2$\rightarrow$1) (see Figure 5.1). Wing emission is also evident at $C^{18}O$ (2$\rightarrow$1) but at low signal to noise levels (Figure 5.1). The large velocity displacements from the systemic value suggest emission arises from outflowing gas. Figure 5.6 reveals the outflow morphology as mapped by the Owens Valley millimeter-wave interferometer at high spatial resolution. Redshifted CO (1$\rightarrow$0) emission, integrated over the velocity range +4.55 to +16.25 km s^{-1}, is shown in solid contours. Negative emission has been excluded for clarity. Emission forms a paraboloid with Elias 1-12 at the apex. Blueshifted CO (1$\rightarrow$0) emission, integrated between velocities -3.25 to +1.95 km s^{-1}, is indicated by broken contours. The outflowing gas extends radially away from Elias 1-12 starting at the ridge traced by redshifted ^{13}CO (1$\rightarrow$0) emission shown in greyscale. The large visual extinction towards Elias 1-12 suggests a high inclination for the system with the star being

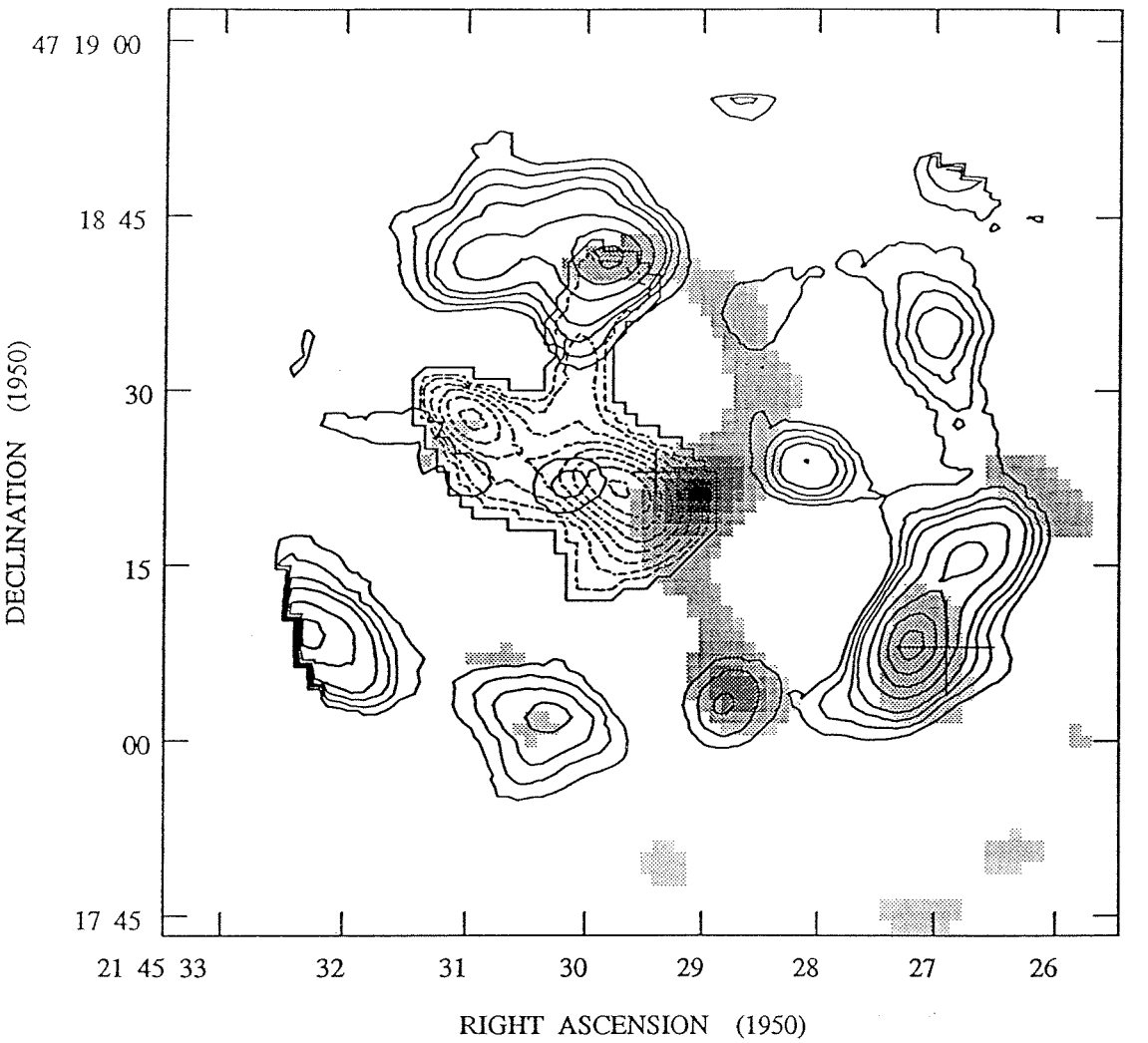

Figure 5.6. Composite map of CO and ^{13}CO (1→0) integrated emission. Solid contours trace redshifted CO emission integrated between velocities +4.55 and 16.25 km s^{-1}. Broken contours delineate blueshifted CO emission integrated over the velocity range −3.25 to 1.95 km s^{-1}. Contour levels are as for Figures 5.4 (a) and (b). The greyscale image shows ^{13}CO emission integrated over velocities +4.41 to +8.49 km s^{-1}.

viewed through the surrounding envelope (Kenyon & Hartmann 1991). Indeed, the overall morphology is consistent with a redshifted conical outflow shell, aligned at PA$\sim$45°, and lying partly in the plane of the sky. Redshifted CO emission delineates the cavity walls while blueshifted emission traces the section of the shell closest to us. Single dish maps possibly reveal the complementary blueshifted component to the southwest of the star (Evans *et al.* 1994). This component is not seen in aperture synthesis maps as emission is weak and possibly extended.

Emission from the rotational transitions of ^{13}CO and $C^{18}O$ (1$\rightarrow$0) reveal a ridge of gas near P2 elongated at PA 140°. Single dish observations of outflowing gas suggest there may be a second source 20″ north and 20″ east of Elias 1-12 (Evans *et al.* 1994), possibly embedded in the ridge. However, the complicated emission pattern seen in single dish maps arises from the juxtaposition of red and blueshifted emission from the swept-up shell walls and not from the outflow lobes of a second driving source. Therefore, the ridge is probably either gas swept-up by the wind from Elias 1-12 or a clump in the ambient cloud. Since emission is present over a large velocity range from +3.56 to +6.62 km s^{-1} and exhibits complex kinematics, the ridge is probably swept-up gas rather than an ambient clump. The minimum ridge mass, calculated from the integrated $C^{18}O$ flux density of 1.0 Jy km s^{-1} assuming optically thin emission, is $\geq$0.21 $M_{\odot}$. If distributed over the region between the ridge and the FUor the average density would be $\geq 2 \times 10^3$ cm^{-3}, consistent with observations of dense molecular clouds. Therefore, the ridge is probably a shell of gas within the cavity, swept-up by the wind from Elias 1-12.

The cavity and ridge morphology seen towards Elias 1-12 is similar to that seen toward the FUors RNO 1B/C where consecutive FUor outbursts have swept-up shells of molecular gas (McMuldroch *et al.* 1995). Outflow models also suggest that cavities are formed by a bowshock resulting from internal working surface in a

time-dependent collimated jet (Raga & Cabrit 1993). Cavities are then "refilled" by the turbulent wake of the bowshock on typical timescales of $\sim 10^3$ to 10^4 years. For an opening angle for the Elias 1-12 outflow of 60°, the system inclination is ~70°. The dynamical age of the swept-up ridge is therefore 1.3×10^4 years. The cavity therefore had sufficient time to be refilled before a new outburst swept-up gas to form the ridge. The outflow structure associated with Elias 1-12 may therefore be caused by multiple FUor outbursts.

In Figure 5.7, contours delineate redshifted CO emission, previously presented in Figures 5.4 (b) and 5.6, while the greyscale image traces the velocity gradient. Heavier shading corresponds to emission at higher redshifts. Emission from the cavity walls arises from highly redshifted gas at positions west of P2 and the swept-up ridge; to the east gas is at much lower redshifts. This suggests that the outburst which formed the ridge is altering the general morphology and kinematics of the cavity. This may explain that although blueshifted gas is evident east of the ridge, none is detected to the west.

The mass loss during the outburst can be derived from the momentum of swept up material assuming a velocity for the driving wind. Since the interferometer resolves out extended flux, estimates are minimum values. The mass of the cavity walls and ridge can be calculated from the integrated CO and $C^{18}O$ emission using Equations 1.1 and 5.1. Assuming optically thin emission and adopting an excitation temperature for the outflow of T_{ex}=10 K, the mass of swept up gas in the ridge and walls is 0.21 and 0.02 $M_\odot$ respectively. Using flux weighted average velocities of 0.2 and 9 km s^{-1} from the systemic value, the relative momenta are 0.04 and 0.18 $M_\odot$ km s^{-1}. The high velocity cavity walls therefore dominate the total momentum. The total mass loss during the outburst, assuming a wind velocity of 615 km s^{-1} (Bastian & Mundt 1985), is $\geq 4 \times 10^{-4}$ $M_\odot$. For a typical outburst lasting 100 years, the mass loss rate

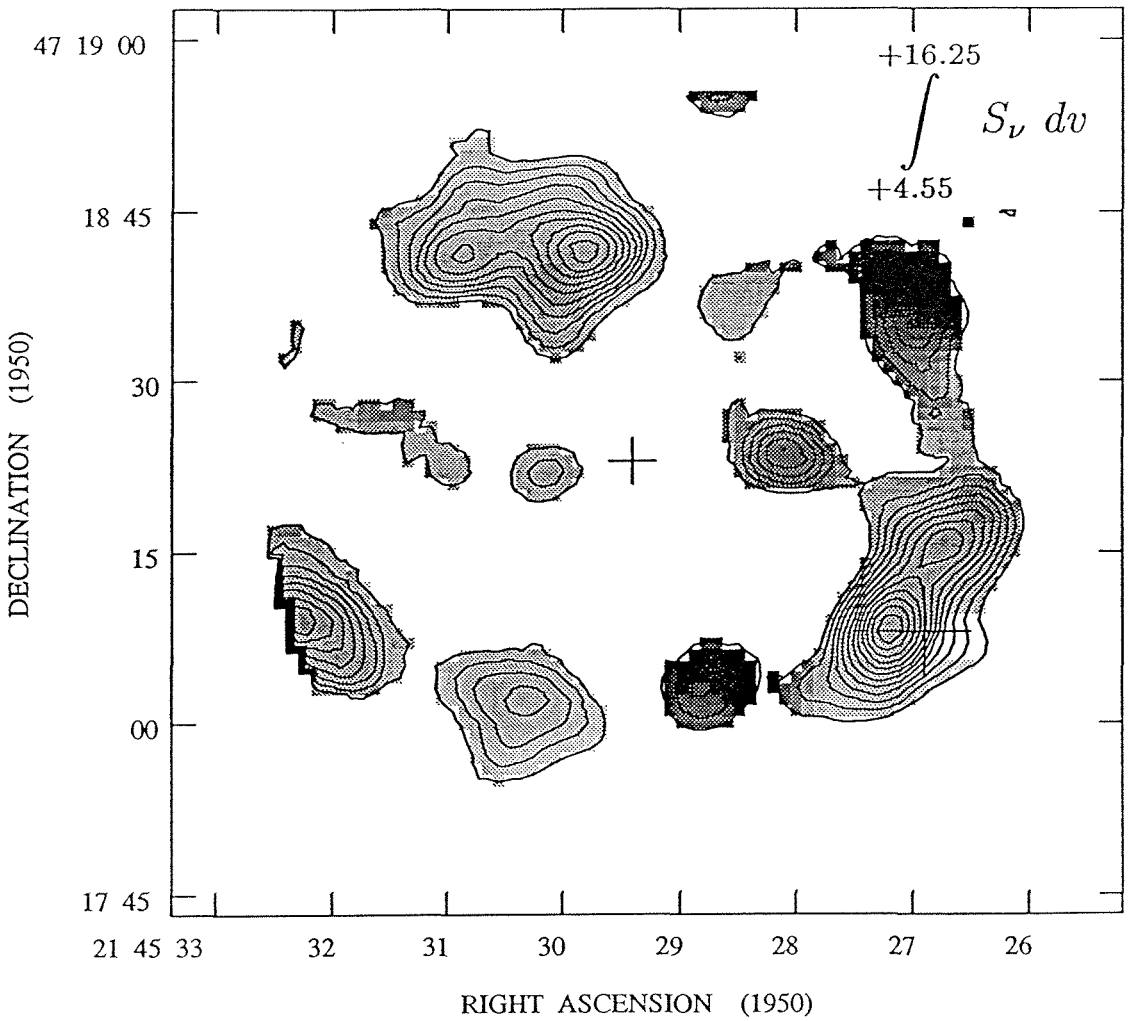

Figure 5.7. *Contours delineate CO (1→0) emission integrated over the velocity range* +4.55 to 16.25 km s^{-1}, previously presented in Figures 5.4 (b) and 5.6. The greyscale image traces the velocity gradient. Heavier shading corresponds to emission at higher redshifted velocities.

would be $\geq 4 \times 10^{-6}\ M_{\odot}\ \mathrm{yr}^{-1}$, consistent with observations of FUor winds.

5. Conclusions

High resolution aperture synthesis observations of the FU Orionis object Elias 1-12 reveal a dense envelope of molecular gas, mass 0.36 $M_{\odot}$, possibly in rotation about the star. Fractional chemical abundances, calculated from an LTE code, suggest that HCN and H_2CO are depleted onto grains. By comparison CH_3OH is slightly enhanced, possibly by low velocity grain-grain collisions in the outflow.

Observations of CO (1→0) emission trace the walls of a redshifted parabolic outflow cavity, PA~45°, lying nearly in the plane of the sky with Elias 1-12 at the apex. Aperture synthesis maps of ^{13}CO and $C^{18}O$ (1→0) emission show a dense ridge within the cavity. The morphology and kinematics of the cavity and ridge are consistent with formation by a time-dependent outflow; cavity walls are possibly comprised of gas swept-up by several FU Orionis outbursts with the ridge being formed by an eruption 1.3×10^4 years ago. The weak blueshifted outflow to the southwest of Elias 1-12 (Evans *et al.* 1994) is not seen in the interferometer maps. No evidence is seen of the possible second source proposed by Evans *et al.* (1994).

CHAPTER 6

The Circumstellar Environment of the FU Orionis Object V1515 Cygni

1. Introduction

The FUor V1515 Cygni is located near the reflection nebulosity NGC 6914, some 1050 pc distant (Racine 1968; Herbig 1977). Although the star displays many typical FUor spectral characteristics, its light curve is unique with the rise to maximum light in 1975 taking decades rather than years. This slower rise time is well modelled by thermal instability models (Bell & Lin 1994). The light curve also shows a strong minimum in 1980 lasting several years, possibly the result of dust condensing in the outflow (Kenyon *et al.* 1991). V1515 Cygni possesses a large infrared excess which, once corrected for the optical extinction of A_v=2.8^m, can be fit as far as 10 μm with standard accretion disk models (Kenyon *et al.* 1988; Kenyon & Hartmann 1991). Beyond this, an infalling dusty envelope is needed to explain the additional flux (Kenyon & Hartmann 1991). Linear polarization measurements at optical wavelengths suggest the envelope is elongated at PA 30°., while the low vsini$\sim$20 km s^{-1} suggests the system is inclined nearly pole-on (Bastien 1982; Kenyon *et al.* 1991; Whitney & Hartmann 1993). Far infrared and submillimeter observations suggest the circumstellar disk is of mass $6 \times 10^{-4} \leq M \leq 7 \times 10^{-2}$ with an emissivity index $\beta \sim 2$. Observations of molecular line emission at millimeter wavelengths reveal double peaked structure in both the CO (3$\rightarrow$2) and ^{13}CO (2$\rightarrow$1) line transitions, the possible result of self-absorption in the line core (Evans *et al.* 1994). Strong wing emission is also apparent indicative of molecular gas swept up by the wind seen at optical wavelengths (Crosswell *et al.* 1987; Evans *et al.* 1994).

2. Observations

2.1 CSO Observations

Observations of V1515 Cygni were acquired with the Caltech Submillimeter Observatory (CSO) on Mauna Kea, Hawaii, in 1991 July. The facility 230 GHz and 345 GHz receivers were used in conjunction with the CSO 500 and 50 MHz bandwidth acousto-optical spectrometers (Ellison & Miller 1987; Ellison *et al.* 1989). Position switching to a reference position 30′ to the west produced the least contaminated spectra. All temperatures quoted have been corrected for the main beam efficiencies of 0.52 and 0.58 at 230 and 345 GHz respectively. For further information concerning the observational technique see Chapter 2.

Although several molecular species were searched for in the 230 GHz band towards V1515 Cygni, only the J=2→1 transitions of CO and its isotopes were detected to a 3σ rms noise limit of 0.5 K. In the 345 GHz band, CO (3→2) line emission was detected towards the FUor.

2.2 OVRO Observations

Aperture synthesis mapping of the rotational transitions of ^{12}CO (1→0), ^{13}CO (1→0), and C^{18}O. (1→0) at ν=115.271, 110.201, and 109.782 GHz respectively, was carried out using the Owens Valley millimeter-wave interferometer between 1993, September and 1993, November. System temperatures were typically 650 and 320 K (SSB) at 115 and 110 GHz respectively. The OVRO digital correlator provided velocity resolutions of 0.33 and 1.30 km s^{-1} at 115 GHz and 0.34 km s^{-1} at 110 GHz. For both sets of observations, simultaneous continuum observations were obtained in a broadband channel of effective width 1 GHz, centered on the systemic velocity of the star, v_{LSR} = 5.7 km s^{-1} (Evans *et al.* 1994).

Phases and amplitudes were calibrated by observing the quasar BL Lac at 25 minute intervals. The absolute flux scale was established by measurements of Uranus.

Maps were generated from calibrated visibility data using the NRAO AIPS software package. Maximum unprojected baselines of 60 m north-south and 60 m east-west gave uniformly weighted synthesized beams of 6″.3 ×5″.2, PA −86° at 115 GHz and 6″.0 ×5″.1, PA 85° at 110 GHz. For these beams and frequencies, $T_B = 1$ K corresponds to 0.33 Jy/beam. The phase center of the maps is α (1950) = $20^h\ 22^m\ 03.2^s$, δ (1950) = +42° 02′ 39″.0, the position of V1515 Cygni given by Herbig & Bell (1988). Positional accuracy is ± 2″.

3. Results

3.1 CSO Results

Emission from V1515 Cygni was detected in four molecular transitions at the CSO, namely those of CO (3→2), CO (2→1), ^{13}CO (2→1), and C^{18}O (2→1). Line profiles are displayed in Figure 6.1. A double peaked profile is present in all transitions. The CO (2→1) peak brightness temperature, T_{MB}=10.1 K occurs at +7.26 km s^{-1} with a smaller peak at +11.93 km s^{-1}. The CO (3→2) spectrum is similar, albeit weaker, with peaks at +6.74 and +11.94 km s^{-1}. By contrast, ^{13}CO and C^{18}O (2→1) emission maxima occur at the smaller velocities of +5.1 and +5.2 km s^{-1}, with secondary peaks at +11.2 km s^{-1}. Relative line strengths suggest that ^{13}CO and C^{18}O peak emission at +5 km s^{-1} is optically thin with τ ~0.8 and 0.1 respectively. These optically thin transitions best trace the gas kinematics towards V1515 Cygni and imply that the double peaked line profile arises due to emission from gas at two distinct velocities rather than the result of self-absorption. The velocities of the primary and secondary velocity components are therefore +5.1 and +11.2 km s^{-1} respectively. Indeed, there is a dip at +5.4 km s^{-1} in the CO (2→1) emission possibly from self-absorption.

All four transitions show wing emission for the component at +5.1 km s^{-1}. Both the CO (2→1) and (3→2) transitions possess strong blue and weak redshifted wings; ^{13}CO and C^{18}O (2→1) emission show only a weak blueshifted wing. Comparison of CO and C^{18}O spectra suggests wing emission extends from +0.5 to +4.0 km s^{-1} and +7.0 to +8.5 km s^{-1}. In contrast, the smaller peak at +11.2 km s^{-1} shows no evidence for wing emission. Relative line intensities suggest this peak is more optically thin with $\tau_{^{13}CO}$ ~0.04 and only a tentative detection at C^{18}O.

3.2 OVRO Results

Dust continuum emission from V1515 Cygni was not detected at 2.7 mm to a

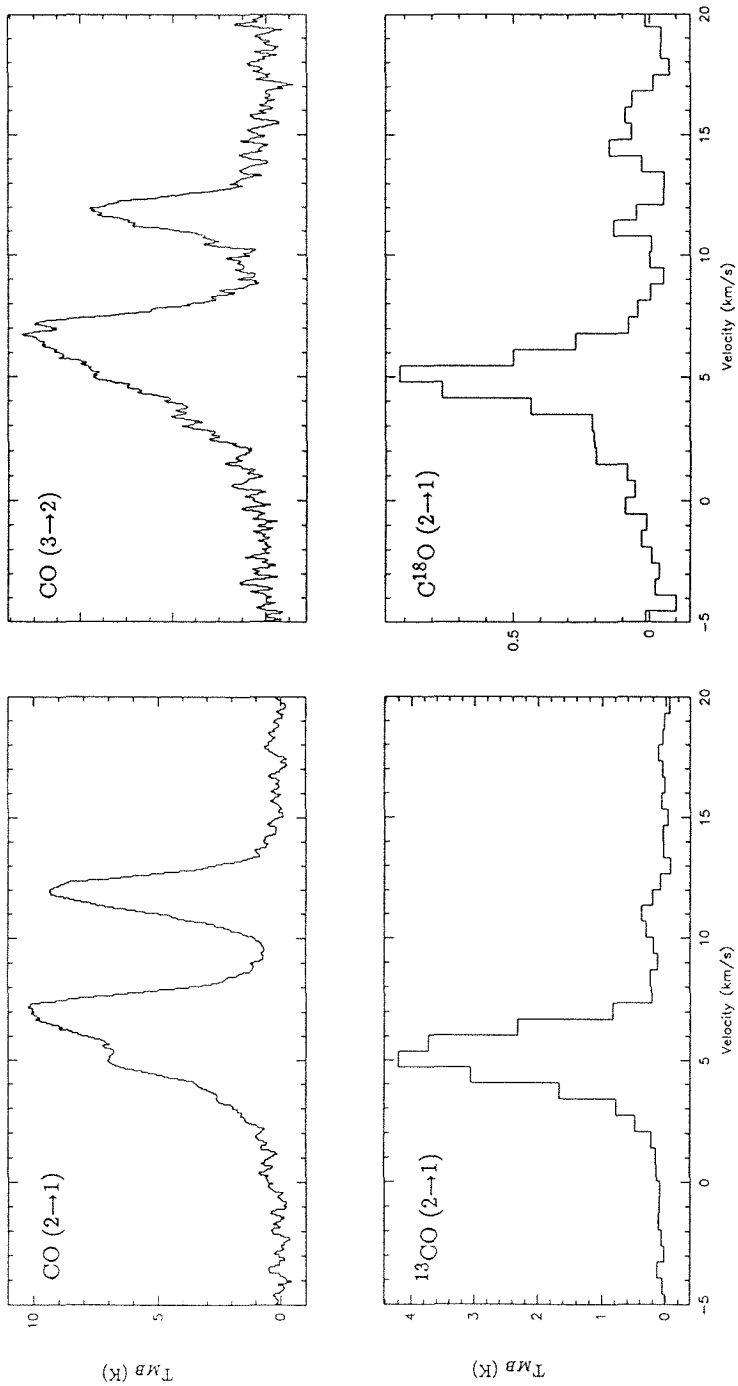

Figure 6.1. Line emission in CO (2→ 1), CO (3→2), ^{13}CO (2→1), and C^{18}O (2→1) as detected at the CSO. Temperatures have been corrected for main beam efficiencies.

3σ limit of 4 mJy/beam, consistent with extrapolations from measurements taken at shorter wavelengths (Weintraub *et al.* 1991). By comparison, molecular gas emission was detected in all three species.

Emission from the rotational transition of $C^{18}O$ (1→0) is unresolved in the 6″.36 × 5″.34 (6700 × 5600 SU), PA 86° beam. The peak of 0.43 Jy/beam occurs at a velocity of +4.66 km s^{-1} and lies at α (1950) = 20^h 22^m 03.649^s, δ (1950) = +42° 02′ 39″.0., approximately 5″ east of the nominal stellar position. No $C^{18}O$ emission was detected outside of the velocity range +4.49 to +4.83 km s^{-1} to a 3σ limit of 0.27 Jy/beam.

The ^{13}CO (1→0) emission peak of 0.7 Jy/beam at 4.32 km s^{-1} is, within the positional uncertainties, coincident with the $C^{18}O$ maximum. Comparison of $C^{18}O$ and ^{13}CO line strengths suggests the $C^{18}O$ emission is optically thin with $\tau_{C^{18}O}$ ~0.6. $C^{18}O$ emission is therefore an accurate tracer of column density. Since V1515 Cygni is only moderately embedded, emission probably arises from high density gas in the immediate vicinity of the star, rather than from swept-up material. The $C^{18}O$ emission peak probably marks the true stellar position. Optical measurements may be in error due to even the moderate amount of extinction towards V1515 Cygni. The total mass surrounding V1515 Cygni can be calculated from the $C^{18}O$ integrated flux density of 0.15 Jy km s^{-1} using Equation 5.1. Adopting an abundance ratio of $C^{18}O/H_2 = 2 \times 10^{-7}$ (Chackerian & Tipping 1983), an excitation temperature of 20 K, and an optical depth $\tau_{C^{18}O}$=0.6, the mass surrounding the FUor is 0.09 $M_\odot$.

Figure 6.2 shows the individual channel maps, with a velocity resolution 1.3 km s^{-1}, of the CO (1→0) emission toward V1515 Cygni. No emission is evident outside of these velocities to a 3σ limit of 0.45 Jy/beam. At velocities between +2.40 and +3.70 km s^{-1}, blueshifted with respect to the primary velocity component, emission is concentrated to north and east of the star. Maps with a higher velocity

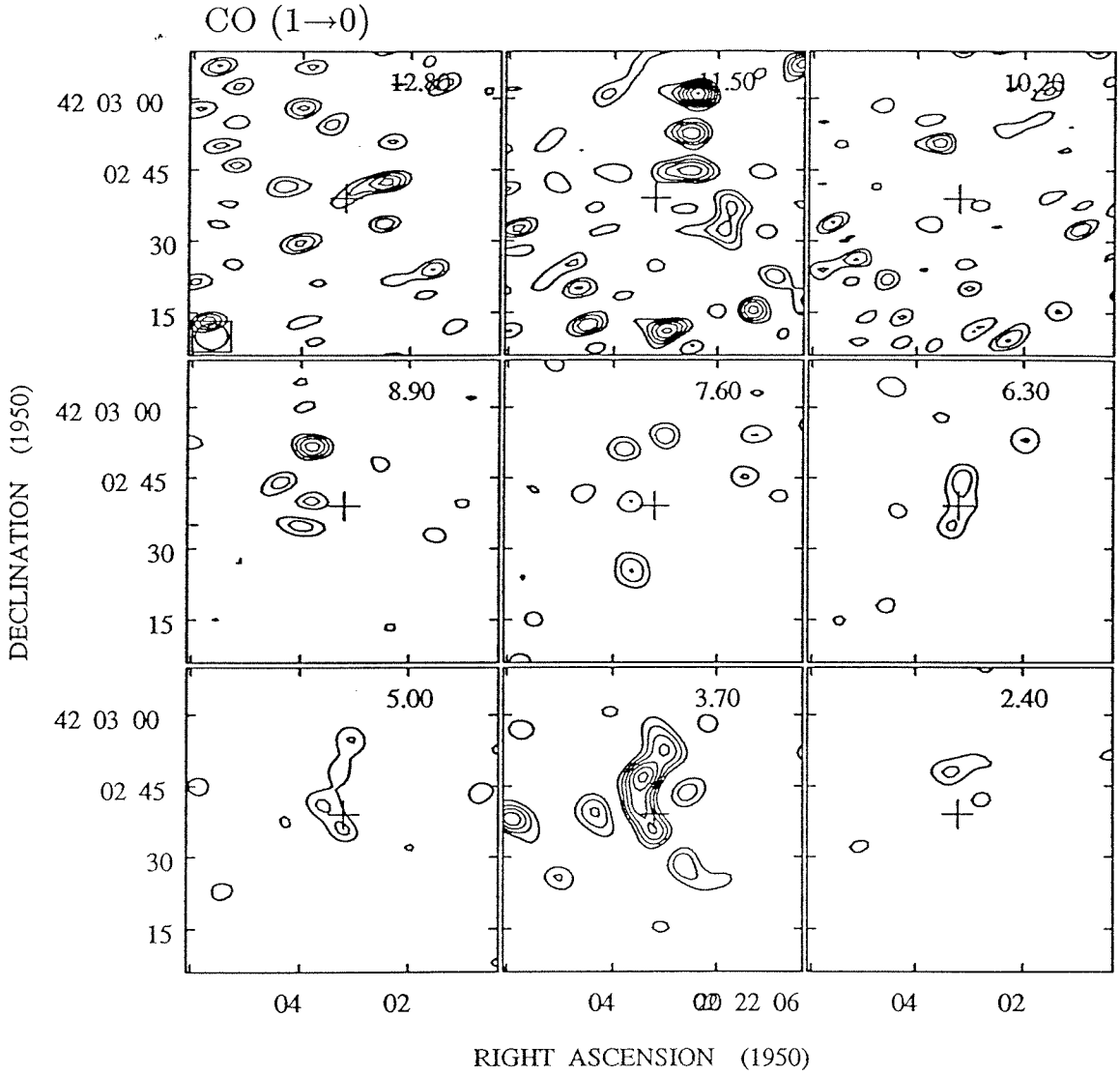

Figure 6.2. Aperture synthesis maps of CO (1→0) emission with a velocity resolution of 1.3 km s^{-1}. Contours begin at 2σ and are spaced by 1σ, 0.12 Jy/beam. A cross 6″ in size marks the optical position of V1515 Cygni.

resolution show a maximum of 1.65 Jy/beam at +3.37 km s^{-1}. At redshifted velocities between +5.00 and +6.30 km s^{-1}, the emission pattern is similar but weaker. No coherent emission structure is discernable between +7.60 and +12.80 km s^{-1}. Between +10.20 and +12.80 km s^{-1}, the range of velocities associated with the secondary component, the noise level is higher probably while emission appears "clumpy", characteristic of an extended component being resolved out.

Figure 6.3 shows CO and ^{13}CO emission integrated over the velocity ranges +1.75 to +6.95 km s^{-1} and +4.49 to +4.83 km s^{-1} respectively. No ^{13}CO emission was detected outside of these velocities to a 3σ limit of 0.36 Jy/beam. The ^{13}CO morphology is roughly comparable to that seen at CO (1→0) although emission is present over a more narrow range of velocities. Comparison of relative line strengths yields an optical depth $\tau_{^{13}CO} \geq 1$. Using Equation 2.1, the mass of molecular gas calculated from the ^{13}CO integrated flux density of 1.23 Jy km s^{-1} is 0.06 $M_{\odot}$. Here, the kinetic temperature is assumed to be 10 K and the optical depth is $\tau_{^{13}CO}=1$.

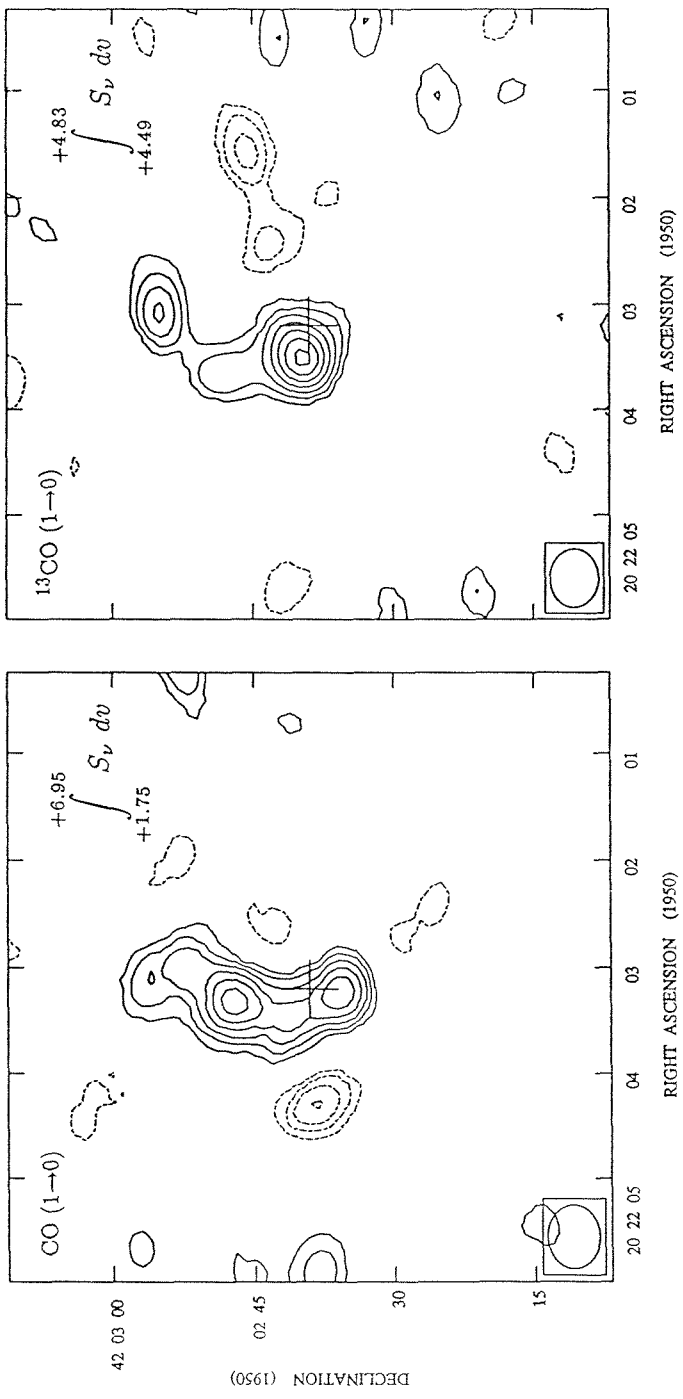

Figure 6.3. Aperture synthesis maps of CO (1→0) and ^{13}CO (1→0) emission integrated over velocities +1.75 to +6.95 km s^{-1} and +4.49 to +4.83 km s^{-1}. The rms noise level is 0.3 Jy/beam km s^{-1} and 0.5 Jy/beam km s^{-1}. Contours in each map begin at 2σ and are spaced by 1σ.

4. Discussion and Summary

Single dish molecular line observations of V1515 Cygni, displayed in Figure 6.1, show a double peaked profile with the primary and secondary a components centered at 5.1 and 11.2 km s^{-1} respectively. The primary component possesses both red and blueshifted outflow wings indicative of a driving source. In contrast, the secondary component shows no sign of outflowing gas. In aperture synthesis maps, the secondary component near 11.2 km s^{-1} is resolved out. Emission from the secondary component probably arises from a molecular cloud in the line of sight.

Near 5.1 km s^{-1}, emission from the CO, ^{13}CO, and $C^{18}O$ (1→0) rotational transitions is concentrated near the stellar position. Maps of unresolved $C^{18}O$ emission suggest the star lies 5″ east of the nominal stellar position and is surrounded by 0.09 $M_{\odot}$ of molecular gas. If this mass is distributed spherically, the implied extinction of $A_v \geq 2.9^m$ is marginally consistent with the observed value $A_v = 2.8^m$. There is no sign of a massive disk-like structure as seen around other FUors and pre-outburst candidates (Chapters 2, 4, & 5). Observations at higher spatial resolution and sensitivity are needed to constrain the gas distribution further.

^{13}CO emission, shown in Figure 6.3, peaks at the star and extends ~15″ to the northwest. CO morphology is similar but is dominated by emission at +3.34 km s^{-1}, blueshifted relative to the peak ^{13}CO and $C^{18}O$ emission. At these velocities, emission probably arises from outflowing gas. Comparison with r-band optical images suggests the molecular line emission traces the arc of the reflection nebulosity (Goodrich 1987). Low vsini measurements and low visual extinction estimates suggest the V1515 Cygni is inclined more pole-on. The morphology of the CO maps and optical images is consistent outflow cavity viewed pole-on. However, more sensitive maps with higher spatial resolution are needed to discriminate between circumstellar and swept-up outflowing gas.

CHAPTER 7

The Circumstellar Environment of FU Orionis

1. Introduction

FU Orionis, the namesake of the FUor class, is located within an arc-like reflection nebula in the B35 dark cloud some 550 pc distant (Herbig 1966, 1977). In 1939, FU Orionis rose in brightness by 6^m over several months, subsequently faded slightly two years later, and has been slowly oscillating since then. Although the star has been relatively quiescent photometrically, shell lines associated with outflowing material show variability over timescales of days. Standard FUor disk models suggest a system inclination of $25° \leq i \leq 70°$ and yield a mass accretion rate $\dot{M} \sim 10^{-4}$ $M_\odot$ yr^{-1} (Kenyon *et al.* 1988). Models of near infrared emission suggest that circumstellar material is distributed in a flared disk or a flattened envelope, consistent with the low optical extinction of A_v=2.9 (Cohen & Kuhi 1979). Linear polarization measurements yield an equatorial position angle of 130° suggesting the envelope is elongated along this direction (Bastien 1982; Whitney & Hartmann 1993). Observations of thermal dust emission at submillimeter and millimeter wavelengths suggest a circumstellar disk mass of $\sim$0.01 $M_\odot$ and emissivity index $\beta \sim 1$ (Weintraub *et al.* 1991). Molecular line emission seen in the CO (1$\rightarrow$0) and (3$\rightarrow$2) transitions is centered at V_{LSR} $\sim$12.0 km s^{-1} but shows no evidence of a molecular outflow (Edwards & Snell 1982; Levreault 1988; Evans *et al.* 1994). Indeed, although optical lines exhibit strong P Cygni profiles, observations at millimeter and radio wavelengths show no evidence of energetic mass loss.

2. Observations

2.1 CSO Observations

Single dish observations in the 345 GHz band were carried out at the Caltech Submillimeter Observatory (CSO) on Mauna Kea, Hawaii, in 1991 January. Spectra were acquired for CO (3→2) and ^{13}CO (3→ 2). Temperatures have been corrected for the main beam efficiency of 0.58, calculated from measurements of Jupiter. Position switching to a reference position at $\alpha = 05^h\ 43^m\ 15^s$, $\delta = +09°\ 10'\ 00''$ produced the least contaminated spectra. For further details of the observational technique consult Chapter 2.

2.2 OVRO Observations

Aperture synthesis mapping of the rotational transitions of CO (1→0) and ^{13}CO (2→1) at ν=220.399 and 115.271 GHz, was carried out with the Owens valley millimeter wave interferometer between 1991 January to April, and 1992 December to May respectively. System temperatures were typically 1100 K (SSB) at 220 GHz and 1300 K (SSB) at 115 GHz. At 220 GHz two filter banks, 32 × 1 MHz and 32 × 50 kHz, each centered on the CO velocity in the direction of the star, v_{LSR} = 12.0 km s^{-1} (Edwards & Snell 1982), provided velocity resolutions of 1.3 and 0.07 km s^{-1} At 115 GHz, the OVRO digital correlator provided velocity resolutions of 1.3 and 0.33 km s^{-1}. For both sets of observations, simultaneous continuum observations were obtained in a broadband channel of effective width 375 MHz, centered on the systemic velocity.

The phase and amplitude gains were calibrated by observing the quasar 0529+075 at 25 minute intervals, and the absolute flux scale was established by measurements of Neptune and Uranus. Maps were generated from calibrated visibility data using the NRAO AIPS software package. Positional accuracy is ± 2″. At 220 GHz, maximum unprojected baselines of 80 m north-south and east-west gave naturally

weighted synthesized beams of $4''.0 \times 3''.1$, PA 29°. At 115 GHz, maximum baselines of 80 m north-south and 115 m east-west resulted in a naturally weighted beam of $25''.1 \times 5''.0$, PA 143°. Since FU Orionis is located near the celestial equator, north-south baselines are strongly foreshortened yielding large beams. The phase center of the maps is α (1950) = $05^h\ 42^m\ 37.97^s$, δ (1950) = +09° 03′ 02″.5, the position of FU Orionis given by Herbig & Bell (1988).

3. Results

3.1 CSO Results

Line profiles of the CO (3→ 2) and ^{13}CO (3→2) emission towards FU Orionis are displayed in Figure 7.1. The peak CO (3→2) emission of 5.6 K occurs at 12.1 km s^{-1} while the ^{13}CO (3→2) emission peak of 3.7 K lies at 11.4 km s^{-1}. Relative line intensities suggest that CO and probably ^{13}CO are optically thick. The line width of CO (3→2) emission toward the star decreases from 2.5 km s^{-1} to 1.7 km s^{-1} one beam width (~20″) away. However, there is no evidence for wing emission indicative of outflowing molecular gas.

3.2 OVRO Results

Dust continuum emission from FU Orionis was not detected at either 2.6 or 1.3 mm to 3σ limits of 30 and 66 mJy/beam respectively, consistent with single telescope measurements (Weintraub *et al.* 1991). In contrast, unresolved molecular emission was detected in both CO (1→0) and ^{13}CO (2→1) transitions with beams 25″.1 × 5″.0 (13750 × 2750 AU), PA 143°, and 4″.1 × 3″.2. (2255 × 1760 AU), PA 29°. Both emission peaks lie, within the positional uncertainties, at the stellar position. No flux was detected outside of the velocity ranges +8.05 to +13.3 km s^{-1} and +10.64 to +12.0 km s^{-1} to 3σ limits of 0.69 and 0.75 Jy/beam respectively.

The mass of H_2 surrounding FU Orionis can be calculated from the CO (1→0) and ^{13}CO (2→1) integrated flux densities of 6.3 and 1.4 Jy using Equations 2.1 and 2.3. Assuming emission is optically thin and adopting an excitation temperature of 10 K and abundances of X(CO)=10^{-4} and X(^{13}CO)=1.7 × 10^{-6} (Chackerian & Tipping 1983; Langer & Penzias 1993), lower limits to the H_2 mass surrounding FU Orionis are 10^{-3} and 2 × 10^{-3} $M_\odot$ respectively.

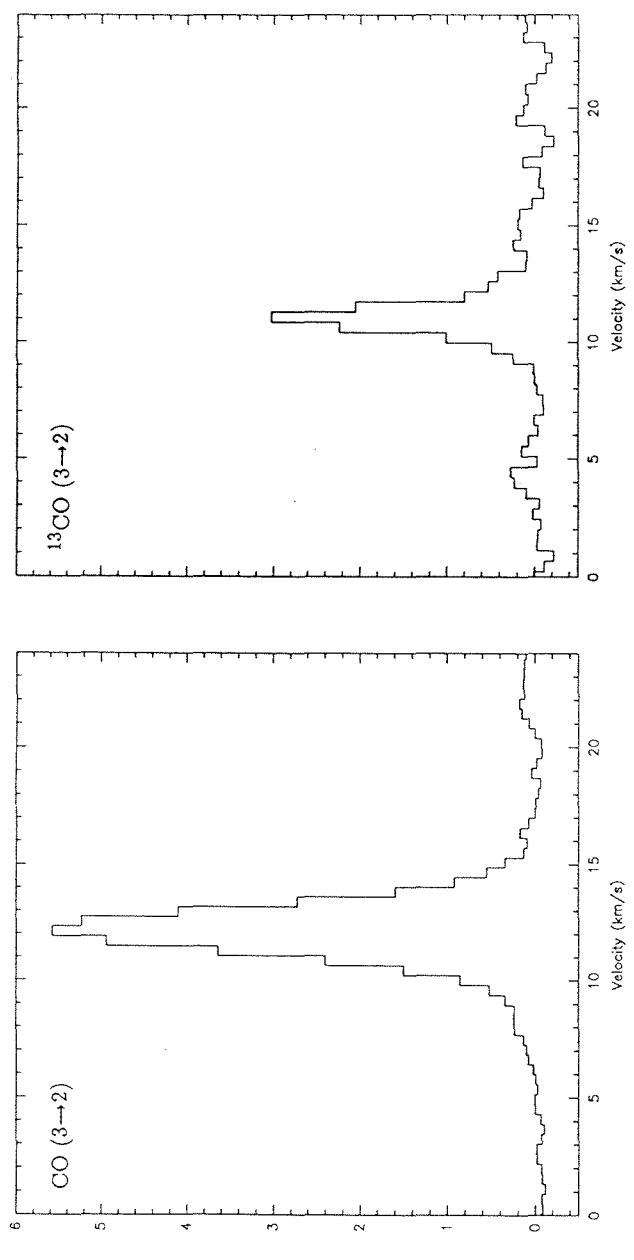

Figure 7.1. Line profiles of the CO (3→ 2) and ^{13}CO (3→2) emission towards FU Orionis as detected at the CSO. Temperatures have been corrected for main beam efficiencies.

4. Discussion

FU Orionis is surrounded by a molecular gas envelope or disk, $\lesssim$2000 AU in size, mass $\geq 2 \times 10^{-3}$ $M_{\odot}$. At the present spatial resolution we are unable to characterize the gas dynamics. No evidence is seen of outflowing molecular gas or of emission further from the star. Estimates of the virial mass from ^{13}CO (2$\rightarrow$1) observations yield 0.2 $M_{\odot}$

Comparison with other FUors and pre-outburst objects reveals that FU Orionis is relatively deficient in circumstellar material. The paucity of swept-up molecular gas together with the low envelope mass suggests there is little available material surrounding FU Orionis for accretion. Indeed, the envelope mass of 2×10^{-3} $M_{\odot}$ is comparable to estimates of the mass accreted onto the star during one FUor outburst i.e. $\sim 10^{-4}$ $M_{\odot}$. This suggests that FU Orionis is possibly near the end of the FUor stage and is dominated by the less energetic T Tauri phase between outbursts.

CHAPTER 8

Discussion

An idealised schematic of an FU Orionis object, derived from the observational characterization of such systems, is shown in Figure 8.1. Each of the individual components in the diagram are described below in detail along with how the present images shed new light on the FU Orionis phenomenon. Table 8.1 summarizes the results of the OVRO and CSO observations for the six FUors and one pre-outburst candidate discussed earlier.

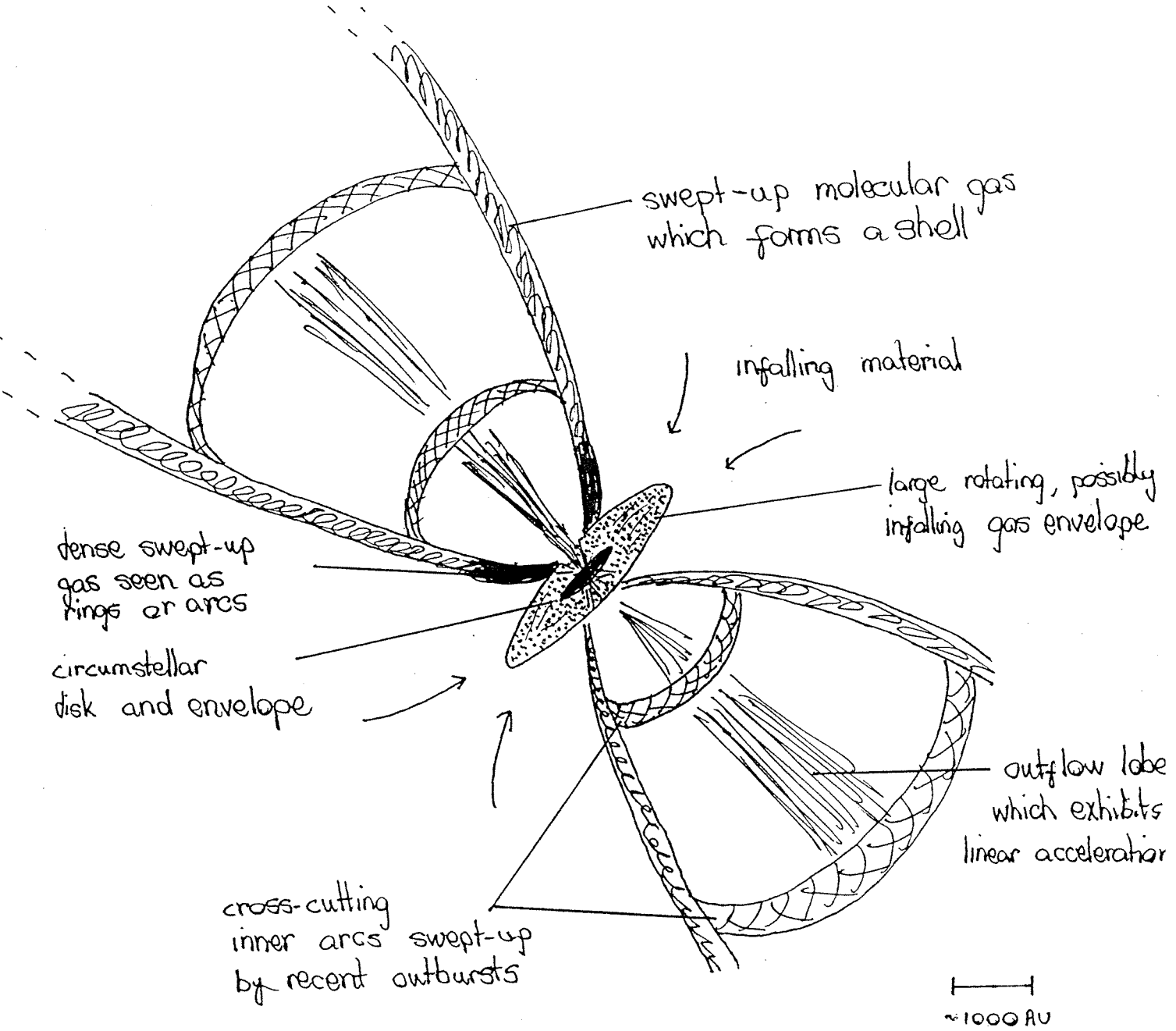

Figure 8.1. Schematic diagram of an FU Orionis object. The star is embedded in a circumstellar disk and a larger dusty envelope, which are in turn surrounded by a extended molecular gas envelope several thousand AU in size. Further from the star, molecular gas swept-up by several outbursts has formed an outflow shell. The most recent outbursts have swept-up molecular gas creating cross-cutting inner arcs.

(1) Source	(2) Disk/envelope $M_\odot$	(3) Gas envelope $M_\odot$	(4) Gas envelope AU	(5) Outflow
V1331 Cygni	0.5±.15	≥0.32	6000 × 4400	ring+bipolar
RNO 1B/1C	≥1.1	–	–	shell
V1057 Cygni	≥0.09	≥0.20	7500 × 4700	arc+bipolar
Elias 1-12	–	≥0.36	8200 × 4600	shell
V1515 Cygni	–	≥0.09	≤6700 × 5600	arc
FU Orionis	–	≥2(-3)	≤2000	none
L1551	0.07	0.28	2300 × 1600	shell

Table 8.1. Table of sample sources. The FUor L1551 is also listed for comparison (Snell 1987; Moriarty-Schieven *et al.* 1987; Uchida *et al.* 1987; Ohashi *et al.* 1994).

1. Circumstellar Dust

Column 2 in Table 8.1 lists the mass of gas derived from measurements of their dust emission. Also included for reference is the FUor L1551. Millimeter continuum emission is seen toward only three of the seven sample sources; their large distances of 550-1050 pc, compared to 140 pc to the Taurus-Auriga cloud, make detections at millimeter wavelengths difficult. No evidence is seen of any FUor companions on ~1000 AU scales. Emission from V1331 Cygni and V1057 Cygni is unresolved in the 3″ and 2″ beams. Dust emission is probably dominated by the disk at 2.7 mm and by the envelope at 1.3 mm (*cf* Tereby *et al.* 1993). Emission around RNO 1C is resolved revealing a flattened duty envelope ~5000 AU in size. The small number of detected sources precludes a meaningful comparison of FUor disk masses with those of disks around T Tauri stars. However, single dish studies at shorter wavelengths suggest that FUor disk masses are comparable.

2. Extended Molecular Gas Envelopes

Large extended molecular gas envelopes exist around V1331 Cygni, V1057 Cygni, and Elias 1-12. Unresolved molecular gas emission, probably also from similar circumstellar envelopes, are associated with FU Orionis and V1515 Cygni. Table 8.1 lists the size and mass of the envelopes. No distinct molecular gas envelope is seen around the FUors RNO 1B/1C. Since these FUors are very embedded, observations in more optically thin transitions are needed to delineate any envelope or disk-like structure.

Aperture synthesis maps reveal the envelopes to be asymmetrically distributed. Calculations of the column density yield optical extinctions higher than the observed values. These facts suggest that gas is either distributed in a disk-like structure or that material is evacuated from around the stellar poles by the strong FUor wind. For Elias 1-12, a system inclined nearly in the plane of the sky, the effect of the outflow evacuation should be minimal. The low observed extinction therefore results from gas lying in a flattened envelope. Other FUors probably possess similar disk-like morphologies. Such structures, several thousand AU in size, are predicted by the models of Galli & Shu (1994) and Stahler *et al.* (1994). The former models include the effects of magnetic fields where pinching forces deflect infalling gas into a pseudodisk. With the latter models, gas infalling on parabolic trajectories has its z-component of velocity cancelled by collisions with other infalling gas, thereby creating a gas disk.

Infalling gas in an elongated envelope has a similar kinematic signature to gas in a bipolar outflow. Envelope densities are probably more dense than all but the highest opacity regions of the outflow. Observations of very optically thin transitions can therefore delineate the dense circumstellar material while remaining unaffected by outflowing gas. Observations of V1057 Cygni and Elias 1-12 possibly reveal infalling and rotating gas. Models of emission from smaller molecular disks surrounding T

Tauri stars clearly delineate the infalling and rotating velocity components (Koerner 1994). Since FUors lie at greater distances, the current aperture synthesis maps lack the spatial resolution required for such modeling.

3. Outflowing Gas

All sources except FU Orionis possess spectra with wing emission indicative of outflowing molecular gas. High spatial resolution aperture synthesis maps suggest the observed outflow structure is very dependent on viewing geometry and optical depth effects. Sources seen more pole-on, such as V1331 Cygni, V1515 Cygni, and V1057 Cygni, show ring or arc-like molecular line emission whose morphology resembles the associated reflection nebulosity. V1331 Cygni and V1057 Cygni also possess poorly collimated bipolar outflows. More inclined FUors, such as RNO 1B/1C and Elias 1-12, show a shell-like emission structure with cross cutting inner walls. Taken together, the emission pattern is most consistent with swept-up shells of gas being viewed at different angles.

These new aperture synthesis observations suggest FUors are frequently associated with shell-like structures. Early studies of the outflow associated with the FUor L1551 suggested that the emission pattern traces an empty expanding bubble with molecular line emission arising in the expanding shell (Snell 1987; Moriarty-Schieven *et al.* 1987; Uchida *et al.* 1987). Such *hollow* shell models present major difficulties (*cf* Bachiller & Gómez-González 1992). Observations of L1551 and the sample sources studied here are more consistent with outflows being driven by a highly collimated jet that forms a *filled* shell structure (Masson & Chernin 1993; Raga & Cabrit 1993; Stahler 1994).

Time-dependent outflow models invoke a jet with a variable wind velocity; internal working surfaces propagate along the jet creating multiple bowshocks which entrain gas to form shells (Raga & Cabrit 1993). The turbulence in the wake of the bowshock causes the cavity to be refilled on timescales of several thousand years. If the time between energetic outflow episodes is longer than this, each new outflow event will form a shell within the pre-existing one. For FUors, with a repetition timescale

of $\sim 10^4$ years, consecutive outbursts would indeed form "shells within shells." These models can therefore reproduce the emission patterns seen in L1551, RNO 1B/1C and Elias 1-12. However the relevance of these models is uncertain since they possess a time-dependent wind velocity not mass loss rate as is observed for FUors. Since shell-like structure is frequently associated with FUors, new outflow models are needed that include variable mass loss rates.

No extremely high velocity molecular emission is detected toward any of the sample sources. Although FUors possess powerful winds, no molecular gas is swept up to high velocities to form the "bullets" seen in other sources (*cf* Bachiller & Gómez-González; Guilloteau *et al.* 1992). FUor outflows may often lack the collimation needed to produce high velocity bullets. This is consistent with outflow surveys which suggest that more energetic sources are less collimated (Levreault 1988).

Comparison of columns 3 and 5 in Table 8.1 suggests the mass of the molecular gas envelope may be correlated with the strength of the molecular outflow. FU Orionis, which is not associated with outflowing molecular gas, has the lowest mass envelope. V1515 Cygni possesses the second lowest mass envelope; spectra exhibit modest outflow wings while aperture synthesis maps show only small amounts of swept-up molecular gas. The other sources with strong outflows, V1331 Cygni, V1057 Cygni, and Elias 1-12 are associated with large, massive envelopes. However, all FUors possess strong atomic winds that can sweep-up molecular gas. This suggests there is a paucity of molecular material around FU Orionis and V1515 Cygni probably due to excavation by the outflow; less molecular gas is now available to be swept-up while envelope masses are smaller since less material is available for accretion.

4. Chemistry

Molecular line emission from CO (3→2) and ^{13}CO (3→2) was observed at the CSO toward FU Orionis. Emission from CO (3→2), CO (2→1), ^{13}CO (2→1), and C^{18}O (2→1) was detected from all the other sample sources. Relative line ratios suggest that CO is optically thick as is ^{13}CO for most objects. C^{18}O emission is more typically optically thin. Emission from other molecules is also observed toward the more deeply embedded FUors RNO 1B/1C and Elias 1-12 (see Tables 3.1 and 5.1). LVG and LTE radiative transfer codes were used to calculate column densities and fractional abundances from line strengths and widths. Towards RNO 1B/1C, SiO and methanol show enhancements larger than an order of magnitude. The fractional abundance of methanol towards Elias 1-12 is comparable to the TMC 1 core, while HCN and H_2CO are depressed. While small effects may result from density and temperature differences in the gas, such large enrichments and depletions are likely the result of chemical interactions.

Shocks in the outflowing gas can drive new reaction routes even for low luminosity sources. The SiO enrichments detected towards RNO 1B/1C are most likely produced by sputtering or evaporation of dust grains in regions of directly shocked and entrained material. Alternatively, SiH_4 may sublime off grain surfaces to react with OH to form SiO. Shocks cannot be invoked to give the methanol and formaldehyde enhancements as these molecules are easily dissociated. Grain-grain collisions can provide the needed methanol. For RNO 1B/1C, collisions evaporate the methanol rich grain mantles causing enhancements in the gas phase. For Elias 1-12, softer collisions heat the grain mantles to ~140 K changing the amorphous ice into a type II clathrate hydrate. Excess methanol above a 7% abundance is released, while even more volatile substances can be trapped in smaller cage sites up to abundances of 14%. Methanol therefore appears enhanced relative to HCN and H_2CO which are

still depleted onto the grains. Such low velocity collisions probably occur in the shear zones in outflowing gas since infalling gas has more laminar flow. Beam dilution factors are too large to detect chemical enhancements in circumstellar disks due to heating effects caused by FUor outbursts.

5. Implications for FU Orionis Phenomena

Large extended molecular gas envelopes, several thousand AU in size, are detected towards V1331 Cygni, V1057 Cygni and Elias 1-12. Unresolved gas concentrations are seen around FU Orionis and V1515 Cygni. Similar envelopes, are frequently detected around embedded sources. Outflows from embedded sources also show time-dependent structure and shell-like morphologies similar to FUors. This suggests that FUors are transition objects from embedded sources to optically visible T Tauri stars.

Consecutive arc-like outflow structure, evident in RNO 1B/1C and Elias 1-12, suggests the FUor phenomenon is repetitive on timescales of $\sim 5 \times 10^3$ and 1.3×10^4 years respectively. The kinematics of the molecular gas disk surrounding V1057 Cygni also support this hypothesis and yield a timescale of $\geq$600 years. These estimates are comparable to the value of 10^3- $\sim 10^4$ years based on the number of observed FUors. The extended molecular gas envelopes surrounding the FUors V1515 Cygni, V1057 Cygni, RNO 1B/1C, and Elias 1-12 are sufficiently massive ($M_{disk} \gtrsim 0.1\ M_\odot$) to supply gas for several FUor outbursts. By comparison, the envelope surrounding FU Orionis lacks enough mass for another outburst, suggesting it is near the end of the FUor stage.

High resolution maps of millimeter continuum emission are probably the most reliable way of identifying and estimating the mass of embedded thermal sources (*cf* Sargent & Welch 1994). Aperture synthesis maps of V1331 Cygni, V1057 Cygni, and RNO 1B/1C suggest FUors are single stars. Higher spatial resolution speckle imaging, at infrared wavelengths, indicate that only Z Canis Majoris has a companion. This suggests that outburst initiation models which invoke binary companions are incompatible with observations.

6. Summary

Solar type stars form by the contraction of dust and gas in cold molecular clouds. Material falls onto an extended molecular gas envelope before being accreted through a circumstellar disk onto the star. Accretion through the circumstellar disk drives a powerful wind which evacuates gas from around the stellar poles. Accretion from the surrounding cloud begins to decline and the star becomes visible. This is the advent of the FU Orionis phase as observationally defined.

The young star is surrounded by a massive centrifugally supported accretion disk which is in turn embedded in a large molecular gas envelope (see Sections 8.1 and 8.2). Material infalls from the ambient cloud but at lower rates than during the deeply embedded phase. The mass of the disk is insufficient to maintain the previous high levels of accretion onto the star; disks alternate between a high and low accretion mode. During periods of low accretion rates ($\sim 10^{-6}$ $M_\odot$ yr^{-1}), the disk accumulates mass until a thermal instability initiates another outburst. Material then falls onto the star at $\sim 10^{-4}$ $M_\odot$ yr^{-1} until the disk is depleted (about 100 years). Accretion rates then revert to their lower values and mass begins to accumulate again. Another outburst occurs $\sim 10^4$ years later.

Since the mass loss rate is proportional to the accretion rate, outbursts are recorded in the structure of outflowing swept-up gas. Each outburst evacuates molecular gas from around the star and forms a filled outflow shell (see Section 8.3). Consecutive outbursts form "shells within shells" or cross-cutting arcs in the larger outflow structure. As the source evolves, the outflow clears out more gas leaving less to be swept-up by subsequent outbursts while the envelope mass diminishes since less material is available for accretion. Eventually, after approximately 10-100 outbursts, infall rates decrease to levels where mass no longer accumulates in the disk. Outbursts cease, and accretion onto the star proceeds at T Tauri levels.

The FUor outflow affects the star's circumstellar environment chemically as well as physically (see Section 8.4). Shocks in outflowing gas destroy dust grains, returning Si onto the gas phase, and causing enrichments in SiO. Low velocity grain-grain collisions evaporate grain mantles causing methanol enhancements in the gas phase. Phase changes, also initiated by collisions, cause methanol to be expelled from the mantle leaving smaller molecules like HCN and H_2CO still depleted onto the grains.

References

Andersson, C., Johansson, L. E. B., Winnberg, A., & Goss, W. M. 1979, A&A, 80, 260

Anglada, G., Rodríguez, L. F., & Girart, J. M. 1994, ApJ, 420, L91

Anglada, G., Rodríguez, L. F., Torrelles, J. M., Estalella, R., Ho, P. T. P., Canto, J., Lopez, R. & Verdes-Montenegro, L. 1989, ApJ, 341, 208

Avery, L. W., Hayashi, S. S., & White G. L. 1990, ApJ, 357, 524

Bachiller, R., & Gomez-Gonzalez, J. 1992, A&A Rev., 3:257

Bachiller, R., Tafalla, M., & Cernicharo, J. 1994, ApJ, 425, L93

Bastian, U., & Mundt, R. 1985, A&A, 144, 57

Bastien, P. 1982, A&AS, 48, 153; 48, 513

Bechis, K. P., & Lo, K. Y., 1975, ApJ, 201, 118

Beckwith, S., Natta, A., & Salpeter, E. E. 1983, ApJ, 267, 596

Beckwith, S. V. W., & Sargent, A. I. 1991, ApJ, 381, 250

Beckwith, S., Sargent, A. I., Chini, R. S., & Gusten, R. 1990, AJ, 99, 924

Bell, K. R., & Lin, D. N. C. 1994, ApJ, 427, 987

Blake, D. F., Allamandola, L., Sandford, S., Hudgins, D., & Freund, F. 1991, Science, 254, 548

Blake, G. A., Sandell, G., van Dishoeck, E. F., Groesbeck, T. D., Mundy, L. G., & Aspin, C. 1994, submitted ApJ

Bonnell, I., & Bastien, P. 1992, ApJ, 401, L31

Cabrit, S., & Bertout, C. 1992, A&A, 261, 274

Calvet, N., Hartmann, L., & Kenyon, S. J. 1991, ApJ, 383, 752

Carr, J. S., Harvey, P. M., & Lester, D. F. 1987, ApJ, 321, 71

Chackerian, C., & Tipping, R. H. 1983, J. Molec. Spectrosc., 99, 431

Charnley, S. B. 1994, ApJ, submitted

Chavarria-K., C. 1981, A&A, 101, 105

Chernin, L., Masson, C., & Pino, E. M. G. D. 1994, ApJ, 426, 204

Clarke, C. J., Lin, D. N. C., & Papaloizou, J. 1989, MNRAS, 236, 495

Clarke, C. J., Lin, D. N. C., & Pringle, J. E. 1990, MNRAS, 242, 439

Cohen, M., & Kuhi, L. V. 1979, ApJS, 41, 743

Croswell, K., Hartmann, L., & Avrett, E. H. 1987, ApJ, 312, 227

Draine, B. T 1989, Proceedings of the 22^{nd} ESLAB Symposium on Infrared Spectroscopy in Astronomy, edited by B. H. Kaldeich (ESA Publications, Noordwijk)

Edwards, S., Ray, T., & Mundt, R. 1993, in Protostars and Planets III, edited by E. H. Levy and J. I. Lunine (University of Arizona, Tuscon)

Edwards, S., & Snell, R. L. 1982, ApJ, 261, 151

Eislöffel, J., Hessman, F., Mundt, R. 1990, A&A, 232, 70

Elias, J. H. 1978, ApJ, 223, 859

Ellison, B. E., & Miller, R. L. 1987, Int. J. Infrared and Millimeter Waves, 8, 608

Ellison, B. E., Schaffer, P. L., Schaal, W., Vail, D., & Miller, R. E. 1989, Int. J. Infrared and Millimeter Waves, 10, 937

Estalella, R., Mauersberger, R., Torrelles, J. M., Anglada, G., Gomez, J. G., Lopez, R., & Muders, D. 1993, ApJ, 419, 698

Evans, N. J. II, Balkum, S., Levreault, R. M., Hartmann, L., & Kenyon, S. 1994,

ApJ, 424, 793

Evans, N. J. II, Levreault, R. M., & Harvey, P. M., ApJ, 301, 894

Fiebig, D., Duschl, W. J., & Tscharnuter, W. M. 1992, IAU Circ, 5438, 1

Galli, D., & Shu, F. H. 1993, ApJ, 417, 243

Goldsmith, P. F., & Arquilla, R. 1985, in Protostars and Planets II, edited by D. C. Black and M. S. Mattthews (University of Arizona, Tucson)

Goodrich, R. W. 1987, PASP, 99, 116

Guilloteau, S., Bachiller, R., Fuente, A. & Lucas, R. 1992, A&A, 265, L49

Hartmann, L. 1992, in NATO ASI on The Formation and Evolution of Stars, edited by N. Kylafis and C. Lada

Hartmann, L., & Kenyon, S. J. 1985, ApJ, 299, 462

Hartmann, L., & Kenyon, S. J. 1987a, ApJ, 312, 243

Hartmann, L., & Kenyon, S. J. 1987b, ApJ, 322, 393

Hartmann, L., Kenyon, S. J., & Hartigan, P. 1993, in Protostars and Planets III, edited by E. H. Levy and J. I. Lunine (University of Arizona, Tuscon)

Herbig, G. H. 1958, ApJ, 128, 259

Herbig, G. H. 1977, ApJ, 217, 693

Herbig, G. H. 1989, in ESO Workshop on Low-Mass Star Formation and Pre-Main Sequence Objects, edited by B. Reipurth (Garching ESO), 233

Herbig, G. H., & Robbin Bell, K. 1988, Lick Observatory Bulletin No. 1111

Hildebrand, R. H. 1983, QJRAS, 24, 267

Irvine, W. M., Goldsmith, P. F., & Hjalmarson, Å1987, in Interstellar Processes, edited by D. Hollenbach and H. A. Thronson (D. Reidel, Dordrecht)

Jansen, D. J., van Dishoeck, E. F., & Black, J. H. 1994, A&A, 282, 605

Kenyon, S. J., & Hartmann, L. 1991, ApJ, 383, 664

Kenyon, S. J., Hartmann, L., Gomez, M., Carr, J. S., & Tokunaga, A. 1993, AJ, 105, 1505

Kenyon, S. J., Hartmann, L. W., & Hewett, R. 1988. ApJ, 325, 231

Kenyon, S. J., Hartmann, L. W., & Kolotilov, E. A. 1991, PASP, 103, 1069

Koerner, D. W. 1994, Ph.D. Thesis, California Institute of Technology

Ladd, E. F., Adams, F. C., Casey, S., Davidson, J. A., Fuller, G. A., Harper, D. A., Myers, P. C., & Padman, R. 1991, ApJ, 382, 555

Lada, C. J., 1991, in The Physics of Star Formation and Early Stellar Evolution, edited by C. J. Lada and N. D. Kylafis (Kluwer Academic Publ., Dordrecht)

Langer, W. D., & Penzias, A. A. 1993, ApJ, 408, 539

Levreault, R. M. 1983, ApJ, 265, 855

Levreault, R. M. 1985, Ph.D. Thesis, University of Texas at Austin

Levreault, R. M. 1988, ApJ, 330, 897

Lin, D. N. C., & Papaloizou 1985, in Protostars and Planets II, edited by D. C. Black and M. S. Mattthews (University of Arizona, Tucson)

Lissauer, J. J., & Stewart, G. R. 1993, in Protostars and Planets III, edited by E. H. Levy and J. I. Lunine (University of Arizona, Tuscon)

Lo, K. Y., & Bechis, K. P. 1973, ApJ, 185, L71

Lo, K. Y., & Bechis, K. P. 1974, ApJ, 190, L125

Mangum,J., & Wootten, A. 1993, ApJS, 89, 123

Masson, C. R., & Chernin, L. M. 1993, ApJ, 414, 230

McCutcheon, W. H., Dewdney, P. E., Purton, C. R., & Sato, T. 1991, AJ, 101, 1435

McMuldroch, S., Blake, G. A., & Sargent, A. I. 1995, to appear in AJ

McMuldroch, S., Sargent, A. I., & Blake, G. A. 1993, AJ, 106, 2477

McMullin, J. P, Mundy, L. G., Wilking, B. A., Hezel, T., & Blake, G. A. 1994, in preparation

Ménard, F., Bastien, P. 1992, AJ, 103, 564

Meyers-Rice, B. A., & Lada, C. J. 1991, ApJ, 368, 445

Moriarty-Schieven, G. H., & Snell, R. L. 1988, ApJ, 332, 364

Moriarty-Schieven, G. H., Snell, R. L., Strom, S. E., Schloerb, F. P., Strom, K. M., & Grasdalen, G. L. 1987, ApJ, 319, 742

Mundt, R., Stocke, J., Strom, S., Strom, K., & Anderson, E. 1985, ApJ, 297, L45

Myers, P. C. 1985, in Protostars and Planets II, edited by D. C. Black and M. S. Mattthews (University of Arizona, Tucson)

Ohashi, N., Kawabe, R., Hayashi, M., & Ishiguro, M. 1991, AJ, 102, 2054

Ohtsuki, K., Ida, S., Nakagawa, Y., & Nakazawa, K. 1993, in Protostars and Planets III, edited by E. H. Levy and J. I. Lunine (University of Arizona, Tuscon)

Petrov, P. P., & Herbig, G. H. 1992, ApJ, 392, 209

Pringle, J. E. 1981, Ann Rev Astr Ap, 19, 137

Racine, R. 1968, AJ, 73, 233

Raga, A. C., & Biro, S. 1993, MNRAS, 264, 758

Raga, A., & Cabrit, S. 1993, A&A, 278, 267

Reipurth, B. 1992, A&A, 257, 693

Rieke, G., Lee, T., & Coyne, G. 1972, PASP, 84, 37

Rodríguez, L. F., & Hartmann, L. W. 1992 Rev Mex Astr, 24, 135

Rodríguez, L. F., Hartmann, L. W., & Chavira, E. 1990, PASP, 102, 1413

Rodríguez, L. F., Haschick, A. D., Torrelles, J. M., & Myers, P. C. 1987, A&A, 186, 319

Sandell, G., Knee, L. B. G., Aspin, C., Robson, I. E., & Russell, A. P. G. 1994, A&A, submitted

Sargent, A. I., & Welch, W. J. 1993, Ann Rev Astr Ap, 31, 297

Shakura, N. I., Sunyaev, R. A. 1973, A&A, 24, 337

Shevchenko, V. A., Yakubov, S. D., Ambaryan, V. V., & Garibdzhanyan, A. T. 1991, Sov. Astronomy-A.Zh., 35(2), 135

Scoville, N. Z., Sargent, A. I., Sanders, D. B., Claussen, M. J., Masson, C. R., Lo, K. Y., & Phillips, T. G. 1986, ApJ, 303, 416

Shu, F., Najita, J., Galli, D., Ostriker, E., Lizano, S. 1993, in Protostars and Planets III, edited by E. H. Levy and J. I. Lunine (University of Arizona, Tuscon)

Simon, T., Morrison, N. D., Wolff, S. C., & Morrison, D. 1972, A&A, 20, 99

Snell, R. L. 1987, in Star Forming Regions: Proc. IAU Symp. 115, edited by M. Peimbert and J. Jugaku (D. Reidel, Dordrecht)

Snell, R. L., Dickman, R. L., & Huang, Y.-L. 1990, ApJ, 352, 139

Snell, R. L., Loren, R. B., & Plambeck, R. L. 1980, ApJ, 239, L17

Snell, R. L., & Schloerb, F. B. 1985, ApJ, 295, 490

Spitzer, L. 1978, Physical Processes in the Interstellar Medium (John Wiley & Sons, New York)

Stahler, S. W. 1994, ApJ, 422, 616

Stahler, S. W., Korycansky, D. G., Brothers, M. J., & Touma, J. 1994, ApJ, 431, 341

Staude, H. J., & Neckel, Th. 1991, A&A, 244, L13

Terebey, S., Chandler, C. J., & Andre, P. 1993, ApJ, 414, 759

Torrelles, J. M., Rodríguez, L. F., Cantó, J., Marcaide, J., & Gyulbudaghian, A. L. 1983, Rev. Mex. Astron. Astrofis., 8, 147

Uchida, Y., Kaifu, N., Shibata, K., Hayashi, S. S., Hasegawa, T., & Hamatake, H. 1987, Publ. Astron. Soc. Japan, 39, 907

van Dishoeck, E. F., Blake, G. A., Draine, B. T., & Lunine, J. I. 1993, in Protostars and Planets III, edited by E. H. Levy and J. I. Lunine (University of Arizona, Tuscon)

van Dishoeck, E. F., Jansen, D. J., & Phillips, T. G. 1993, A&A, 279, 541

Wachmann, A. A. 1939, Beob. Zirk., 21:12.

Weidenshilling, S. J., & Cuzzi,J. N. 1993, in Protostars and Planets III, edited by E. H. Levy and J. I. Lunine (University of Arizona, Tuscon)

Weintraub, D. A., & Kastner, J. 1993, ApJ, 411, 767

Weintraub, D. A., Sandell, G., & Duncan, W. D. 1989, ApJ, 340, L69

Weintraub, D. A., Sandell, G., & Duncan, W. D. 1991, ApJ, 382, 270

Welin, G. 1971, Inf Bull Var Stars, 581

Welin, G. 1976, A&A, 49, L145

Welty, A., Strom, S., Edwards, S., Kenyon, S. J., & Hartmann, L. 1992, ApJ, 397, 260

Whitney, B. A., & Hartmann, L. 1993, ApJ, 402, 605

Williams, H. A., & Tohline, J. E. 1988, ApJ, 334, 449

Winnberg, A., Graham, D., Walmsley, C. M., & Booth, R. S. 1981, A&A, 93, 79

Wolstencroft, R. D., & Simon, T. 1975, ApJ, 199, L169

Yang, J., Umemoto, T., Iwata, T., & Fukui, Y. 1991, ApJ, 373, 137

Yang, J. Ohashi, N., & Fukui, Y. 1993, in Second Northeast-Asian Regional Meeting on Recent Development in Millimeter-Wave and Infrared Astronomy, edited by S. H. Cho and H. S. Chung (Korea Astronomy Observatory, Daejon)

Zhou, S., Evans II, N. J., Kömpe, C., & Walmsley, C. M. 1993, ApJ, 404, 232